Practical Implementation of Multiple-input Multiple-output Visible Light Communication Systems

Rui BIAN

A thesis submitted for the degree of Doctor of Philosophy.
The University of Edinburgh.
2019

Abstract

Wireless data transmission occurs everywhere and the global data traffic is growing rapidly. Current radio frequency (RF) spectrum resource is becoming saturated and our current RF based wireless communication system will not meet the demands for data traffic in the future. Research efforts have been put into increasing the spectral efficiency of existing RF networks. Techniques such as multiple-input multiple-output (MIMO), have been well studied. However, it is still insufficient for the rapid growth of the wireless data traffic. The visible light (VL) spectrum is over 1000 times wider than the size of the entire 300 GHz RF spectrum, therefore, it is a viable alternative resource. The spread of light emitting diode (LED) lighting infrastructures provides a good opportunity for visible light communication (VLC). VLC turns the LEDs into high speed wireless data transmitter while retaining their illumination function. VLC has drawn much attention in recent years. MIMO techniques have also been studied in VLC. However, there have only been a few studies that compared practical MIMO VLC systems with theoretical studies. In this thesis, several practical implementations of the MIMO VLC system have been presented.

First, a generalised space shift keying (GSSK) system, which is a simple form of spatial modulation (SM), has been presented. The performance of the field programmable gate array (FPGA) based real-time system has been studied against different transmitter (Tx) and receiver (Rx) numbers. The performance against mobility has also been evaluated. Up to 16 transmitters have been used and the result shows high spectral efficiency is achievable with the low complexity implementation of GSSK.

Second, an investigation of an ultra-high speed wavelength division multiplexing (WDM) VLC system using inexpensive, low-complexity front-end components has been developed. We have used ordinary off-the-shelf red, green, blue and yellow (RGBY) LEDs in surface-mount technology (SMT). The result shows that a data rate of over 15 Gbits/s can be achieved by using proper optimising procedures on the inexpensive commercially available components. This study has confirmed the potential of high achievable capacities of VLC systems.

Third, the first MIMO VLC system using organic photovoltaics (OPVs) has been implemented featuring simultaneous data communication and energy harvesting. Record data rates of 102 Mbits/s for a single pixel and 146 Mbits/s for a 2-by-2 MIMO set-up have been presented. The first system model for MIMO OPV VLC system has been proposed. The model has been validated with experimental results. The scalability of the system has also been discussed.

Lay summary

Wireless data transmission plays a vital role in our daily lives. However, as the number of connected devices grows, the amount of data transmitted by these devices will also grow, which leads to a rapid increase in global data traffic. Thus, it is highly likely that our current radio frequency (RF) based wireless communication systems will not be able to fulfil the data traffic demands in the future. Research efforts have been made to improve the efficiency of conveying data in the existing RF network under these circumstances. Nonetheless, it is still not sufficient for the rapidly growing data traffic. Visible light communication (VLC), which uses the visible light spectrum to send and receive information at very high data transmission speeds, has emerged in this context and has become a viable alternative for wireless communication. VLC can utilise light emitting diodes (LEDs), which are widely used for lighting today, into high speed wireless data transmitters while retaining their illumination function. It has drawn extensive attention in recent years, in which multiple-input multiple-output (MIMO) techniques have also been studied. However, there have only been a few studies that compared practical MIMO VLC systems with theoretical studies. In this thesis, several practical implementations of the MIMO VLC system have been presented.

First, a generalised space shift keying (GSSK) system has been implemented and presented. The key method of the GSSK system is to convey data bits into the spatial location of the active transmitters. The presented real-time system is implemented based on field programmable gate array (FPGA) and for the first time, up to 16 micro-LEDs (μLEDs) are used. This work shows that high efficiency can be achieved with this low complexity implementation of GSSK.

Second, an investigation of an ultra-high speed wavelength division multiplexing (WDM) VLC system using inexpensive, low-complexity front-end components has been developed. The system is composed of red, green, blue and yellow (RGBY) LEDs. We have used ordinary off-the-shelf LEDs in surface-mount technology (SMT) and a data rate of over 15 Gbits/s can be achieved. This study has confirmed the potential of high achievable capacities of VLC systems.

Third, the use of solar cells for simultaneous energy harvesting and data communication is also studied. The first MIMO VLC system using organic solar cells has been analysed. A system model is proposed and it is validated with experimental results. Record data rates of 102.2 Mbits/s for a single pixel and 146 Mbits/s for a 2-by-2 MIMO set-up have been presented. The scalability of the implementation is also discussed.

Declaration of originality

I hereby declare that the research recorded in this thesis and the thesis itself were composed and originated entirely by myself in the School of Engineering at The University of Edinburgh.

Rui Bian
Edinburgh, UK
February 2019

Acknowledgements

Firstly, I would like to offer my sincerest gratitude to my wife, Juan Xiong, my mother, Jiaqing Luo, my father, Shan Bian, my paternal grandparents, Yiqun Xiong, Jingnan Bian, and my maternal grandparents, Qiulian Fang, Caiyuan Luo, for their love and support. They are always by my side, no matter what troubles I meet. Without them, I will never be complete.

I would like to sincerely thank my supervisor Prof. Harald Haas, who has shown me the wonderful world with light. With his encouragement and support, I have learned so much during the past four years.

I would like to thank all my friends and colleagues. They have helped me a lot in both study and life. This period in Edinburgh is a precious memory in my life.

Contents

List of figures

List of tables

Acronyms and abbreviations

AC	alternating current
ADC	analog-to-digital converter
AGC	automatic gain control
AM 1.5G	air mass 1.5 global
APD	avalanche photodiode
AWG	arbitrary waveform generator
AWGN	additive white Gaussian noise
B	blue
BER	bit error rate
BHJ	bulk hetero-junction
CIR	channel impulse response
CMOS	complementary metal-oxide-semiconductor
CP	cyclic prefix
DAC	digital-to-analog converter
DC	direct current
DCO-OFDM	direct-current biased optical orthogonal frequency division multiplexing
DD	direct detection
EB	exabytes
EM	electromagnetic
E-O	electrical-to-optical

FEC	forward error correction
FF	fill factor
FFT	fast Fourier transform
FoV	field of view
FPGA	field programmable gate array
FSO	free-space optical communication
G	green
GaAs	gallium arsenide
GaN	gallium nitride
GPMC	general purpose memory controller
GSSK	generalised space shift keying
HDFEC	hard decision forward error correction coding
i	intrinsic
ICI	inter-channel interference
IEEE	institute of Electrical and Electronics Engineers
IFFT	inverse fast Fourier transform
IM	intensity modulation
IM/DD	intensity modulation and direct detection
IoTs	internet-of-things
IR	infrared
IrDA	infrared data association
ISI	inter-symbol interference
km	kilometre

LASER	light amplification by stimulated emission of radiation
LD	laser diode
LED	light emitting diode
LiFi	light-fidelity
LOS	line-of-sight
LRC	inductor, resistor and capacitor
MIMO	multiple-input multiple-output
ML	maximum likelihood
QAM	quadrature amplitude modulation
MSB	most significant bit
n	n-type
NFA	non-fullerene acceptors
NRZ	non-return-to-zero
OFDM	orthogonal frequency division multiplexing
OLED	organic LED
O-OFDM	optical OFDM
OOK	on-off keying
OPV	organic photovoltaic
OWC	optical wireless communication
p	p-type
PAM	pulse amplitude modulation
PC	personal computer
PCE	power conversion efficiency

PD	photodiode
PIM	pulse interval modulation
PIN	p-type intrinsic n-type
PPM	pulse position modulation
PSD	power spectral density
PV	photovoltaic
PWM	pulse width modulation
R	red
RC	repetition coding
RF	radio frequency
RGBY	red, green, blue and yellow
RMS	root-mean-squared
RZ	return-to-zero
Rx	receiver
RX1	first receiver
RX2	second receiver
SISO	single-input-single-output
SM	spatial modulation
SMP	spatial multiplexing
SMT	surface-mount technology
SNR	signal-to-noise ratio
SPAD	single-photon avalanche diode
SSK	space shift keying

SSL	solid-state lighting
STC	standard test conditions
TI	Texas Instruments
TIA	transimpedance amplifier
Tx	transmitter
TX4	the fourth LED
UHD	ultra-high-definition
μ **LED**	micro-LED
V	voltage
VCA	voltage-controlled amplifier
VL	visible light
VLC	visible light communication
Vpp	peak-to-peak voltage
VR	virtual reality
vs	versus
WDM	wavelength division multiplexing
Wi-Fi	wireless fidelity
Y	yellow

Nomenclature

$*$	convolution operation
π	pi
A	diode quality factor
A_{r}	detection area
B	bandwidth
c	speed of light in vacuum
C	capacitance
C_0	capacitance in OPV data communication branch
$\mathbf{d}$	distance
d	The Euclidean distance of the received signal and the GSSK signature
f	frequency
g_{c}	concentrator gain
g_{f}	filter gain
g_{nm}	the electrical gain between the output of the n_{th} OPV and the photocurrent generated by the m_{th} OPV
$g_{(n=m)}$	local electrical gain
$g_{(n\neq m)}$	electrical gain from other cells
$\mathbf{G}_0$	electrical channel gain matrix
h	Plank's constant
$h(t)$	channel impulse response
$h_{n_{\mathrm{r}}n_{\mathrm{t}}}$	the optical channel gain from transmitter n_{t} to receiver n_{r}

$h_{\mathrm{r,else}}$	the electrical gain of the thermal noise generated by r to the output of other cells
$h_{\mathrm{r,self}}$	the electrical gain of the thermal noise generated by r to the output of local call
$h_{\mathrm{R_c,else}}$	the electrical gain of the thermal noise generated by R_{c} to the output of other cells
$h_{\mathrm{R_c,self}}$	the electrical gain of the thermal noise generated by R_{c} to the output of local call
$h_{\mathrm{R_L,else}}$	the electrical gain of the thermal noise generated by R_{L} to the output of other cells
$h_{\mathrm{R_L,self}}$	the electrical gain of the thermal noise generated by R_{L} to the output of local call
$h_{\mathrm{R_s,else}}$	the electrical gain of the thermal noise generated by R_{s} to the output of other cells
$h_{\mathrm{R_s,self}}$	the electrical gain of the thermal noise generated by R_{s} to the output of local call
$h_{\mathrm{R_{SH},else}}$	the electrical gain of the thermal noise generated by R_{SH} to the output of other cells
$h_{\mathrm{R_{SH},self}}$	the electrical gain of the thermal noise generated by R_{SH} to the output of local call
$\mathbf{H}$	optical channel matrix
$\left\|H(f)\right\|$	normalised magnitude response
$H_{\mathrm{o}}(f)$	gain of the optical channel
$H_{\mathrm{t}}(f)$	frequency response of the transmitter electrical-to-optical (E-O) gains
$H_{\mathrm{AMP}}(f)$	frequency response of the amplifier stages
$H_{\mathrm{OPV}}(f)$	magnitude frequency response of the LRC circuit model for OPV
$i_{\mathrm{PH}}(\omega)$	the AC component of the photocurrent
I	current through the load resistor
I_0	dark reverse saturation current
I_{b}	bias current
I_{D}	current through the diode

$I_{\mathrm{Linear\_max}}$	the maximum current for working in linear region
I_{photo}	photocurrent
I_{PH}	photo current
J_{sc}	short circuit current density
k_B	Boltzmann's constant
L	inductance
L_0	inductance in OPV energy harvesting branch
m	Lambertian emission order
$m(t)$	input signal
M_k	modulation order at the k_{th} subcarrier
n_{s}	the number of solar cells which have been connected in series
$n(t)$	additive white Gaussian noise
N_{act}	number of subcarriers with non-zero modulation order
N_{cell}	the number of connected solar cells in the system
N_{CP}	cyclic prefix size
N_{FFT}	FFT order
N_0^{sh}	the power spectral density of shot noise
$N^{\mathrm{sh}}(f)$	AWGN shot noise
N_0^{th}	the power spectral density of thermal noise
$N_{0,\mathrm{r}}^{\mathrm{th}}$	the power spectral density of thermal noise generated by resistor r
$N_{0,\mathrm{R_c}}^{\mathrm{th}}$	the power spectral density of thermal noise generated by resistor R_{c}
$N_{0,\mathrm{R_L}}^{\mathrm{th}}$	the power spectral density of thermal noise generated by resistor R_{L}
$N_{0,\mathrm{R_s}}^{\mathrm{th}}$	the power spectral density of thermal noise generated by resistor R_{s}

$N^{\mathrm{th}}_{0,\mathrm{R_{SH}}}$	the power spectral density of thermal noise generated by resistor R_{SH}
$N^{th}(f)$	AWGN thermal noise
P_{ct}	the power of the crosstalk
P_{r}	received optical power by photodetector
$P_{\mathrm{r,bg}}$	received optical power from background light
$P_{\mathrm{r,sg}}$	received signal optical power
$P_{\mathrm{r,tx}}$	received optical power from the transmitter
P_{t}	optical output from LED
q	charge of an electron
$\mathrm{Q}(.)$	Q-function
r	internal resistance in solar cell model
R	data rate
R_{c}	resistance in OPV data communication branch
R_{load}	load resistance
R_{s}	series resistance in solar cell model
R_{L}	resistance in OPV energy harvesting branch
R_{OPV}	OPV responsivity
R_{PD}	responsivity of photodiode
R_{SH}	shunt resistance in solar cell model
R_{Ω}	resistance
$\mathbf{s}^{\mathbf{y}}$	signature value for symbol y
$S(\phi)$	radiant intensity
$S_{\mathrm{r}}(f)$	received signal

$S_{\mathrm{t}}(f)$	frequency component of the transmitted signal
$\mathrm{SNR}_{\mathrm{k}}$	SNR at the k_{th} subcarrier
T	absolute temperature
T_{sym}	a symbol clock
$v(\omega)$	the AC component of the voltage across the load resistor
V	voltage across the load resistor
V_{oc}	open circuit voltage
V_{T}	junction thermal voltage
$\mathbf{w}$	AWGN vector
$\mathbf{x}$	transmitted signal vector
$x(t)$	intensity modulated signal
$X(k)$	the k_{th} M-QAM symbol
$\mathbf{y}$	received signal vector
$y(t)$	received signal
γ	SNR
$\delta(.)$	Dirac delta function
η_{eqe}	external quantum efficiency
η_{qe}	quantum efficiency
λ	wavelength
σ^2_{sh}	the power of shot noise
σ^2_{shot}	shot noise variance
σ^2_{th}	the power of thermal noise
$\sigma^2_{\mathrm{th,r}}$	the power of thermal noise generated by r

$\sigma^2_{\mathrm{th,R_c}}$	the power of thermal noise generated by R_{c}
$\sigma^2_{\mathrm{th,R_L}}$	the power of thermal noise generated by R_{L}
$\sigma^2_{\mathrm{th,R_s}}$	the power of thermal noise generated by R_{s}
$\sigma^2_{\mathrm{th,R_{SH}}}$	the power of thermal noise generated by R_{SH}
$\sigma^2_{\mathrm{thermal}}$	thermal noise variance
τ	duty cycle
τ_{c}	response time constant
ϕ	incident angle
$\phi_{1/2}$	half-power semi-angle
ϕ	radiant angle
ψ_{FoV}	field of view

Chapter 1
Introduction

1.1 Motivation

Wireless data transmission occurs everywhere in our daily life. By 2022, the number of devices connected to the network is estimated to be more than three times the global population [1]. In addition, the bandwidth-consuming technologies, such as ultra-high-definition (UHD) videos and virtual reality (VR), are growing rapidly. Both the exploding number of devices and the increasing amount of data require tremendous data traffic resource. It is estimated that by 2022 the annual global data traffic will reach 396 exabytes (EB, 1 EB = 10^{18} bytes) per month [1]. Current radio frequency (RF) spectrum resource is becoming saturated and our present RF based wireless communication systems will not meet the demands for data traffic in the future. Some innovative technologies have been studied and considered to increase the spectral efficiency of existing RF networks such as multiple-input multiple-output (MIMO) techniques. However it is still insufficient for the rapid growth of the wireless data traffic.

As shown in Figure 1.1, compared to the size of the entire RF spectrum, the total frequency bandwidth of optical spectrum including the infrared (IR) and visible light (VL) is over 1000 times wider [2]. Such plenty of resources could be used for wireless data transmission. Lots of effort have been made to develop the optical wireless communication (OWC) technology. Ac-

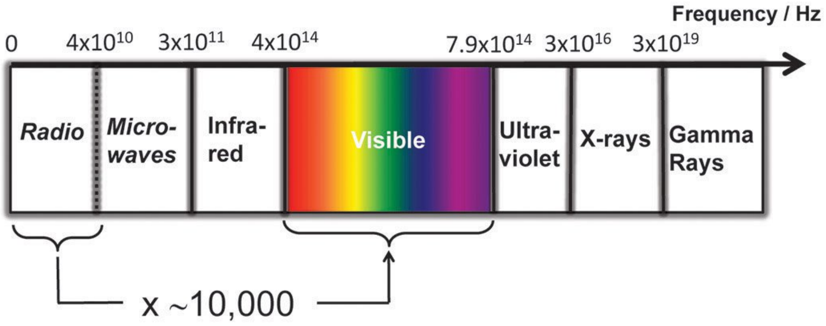

Figure 1.1: *The electromagnetic spectrum.*

cording to [3], OWC system takes several advantages over RF techniques which are: the optical signal does not interfere with any existing RF system; it can be applied to any radio radiation restricted area; and the optical spectrum resource is unlicensed. With recent developments in solid-state lighting (SSL), light emitting diodes (LEDs) have shown significant advancement in energy efficiency and luminaire lifespan against conventional incandescent and fluorescent bulbs. The spread of LED lighting [4] provides a good opportunity for OWC, or more specifically, for visible light communication (VLC).

VLC has drawn much attention recently with a rapid development. Some modulation techniques that are well-studied in RF systems have been applied to VLC including both single carrier modulation techniques, such as pulse amplitude modulation (PAM), pulse position modulation (PPM) and multi-carrier modulation techniques such as orthogonal frequency division multiplexing (OFDM) [3]. As intensity modulation (IM) and direct detection (DD) are applied in VLC, some of these modulation techniques need to be modified before being applied in order to make sure the modulated transmitted signal is both real-valued and non-negative. MIMO techniques are also being studied in VLC for higher spectral efficiency. Spatial modulation, which was introduced in [5], is an innovative modulation scheme which combines MIMO and digital modulation techniques and has also been applied to VLC [6]. Compared to the published theoretical research activities, there are fewer studies reporting practical implementations, especially with MIMO techniques. One possible reason is that lots of practical issues seem to occur when considering hardware. For example, the performance of a VLC link may be limited by the characteristics of the front-end elements. It is, however, significant to compare any theoretical results with experimental results to validate the modelling work or any method being applied.

One factor which makes VLC a promising technology is that LED lighting is replacing conventional lighting sources and will become the dominant lighting infrastructure [4]. VLC can be directly applied to LEDs, which means in the future any lighting source can become a high-speed wireless data transmitter. However, the term 'high-speed' may not suit all LEDs as in general the commercial LEDs have very limited bandwidth [7, 8] due to the large diode capacitance [9]. Some high-speed links have been reported using specially designed micro-LEDs (μLEDs) [10, 11]. Even though, a study on the low-cost commercial LEDs is still required to exploit the potential of delivering high-speed wireless data by using delicate modulation techniques.

Portable or wearable devices being enabled with internet-of-things (IoTs) is a trend nowadays. More than 50 billion objects are expected to be connected by 2020 with the IoT technology [12]. Organic material is printable, lightweight and flexible, which makes it a good candidate for such devices. Moreover, photovoltaic devices have been used for energy harvesting and recently they have been demonstrated as photodetector for VLC links [13]. A study has been carried out to use organic photovoltaics (OPVs) for simultaneous VLC detection and energy harvesting [14]. A MIMO set-up of such OPVs can further improve both communication efficiency and total harvested energy.

1.2 Contribution

The thesis focuses on the practical implementations of MIMO VLC systems by the use of different front-end elements and digital communication techniques. While most current published work are primarily on simulation work, this thesis presents mainly the experimental work. It aims at addressing the following three research objectives:

- Understand the practical limitations and challenges of spatial modulation applied to a practical VLC system.
- Development of techniques to achieve ultra-high speed data transmission from low-cost commercial front-end components..
- Build and optimise a MIMO VLC system using organic photovoltaic devices for simultaneous data communication and energy harvesting.

Several contributions have been made by addressing these objectives.

Following the first objective, a field programmable gate array (FPGA) based VLC transmitter is implemented. This driver is capable of generating both space shift keying (SSK) and generalised SSK (GSSK) modulated signals and drive up to 16 individual optical sources simultaneously. Several studies are conducted with different types of optical detectors being applied. Firstly, a 4-by-4 real-time GSSK system is investigated. A FPGA based decoder is implemented for the first time and 4 commercial PIN PDs are used. In the second study, up to 16 LEDs are driven by the proposed driver and APDs are used at the receiver end. The BER performance of the set-up is evaluated with different position arrangements and at different spectral efficiencies. This part of the work has led to the publication at IEEE BlackSeaCom 2017 [15]. In a follow-up study, a complementary metal-oxide-semiconductor (CMOS) APD chip introduced in [16] is used as a receiver and then led to a high speed integrated VLC link which was published in [17].

Considering the second objective, a wavelength division multiplexing (WDM) based MIMO VLC system is implemented using low-cost off-the-shelf red, green, blue and yellow (RGBY) LEDs and a record data rate of 15.73 Gb/s is achieved. This is the highest data rate using off-the-shelf components in the currently published work. The system is carefully designed based on the chosen LEDs' characteristics and an implementation of DCO-OFDM with adaptive bit and power loading is used to exploit the potential of achievable data rates. A receiver circuit with low-cost commercial components is also designed showing that an ultra high speed VLC system using off-the-shelf components is indeed possible. This work has led to a conference paper [18] and a journal paper [19].

Regarding the third objective, a MIMO system using organic photovoltaics (OPVs) as photodetectors for simultaneous data communication and energy harvesting is studied theoretically and implemented experimentally for the first time. The system model is proposed. Record data rates have been achieved and the system model has been validated with experimental results.

1.3 Thesis Layout

The remainder of this thesis is organised as follows. In Chapter 2, the concept of a VLC system is briefly introduced. The fundamental elements for implementing a practical VLC system are introduced. The characteristics of these components are described and a typical model of a VLC link is provided. The different optical modulation techniques are introduced including both single-carrier modulation and multi-carrier modulation techniques. Finally, multiple-input multiple-output (MIMO) concepts and techniques are briefly provided.

In Chapter 3, a FPGA based GSSK driver is introduced and described in details. The first real-time practical implementation of GSSK VLC system is presented. The basic concepts of GSSK are introduced and the implementation details are described. The BER performance of the system is evaluated as well as the performance against mobility. A further implementation using APDs and up to 16 LEDs is also demonstrated showing the presented system is capable of running high order GSSK modulation with low system complexity. In addition, a CMOS

APD chip [17] together with an imaging lens is applied to the system and the experimental results are given. Finally, the limitations of current implementation is discussed with possible future work directions.

In Chapter 4, the investigation of ultra-high speed VLC system using inexpensive off-the-shelf front-end components has been presented. A WDM system with four low-cost commercially available LEDs (RGBY) has been implemented. A full WDM operation with all four colour links being active simultaneously has been demonstrated. The optimisation process for driving the LED source has been introduced and analysed with experimental results. The arrangement of dichroic mirrors has also been discussed with numerical results. A record data rate of 15.73 Gb/s has been reported while the limitations of the system being addressed. Another investigation on the achievable data rate changes with low-complexity receiver has been introduced. A custom-designed receiver circuit has been introduced with inexpensive commercial components and a low-complexity circuit design. By investigating the inexpensive low-complexity front-end components, this work confirms that high capacity of VLC systems can be achieved with such components when suitable optimisation techniques are applied.

In Chapter 5, the first MIMO VLC implementation using organic solar cells is presented for simultaneous wireless data communication and energy harvesting. Record data rate has been presented and the first system model for MIMO OPV VLC system has been proposed. The model has been validated with experimental results. The scalability of the system has been discussed based on the system model.

Chapter 6 summaries the key results of this thesis. The limitations of the experimental work in this thesis are given and future research directions are also discussed.

Chapter 2
Background

2.1 Introduction

Optical communication refers to any information transmission at a distance using light as a carrier. In a typical optical communication system, the transmitter encodes information into an optical signal and the receiver reproduces the information from the received signal. The earliest form of optical communication can be traced back to the days when electronic devices were not employed. Visual techniques, such as smoke signals and beacon fires, were used for signalling purposes. The signal can either be simple, like the presence of smoke, or complex, such as lights flashed in Morse code. The photophone, invented by Alexander Graham Bell in 1880, can be considered as the first piece of equipment that used optical signals for wireless communication [20]. It succeeded in transmitting a voice signal clearly over a distance of 200 metres by using sunlight as the light source. Since then, the method of optical communication has been exploited and significantly improved.

Today, optical wireless communication (OWC) uses light emitting diodes (LEDs) or Laser diodes (LDs) as transmitters. Thus the development of OWC is significantly related to the development of such optoelectronic devices. In 1962, the first practical Gallium Arsenide (GaAs) LED was announced [21] and in the same year MIT Lincoln Labs presented an experimental OWC link using the GaAs LED to transmit a television signal over 30 miles (48 km) [22]. After the announcement of the first working LD in July 1960 [23], a number of free-space optical communication (FSO) links for point-to-point long distance transmissions were demonstrated in the 1960s and 1970s. A list of such demonstrations can be found in [24]. OWC has continued to be a subject of research, especially by the military.

The use of OWC for short range wireless communication was first implemented using infrared (IR) sources. In [25], Gfeller and Bapst presented a diffused IR radiation communication system for achieving a data rate of 100 kbps. The infrared data association (IrDA), founded in

1993, became a highly successful wireless short-range data transmission solution and formulated a set of protocols [26, 27]. However, over the decades, IR technology is gradually being replaced by radio wave (RF) technologies such as Bluetooth and wireless fidelity (Wi-Fi) [27]. Recent advancements in solid-state lighting (SSL) through LEDs have shown significant improvements in energy efficiency and luminaire lifespan compared to current incandescent and fluorescent bulbs. The LED lighting industry has had tremendous growth and it is expected that nearly 80% of all lighting infrastructures will be LEDs by 2020 [4]. The increasing usage of LEDs provides a great opportunity for OWC. LEDs can be switched to different light intensity levels at a rate fast enough to be unnoticed by the human eye, and therefore can be used for wireless data transmission. This is known as visible light communication (VLC). In recent years, VLC has shown great potential in high speed wireless communication and links with Gbps data rate have been experimentally demonstrated [10, 11]. The institute of Electrical and Electronics Engineers (IEEE) has published IEEE802.15.7 standard for short-range VLC and now announces the revision r1 [28]. There is also an IEEE802.11bb task group on wireless light communication [29].

2.2 Front-end Elements

Intensity modulation (IM) is used in VLC. Optical sources, such as LEDs and LDs, are the key front-end elements at the transmitter side which convert electrical signals to light signals. Optical detectors are the key elements at the receiver side which detect the light signal and generate electrical signal. The principle of direct detection (DD) is applied in VLC. Optics and optical filters can be used to shape the radiation pattern of the light or truncate the spectrum of light reaching the detector for better connection quality. Currently, the characteristics of these front-end elements are a major limitation of the performance of a VLC system. In the following sections, the characteristics of these key front-end elements are introduced.

2.2.1 Light Emitting Diode

LEDs are widely considered for VLC techniques and in related studies [7]. A typical LED is a semiconductor device with a p-n junction. The p refers to the p type semiconductor which contains an excess of holes, while the n refers to the n type semiconductor with an excess of electrons. When a forward bias voltage is applied to the p-n junction, current flows and the recombination of electrons and holes release energy in the form of photons [30]. This effect is called electroluminescence. The colour of the emitting light corresponds to the energy of the photons, which is determined by the energy required for electrons to cross the band gap of the semiconductor [30]. By using different semiconductor materials, current commercial LEDs are available across the ultraviolet, visible and infrared spectrum.

2.2.1.1 Lambertian Radiation Pattern

In general, the LEDs' light emission is modelled with a generalised Lambertian radiant intensity. The radiant intensity can be calculated [22]:

$$S(\phi) = P_{\mathrm{t}} \frac{(m+1)}{2\pi} \cos^{m}(\phi), \tag{2.1}$$

where P_{t} is the optical output of the LED, ϕ is the radiant angle and m is the Lambertian emission order corresponding to the half-power semi-angle $\phi_{1/2}$ by $m = -\frac{\ln 2}{\ln(\cos\phi_{1/2})}$. The half-power semi-angle $\phi_{1/2}$ is defined as the semi-angle where the optical power falls to 50%.

2.2.1.2 LED Non-linearity

In the process of IM with an LED source, there is a non-linear relationship between the input electrical signal and the output optical signal [31]. Figure 2.1 shows a measured relationship between the input driving current and the output optical power of a commercial red LED (VLMS1500). When the input current is below $I_{\mathrm{Linear\_max}}$, the LED can linearly convert the current to optical power. In general, the LED is the main non-linearity source in a VLC system and pre-distortion techniques can be applied to compensate LED non-linearities [31].

2.2.1.3 LED Modulation Bandwidth

The frequency response of an LED typically shows a low-pass characteristic. The normalised magnitude response can be estimated by [22]:

$$\left|H(f)\right| = \frac{1}{\sqrt{1+(2\pi f \tau_{\mathrm{c}})^2}}, \tag{2.2}$$

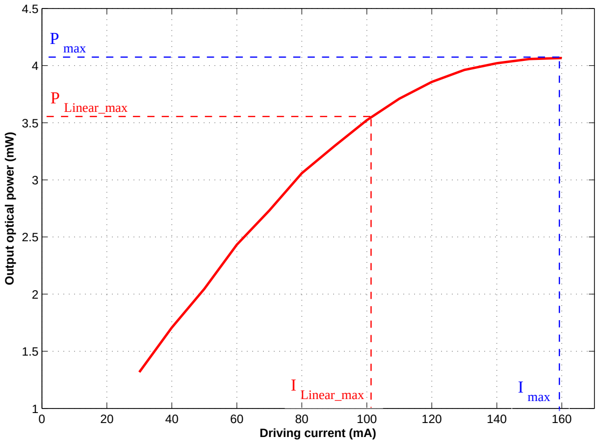

Figure 2.1: *An example of the measured relationship between driving current and output optical power of a commercial red LED (VLMS1500).*

where f is the frequency, τ_{c} is the response time constant which is related to the spontaneous lifetime of the carrier in the device active region and the large diode capacitance [9]. In LEDs that being used for high optical power output applications, the current-injected p-n junction area is large and such diodes have very large capacitance. In this case, denoting the overall series resistance as R_{Ω} and the diode capacitance as C, τ_{c} is given by the RC time constant. In LEDs that being used for data communication purposes, the current-injected active region is much smaller, so the modulation bandwidth is limited by the spontaneous lifetime of the carrier rather than the diode capacitance [9].

2.2.1.4 Type of LEDs

There are a wide range of commercial available LEDs in the market featuring different colours, sizes or optical power output. Currently there are two primary ways to make white LEDs. The first is to mix three individual LEDs that emit the three primary colours - red (R), green (G) and blue (B) - to form white light. The second way is to use phosphor material on a blue LED to produce broad-spectrum white light. These LEDs are normally designed for illuminations or relative applications, thus they are capable of delivering high optical output power. However, if they are considered as VLC transmitters, their modulation bandwidth would be the major limitation. Most commercial available white LEDs are made with blue LEDs and their modulation bandwidth is significantly limited (typically 2-3 MHz [7]) due to the slow response of the phosphor material. LEDs that emit monochromatic lights have a higher modulation bandwidth

(20 MHz [8]) than white LEDs, however this is still limited.

In [10], a blue Gallium Nitride (GaN) Micro-LED (μLED) was introduced. This μLED is specially designed for data communication. It is much smaller in size compared to commercial LEDs, therefore it offers a much higher modulation bandwidth of 60 MHz, while still offering lower output optical power as a trade-off. A data rate of 3 Gb/s is reported using this μLED and later 7.91 Gb/s data transmission rate is reported using a single GaN violet μLED [11].

Organic LEDs (OLEDs) are widely used in displays and smart devices, which benefit from their flexibility and low cost [32, 33]. The principle of using OLEDs as VLC transmitters to enable internet-of-things (IoTs) on smart devices has drawn attention recently. However, the modulation bandwidth of OLEDs is generally much lower than inorganic LEDs. The low charge mobility of the organic semiconductor material is one of the main reasons for low bandwidth. In addition, the large size and thickness would introduce high capacitance which reduces the modulation bandwidth significantly [33]. A data rate of 51.6 Mbps is reported in [34] using a monochromic OLED.

2.2.2 Photodetectors

Photodetectors are light sensors that convert optical signals to electrical signals. As the light strength is generally weak [22] after travelling through a communication channel, a photodetector with high light sensitivity in the given wavelength region is required to produce sufficient signal power with a low noise level for good quality data communication. In addition, in VLC, the direct detection method is used as a detection technique so high bandwidth is also required for the photodetectors to detect the rapid changes in the light intensity. To fulfil the requirements for VLC, a set of characteristics of photodetectors need to be considered.

2.2.2.1 Photodetector Characteristics

The key characteristics of a photodetector include the detection pattern, responsivity and the modulation bandwidth [3]. A Lambertian detection pattern is generally used for a single photodetector [25]. The field of view (FoV) of a photodetector is defined as the angle between the points where the directivity is reduced to 50% of the detection pattern. The FoV can be enhanced or limited by the use of other optical components to achieve a desired performance in a VLC system [3]. Thus, the parameters of the additional optical elements need to be added to model the actual detection characteristics.

Photodetector responsivity R_{PD} (in A/W) is defined as the amount of photocurrent generated per unit incident optical power and is given by [35]:

$$R_{\mathrm{PD}} = \frac{\lambda q \eta_{\mathrm{qe}}}{hc}, \tag{2.3}$$

where λ is the wavelength of light, $q = 1.602 \times 10^{-19} C$ is the charge of an electron, $h = 6.626 \times 10^{-34}$J· s is the Planck's constant, c refers to the speed of light in vacuum and η_{qe} is the quantum efficiency of the photodetector which is defined as [35]:

$$\eta_{\mathrm{qe}} = \frac{\text{number of electrons produced}}{\text{number of photons absorbed}}. \tag{2.4}$$

Thus the photocurrent being generated can be calculated as:

$$I_{\mathrm{photo}} = R_{\mathrm{PD}}(\lambda) P_{\mathrm{r}}, \tag{2.5}$$

where P_{r} refers to the optical power collected by the photodetector. The material of the photodetector would affect the responsivity for a given wavelength.

The magnitude of the current signal generated by a photodetector is always proportional to the optical power of light reaching the detecting area [22]. This transfer is linear over a large dynamic range [3] and by employing the automatic gain control (AGC) method, the signal clipping due to the saturation of the photodetector can be avoided. In addition, the light signal is unlikely to become non-linearly distorted because of the signal attenuation due to path loss. Therefore it is normally assumed that the non-linear distortion happens only at the transmitters [3].

A larger detection area will offer higher output power. However, similar to an LEDs characteristics, a photodetector also has a low-pass electrical frequency response and its bandwidth depends on both device capacitance and the transit time of the carriers excited by photons through the depletion region [22]. The larger size of the detection area would form higher capacitance which reduces the bandwidth. A photodetector with a smaller detecting area would provide a higher bandwidth to accommodate high data rate communication. However, a higher optical output power at the transmitters or a careful optics arrangement may be required for the photodetector to generate sufficient signal amplitude. This trade-off between the optical-to-electrical gain and the modulation bandwidth needs to be considered while designing a photodetector and implementing a VLC system. As mentioned in [3], this trade-off can be alleviated by using an array of photodetectors which increase the overall detection area without reducing the individual modulation bandwidth. In addition, these photodetectors can be freely located to form a desired detection pattern.

2.2.2.2 Type of Photodiodes

Four types of photodetectors are mentioned in [22]: PIN photodiodes (PDs), avalanche photodiodes (APDs), photoconductors and metal-semiconductor-metal photodiodes. Single-photon avalanche diodes (SPADs) are also being investigated for VLC studies. Among all these types of photodetectors, both PIN diodes and APDs are the most promising types of photodetector in VLC studies and OWC systems [22]. A solar panel, or photovoltaic (PV) panel, which is used for energy harvesting from sunlight, has recently been demonstrated as a dual-functional receiver for simultaneous energy harvesting and wireless data communication [13]. Studies using solar panels as OWC receivers have been published [36, 37] and more recently, a VLC link using organic photovoltaic devices, has been reported [14].

Compared to a p-n junction diode, the PIN photodiode consists of a wide, undoped or very slightly n-doped intrinsic region i between the p type and the n type semiconductor material [38]. During an operation, the PIN diode is reverse biased with a sufficient voltage so that the i region is fully depleted with carriers. When the incident photon arrives with enough energy, which is equal to or greater than the band-gap energy of the semiconductor material, the photo will give up its energy and excite an electron. This process generates free electron-hole pairs mainly in the depletion region. Under the high electrical field generated by the reverse bias voltage, the flow of the free electrons and holes forms the photocurrent [38]. According to [22], the responsivity of a PIN PD is always less than unity, so in practical, a transimpedance amplifier (TIA) circuit is always required to convert photocurrent signal into voltage signal. However, PIN PDs are capable of achieving a very high bandwidth. The Silicon PIN PD can work in the visible light spectrum region and the achieved responsivity is in the range of 0.4 to 0.6 A/W [38]. The bandwidth of commercially available PIN PDs can achieve up to 40 GHz (e.g. Thorlab RX40AF) while a much higher bandwidth has also been reported for research purposes [22].

Unlike PIN PDs, the APD can achieve much higher responsivity. This is because in the APD,

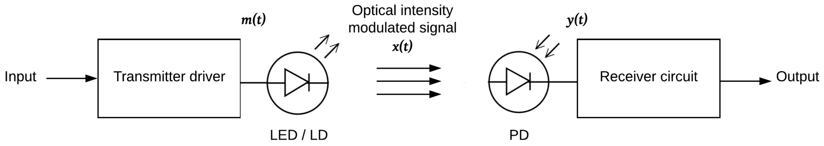

Figure 2.2: *Typical block diagram for an optical wireless system.*

an internal first-stage current gain is provided through avalanche multiplication [22] before the photocurrent reaches any TIA circuit. The responsivity of a Silicon APD can reach 77-130 A/W which includes a gain in the range of 150-250 [38]. However, in the APD there is always a multiplication noise due to the avalanche process. In addition, the APD requires a much higher bias voltage than a PIN PD to operate and it is more temperature sensitive which makes the condition more restricted when using an APD in a practical system.

Photovoltaic (PV) devices, such as solar cells, have drawn some attention from researchers for being multi-function receivers. Different from PDs, a PV device does not require any external power supply to convert optical signals to electrical signals. However, for simultaneous energy harvesting, the PV devices always have a large detection area which leads to a low modulation bandwidth. Organic photovoltaic (OPV) devices, such as organic solar cells, are now widely used in portable devices. They are also being studied as potential VLC receivers to enable IoTs.

2.3 Channel Modelling

In this section, the major elements of an optical wireless channel are introduced. As this work focuses on evaluating different point-to-point optical wireless system implementations, only directed line-of-sight (LOS) configuration is considered. A typical OWC system block diagram is shown in Figure 2.2. The driving current of the optical source is modulated by the signal $m(t)$ and consequently an optical intensity modulated signal $x(t)$ is emitted. The optical signal travels through the free-space LOS channel and reaches the photodetector where a photocurrent $y(t)$ is generated. This IM/DD based optical wireless system can be modelled as shown in Figure 2.3. R_{PD} is the photodetector responsivity, $h(t)$ is the channel impulse response (CIR) and $n(t)$ refers to the signal-independent noise which is modelled as the additive white Gaussian noise (AWGN). This model can be summarised as [39]:

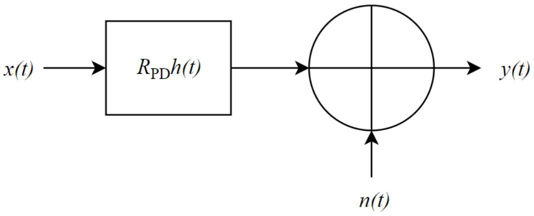

Figure 2.3: *Equivalent model of an optical wireless system.*

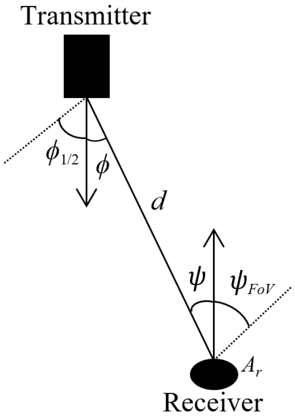

Figure 2.4: *LOS DC gain geometry.*

$$y(t) = R_{\mathrm{PD}} x(t) * h(t) + n(t), \tag{2.6}$$

where $*$ denotes the convolution operation.

The geometry shown in Figure 2.4 includes a Lambertian optical source with Lambertian emission order m, R_{PD}, an FoV of ψ_{FoV} and a detection area of A_{r}. The distance between the transmitter and the receiver is d with an irradiance angle of ϕ and an incident angle of ψ. Assuming an optical filter with a transmission gain of g_{f} and a concentrator with gain g_{c} are used, the DC gain can be approximated as follows [39]:

$$H(0) = \begin{cases} \frac{A_{\mathrm{r}}(m+1)}{2\pi d^2} \cos^m(\phi) g_{\mathrm{f}} g_{\mathrm{c}} \cos\psi, & 0 \leq \psi \leq \psi_{\mathrm{FoV}}. \\ 0, & \text{elsewhere.} \end{cases} \tag{2.7}$$

Then for a given transmitted optical power P_{t} the received optical power P_{r} becomes

$$P_{\mathrm{r}} = H(0)P_{\mathrm{t}}. \tag{2.8}$$

The CIR can be expressed as follows [22]:

$$h(t) = \frac{A_{\mathrm{r}}(m+1)}{2\pi d^2}\cos^m(\phi)g_{\mathrm{f}}g_{\mathrm{c}}\cos\psi\delta(t-\frac{d}{c}), \tag{2.9}$$

where $\delta(.)$ represents the Dirac delta function. It is assumed that $\psi \leq \psi_{\mathrm{FoV}}$.

2.4 Photodetection Noise

The noise level is always one of the decisive factors while evaluating the performance of a point-to-point VLC link. In this section, shot noise and thermal noise are introduced.

Shot noise is a major noise source in a VLC link which is related to the particle nature of light [22]. When the number of photons received by the detector is large enough, the shot noise can be modelled as an AWGN and its power can be expressed as [3]:

$$\sigma^2_{\mathrm{shot}} = 2q(P_{\mathrm{r,tx}} + P_{\mathrm{r,bg}})R_{\mathrm{PD}}B, \tag{2.10}$$

where $P_{\mathrm{r,tx}}$ refers to the received optical power from the transmitters, $P_{\mathrm{r,bg}}$ denotes the received power from the background light, and B is the noise bandwidth which is determined by the modulation bandwidth of the signal or the receiver bandwidth that has been used.

Another noise source is thermal noise, due to the resistive element in the receiver circuit [22]. Thermal noise can also be modelled as AWGN with a variance of [3]:

$$\sigma^2_{\mathrm{thermal}} = \frac{4k_BT}{R_{\mathrm{load}}}B, \tag{2.11}$$

where $k_B = 1.38^{-23}J/K$ denotes the Boltzmann's constant, T refers to the absolute temperature and R_{load} is the load resistance in the receiver circuit. For a given set-up, the power of the total noise can be approximated as [3]:

$$\sigma_{AWGN}^2 = N_0 B = 2q(P_{\mathrm{r,tx}} + P_{\mathrm{r,bg}}) R_{\mathrm{PD}} B + \frac{4k_B T}{R_{\mathrm{load}}} B, \tag{2.12}$$

N_0 denotes the power spectral density (PSD) of the total receiver noise.

2.5 Modulation Techniques

The data transmission in OWC is realised through intensity modulation and direct detection (IM/DD). Unlike RF systems where the frequency, amplitude and phase of the carrier can be modulated, it is the intensity of the optical carrier that is modulated in OWC. The information is encoded in the envelope of the transmitted signals which need to be both in real value and non-negative. Modulation techniques including both single-carrier modulation and multi-carrier modulation are well studied for OWC and are achieved in practice [3].

2.5.1 Single Carrier Modulation

In single-carrier pulse modulation, the information can be encoded in: (1) the duration of the pulse such as pulse width modulation (PWM) and pulse interval modulation (PIM) [22, 40]; (2) the position of the pulse in a fixed time frame such as pulse position modulation (PPM) [39]; (3) the amplitude of the pulse such as pulse amplitude modulation (PAM) [41]. A typical block diagram of single-carrier pulse modulation is shown in Figure 2.5. The modulated signal passes through a digital-to-analog converter (DAC) and is converted to a train of analogue pulses. A pulse shaping filter is applied to obtain a band-limited signal. A matched filter is applied to the received signal which is then converted to digital signal by an analog-to-digital converter (ADC) and decoded [3].

On-off keying (OOK) is possibly the best-known modulation technique for IM/DD in optical communication systems. The concept is simple: whenever a pulse occurs during a symbol period, a bit one is transmitted while the bit zero is represented as the absence of the pulse in the symbol period. The multi-level M-PPM achieves higher power efficiency than OOK by sending a pulse with a shorter duration within the symbol period. However, the bandwidth requirement is increased as well as the system complexity [22]. In multi-level M-PPM, a time-domain symbol contains $\log_2(M)$ input bits and the spectral efficiency is $\log_2(M)/M$

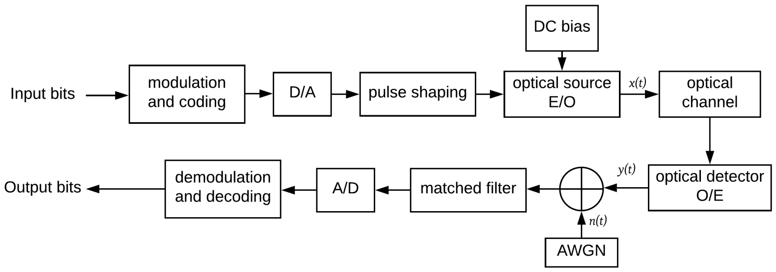

Figure 2.5: *Typical block diagram for a single-carrier pulse modulation based optical wireless system.*

bits/s/Hz [39]. In multi-level M-PAM, each time-domain symbol also contains $\log_2(M)$ and the achieved spectral efficiency is $\log_2(M)$ bits/s/Hz [39].

One issue which limits the throughput of such techniques is the inter-symbol interference (ISI). As mentioned in previous sections, the channel of an OWC link containing all the front-end elements has a low-pass characteristic. At high frequencies, the pulse bandwidth exceeds the channel coherence bandwidth and as a result, the root-mean-squared (RMS) delay spread of the optical wireless channel exceeds the pulse duration and ISI occurs. This also happens when the lowest delay is larger than the symbol duration. A guard interval can be added which reduces the overlap of the pulses, however, the system spectral efficiency is decreased [42].

2.5.2 Multi-carrier Modulation

In multi-carrier modulation, instead of conveying information through pulses, the information is encoded in complex-valued subcarriers at different frequencies. Multi-level quadrature amplitude modulation (M-QAM) is applied as the underlying modulation scheme. The subcarriers are multiplexed after the inverse fast Fourier transform (IFFT) operation at the transmitter and demultiplexed by the fast Fourier transform (FFT) operation at the receiver. Orthogonal frequency division multiplexing (OFDM) has been well studied in RF communication and also been applied to optical communication [43–45]. M-QAM optical OFDM (O-OFDM) gains robustness to ISI because the symbol duration is significantly longer than the RMS delay spread of the wireless channel [3]. In addition, O-OFDM is capable of delivering very high data rates [46, 47]. For the concept of IM/DD, the time-domain O-OFDM signal also need to be real-valued and non-negative. The real-valued signal can be obtained by imposing Hermitian symmetry on the subcarriers [44]. One way to obtain a non-negative time-domain signal is known as direct-current-biased optical OFDM (DCO-OFDM) which introduces a DC bias to the OFDM signal [43].

A block diagram for the key elements in a DCO-OFDM communication system is shown in Figure 2.6 [3]. The input bit stream is coded and mapped to M-QAM symbols. The time-domain OFDM symbols are generated after having the IFFT operation for the M-QAM symbols. $X(k)$ is the k^{th} M-QAM symbol for a DCO-OFDM frame containing N_{FFT} subcarriers and $k = 1, 2, \cdots, \frac{N_{\text{FFT}}}{2} - 1$. As Hermitian symmetry is imposed to generate real-valued signal, there are $N_{\text{FFT}}/2 - 1$ subcarriers carrying information with index $k = 1, \cdots N_{\text{FFT}}/2 - 1$. In addition, $X(0) = X(\frac{N_{\text{FFT}}}{2}) = 0$ because of the DC bias and $X(N_{\text{FFT}} - k) = X^{*}(k)$ where $[\cdot]^{*}$ denotes the complex conjugate operation. For having a non-negative signal, a positive DC bias is added. A cyclic prefix (CP) extension with a length of N_{CP} is added at the beginning of the OFDM symbols to mitigate the ISI and the inter-carrier interference [44].

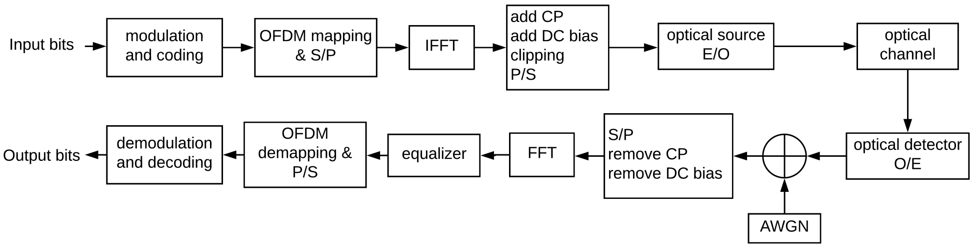

Figure 2.6: *Typical block diagram for a DCO-OFDM based optical wireless system.*

Bit and power loading system has been implemented in this work. The modulation order can be selected adaptively at each subcarrier to maximise the achievable data rate at a target bit error rate (BER) [48]. The modulation order at each subcarrier M_k is determined by the available SNR and target BER. The BER of a M-QAM modulation format with SNR_k can be approximated as [49]

$$\begin{aligned}\text{BER}\left(M_k, \text{SNR}_k\right) \simeq & \frac{4\left(1 - \frac{1}{\sqrt{M_k}}\right)}{\log_2 M_k} \\ & \times \sum_{l=1}^{\min(2,\sqrt{M_k})} \text{Q}\left((2l-1)\sqrt{\frac{3\text{SNR}_k}{2\left(M_k - 1\right)}}\right)\end{aligned} \tag{2.13}$$

where Q(.) is the Gaussian Q-function. Therefore, using the iterative algorithm for bit loading, the modulation orders M_k are determined, and the overall data rate s is given by [50]

$$s = \frac{\sum_{k=1}^{\frac{N_{\mathrm{FFT}}}{2}} \log_2 M_k}{(N_{\mathrm{FFT}} + N_{\mathrm{CP}})/2B}, \tag{2.14}$$

where N_{CP} is the cyclic prefix size.

2.6 MIMO Techniques

Multiple-input multiple-output (MIMO) techniques are well studied and widely implemented in radio frequency (RF) communication systems providing high data rates with high spectral efficiency [51, 52]. Currently the growing number of LED based lighting infrastructures offer potential opportunities for MIMO applications. In general, multiple transmitters are used for indoor lighting and an array of multiple LEDs may be equipped for one single light installation. In addition, off-the-shelf LEDs provide limited bandwidth, which restricts the achievable data rate of practical OWC systems. Therefore, achieving higher spectral efficiency is desired in OWC systems, with limited bandwidth. By using multiple transmitters and multiple receivers, MIMO OWC systems benefit from the multiplexing and diversity gain and are capable of offering higher spectral efficiency.

Repetition coding (RC) is the simplest MIMO technique. The same signal is sent by all transmitters at the same time. For RC which employs M-PAM, a spectral efficiency of $\log_2(M)$ bits/s/Hz is achieved. According to [3], RC can be represented by a single-input single-output (SISO) scheme with the same received electrical energy.

Another technique is spatial multiplexing (SMP). In SMP, independent data streams are sent to each transmitter at the same time. For SMP which contains N_t transmitters and employs M-PAM, the achieved spectral efficiency is increased to $N_t \log_2(M)$ bits/s/Hz compared to RC.

Wavelength division multiplexing (WDM) is a technique which multiplexes multiple optical carrier with different wavelengths at the transmitter end and demultiplexes at the receiver end. WDM can be realised in different structures. For instance, only bandpass filters at the receiver side may be used for detecting each wavelength individually [53], or a combination of bandpass filters at the receiver and dichroic mirrors at the transmitter may be selected [54]. Similar to SMP, independent data streams are carried by each individual wavelength. WDM is widely used in optical fibres and can also be applied in OWC systems.

Spatial modulation (SM), which was firstly proposed in [5] and enhanced in [55, 56], is a new technique combining MIMO and digital modulation techniques and has also been applied to OWC [6]. SM introduces extra information bits in spatial dimension in addition to the conventional signal constellation. Thus the achieved throughput is enhanced. For a SM with N_t transmitters, each individual transmitter can be represented by a unique index of $\log_2(N_t)$ binary bits. During transmission, a transmitter is only activated when its index matches the on-coming random spatial symbols. When M-PAM is employed, SM achieves a spectral efficiency of $\log_2(N_t) + \log_2(M)$ bits/s/Hz. During each symbol period, there is only one transmitter being activated, thus, inter-channel interference (ICI) is avoided. In addition, compared to other MIMO techniques, SM has a lower decoding complexity [5].

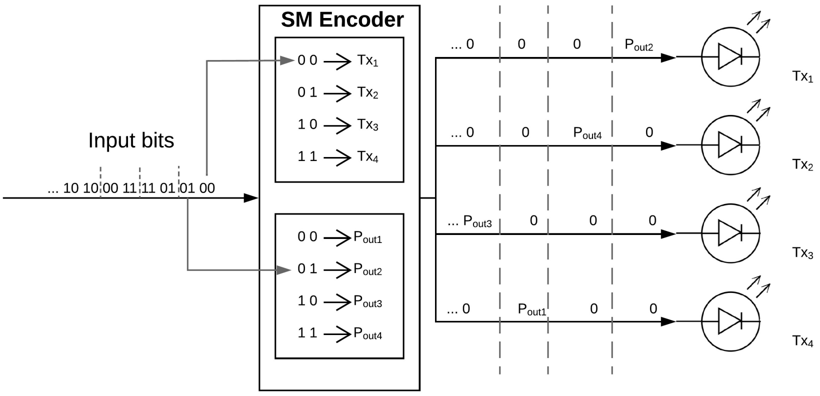

Figure 2.7: *Illustration of SM 4-PAM operation with 4 transmitters.*

Figure 2.7 illustrates the operation of SM M-PAM with $N_t = 4$ and $M = 4$. $Tx_1 - Tx_4$ represent the four transmitters and $P_{\text{out}1} - P_{\text{out}4}$ refer to the four levels of the emitting signal. In the example, $\log_2(N_t) = 2$ bits are used for selecting the transmitter while $\log_2(M) = 2$ bits are encoded to each 4-PAM symbol. As illustrated in the diagram, in the first coming 4 bits sequence '0 1 0 0', the emitting signal $P_{\text{out}2}$ represented by the bits '0 1' is sent to Tx_1 which is decided by the bits '0 0'. During this symbol period, the other three transmitters remain inactivated.

MIMO techniques can also be divided into non-imaging MIMO and imaging MIMO. In an optical non-imaging system, each receiver has an individual non-imaging concentrator. The light from each LED is received by all the receivers with different strengths. A comprehensive study on the non-imaging MIMO schemes is presented in [57]. However, the number of reported practical implementation of non-imaging MIMO system is limited. An implementation of a non-imaging MIMO VLC system is reported in [58] with a data rate of 50 Mbits/s. In an optical imaging-MIMO system, an imaging receiver is used. Each LED is imaged by the imaging lens onto the detector array. A study comparing both non-imaging MIMO and imaging-MIMO is presented in [59] and several implementations of imaging-MIMO have been reported in [16, 60].

2.7 Summary

In this chapter, the basic concept of a VLC system is introduced. The characteristics of the front-end elements which define a VLC system have been described. In addition, the channel model for a LOS set-up is described and the noise source are briefly introduced. Optical modulation techniques, including both single carrier modulation and multi-carrier modulation, are discussed. Lastly, several MIMO techniques are presented.

Chapter 3
Practical Implementation of Generalised Space Shift Keying

3.1 Introduction

A VLC system employs intensity modulation (IM) and direct detection (DD) for data modulation. Incoherent solid-state lighting elements such as light emitting diodes (LEDs) are used as VLC transmitters. A micro-LED (μLED) with a size of 50 μm diameter was introduced in [61] and an optical link at a data rate of up to 3 Gb/s with a single high bandwidth μLED was demonstrated in [10]. These μLEDs are used in this work to evaluate the performance of the presented system and understand the practical limitations other than the low bandwidth of transmitters.

Multiple-input multiple-output (MIMO) techniques have been studied within free space VLC [57] as they offer high data rates by increasing spectral efficiencies. Spatial modulation (SM) introduces additional information bits in the spatial domain thus enhancing the achieved throughput. During each symbol period, there is only one transmitter being activated, thus the inter-channel interference (ICI) is avoided. Space Shift Keying (SSK) [62] and generalised SSK (GSSK) [63] are special cases of SM where only spatial information is transmitted and each transmitter is either activated or off. SSK and GSSK inherit the robustness against LED non-linearities from OOK [64] while offering higher spectral efficiency by exploiting the spatial dimension. Compared to modulation techniques such as pulse amplitude modulation (PAM) and direct current biased Optical Orthogonal Frequency Division Multiplexing (DCO-OFDM), SSK and GSSK have much lower complexity in their implementation. Digital-to-analog converters (DACs) are not required, which significantly reduces the complexity and the cost. In addition, SSK and GSSK also work in dimmed conditions which supports the IEEE 802.15.7 standard [65] by changing the duty cycle of transmitters. Both SSK and GSSK are well studied for optical communication [66, 67], but there are few practical implementations. Work in [68] and [69] present both SSK and GSSK set-ups using a camera as a receiver. Higher modulation order operations can be achieved by using more LEDs. A high resolution camera receiver can make the LED sources well separated on the image because there are a large number of pixels which can detect the LED lights. However, the data rate is limited by the camera's frame rate - reported as up to 1000 frames per second. The work in [70] shows an offline experimental set-up with 2 LEDs and 1 photo diode (PD) receiver. It is stated that the experimental modulation order is limited by the arbitrary waveform generator (AWG) which contains only two output ports.

A practical real-time GSSK driver has been implemented using FPGA. It is capable of driving up to 16 individual optical sources simultaneously. Several experimental set-ups have been demonstrated with the system BER performance being evaluated. Firstly, a real-time GSSK system with μLEDs is presented. A real-time GSSK decoder has been implemented using a FPGA. The real-time operations with up to 4 μLEDs are presented with measured data and simulation results. The system performance is assessed for one or more receivers. In addition, the results indicate that the system contains flexibility against receiver movements to a certain extent and a precise alignment is not required. Hardware and software implementations are introduced. Limitations of this initial proof-of-concept implementation are also identified and solutions are proposed. The second GSSK set-up contains 16 μLEDs and 4 APDs showing the GSSK operation with a spectral efficiency of up to 16 bits per symbol. At last, a further GSSK implementation using a complementary metal-oxide-semiconductor (CMOS) APD receiver chip is presented.

3.2 Generalised Space Shift Keying

GSSK is a special implementation of SM and a generalised case of SSK. It is based on the fact that the system contains a transmitter array while only spatial information is transmitted. The transmitters are switched on and off without conveying information in frequency domain. The block diagram of SSK operation with four transmitters can be simplified from Figure 2.7 and is illustrated in Figure 3.1. The activated transmitter refers to the incoming bits and it is 2 bits in a 4-SSK operation. Considering a SSK system with N_t transmitters and N_r receivers, each transmitter represents a unique binary index and this index is termed as a spatial symbol. Data is encoded by activating one of these N_t LEDs during each symbol period. The achieved spectral efficiency is $\log_2(N_t)$ bits/symbol.

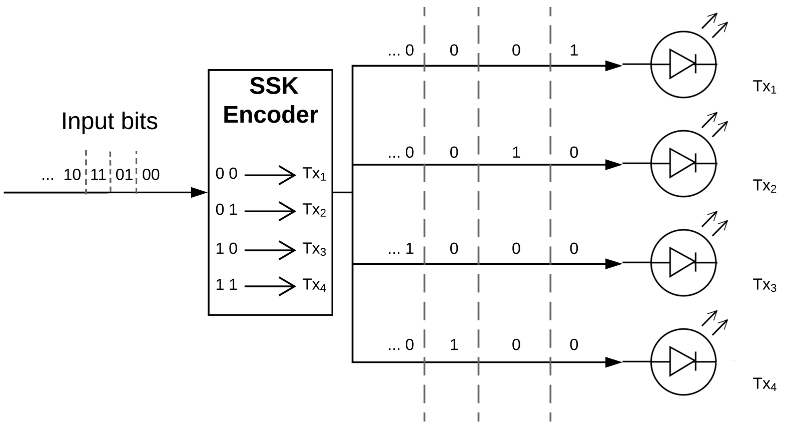

Figure 3.1: *Illustration of SSK operation with 4 transmitters*

Table 3.1: *Example of GSSK scheme for 2 transmitters and* $\tau = 1$

Symbol	Binary	Tx_1	Tx_2
0	[0 0]	OFF	OFF
1	[0 1]	OFF	ON
2	[1 0]	ON	OFF
3	[1 1]	ON	ON

This operation can be generalised using GSSK by removing the limitation of turning on only one LED during each symbol duration. For an LED array of N_t LEDs, there are 2^{N_t} combinations of modulating LEDs including turning off all the LEDs. Thus in the N_t GSSK system, the maximum spectral efficiency is N_t bits per symbol. During a symbol clock T_{sym}, a duty cycle τ can be introduced to control how long the LED will be on during each symbol duration. A non-return-to-zero (NRZ) pulse pattern is formed when $\tau = 1$ and each LED is on for the whole symbol duration. Using an NRZ pulse pattern offers the maximum spectral efficiency of N_t bits per symbol. When $\tau < 1$, each LED is turned on for part of each symbol duration and then turned off, then the signal is in the return-to-zero (RZ) pulse pattern. In practice, the received signal usually experiences a variation in the nominal zero level and this is known as the baseline drift. It happens due to the average value of the signal during each symbol period changes with time. The RZ pattern has better performance against the signal's baseline drift and it is helpful for synchronisation purposes [71]. Varying the duty cycle will also make the LEDs work in dimmed conditions, which supports the IEEE 802.15.7 standard [72]. An example GSSK scheme for two LEDs when $\tau = 1$ is shown in Table 3.1.

A maximum likelihood decoder is implemented covering the decoding process. By capturing the training estimation signals, the decoder generates a $N_r \times 1$ vector for each spatial symbol during the particular symbol period which means that a $N_r \times 2^{N_t}$ matrix is established for all the 2^{N_t} symbols. The decoder compares the received signal $\mathbf{x}$ with each signature value $\mathbf{s}^y$ for the symbol y. Both $\mathbf{x}$ and $\mathbf{s^y}$ are in the form of $N_r \times 1$ vector and each element of the vector represents the height of the signal pulse for each receiver during the particular symbol period. The Euclidean distance of the received signal and the signature is calculated as:

$$\mathbf{d} = \sqrt{\sum_{i=1}^{N_r} (\mathbf{x}_i - \mathbf{s}_i^y)^2} \tag{3.1}$$

The spatial symbol, which has the minimum distance with the received signal, is chosen to be the correct and its binary index is the output of the decoder.

In the following sections, several GSSK implementations are presented. Measurements have been carried out to evaluate the bit error ratio (BER) performance with different $N_\mathrm{t} \times N_\mathrm{r}$ set-up and different spectral efficiencies. The BER performance against receiver movement is also considered.

3.3 4-by-4 Real-time GSSK system

3.3.1 System Set-up

A 4-by-4 real-time GSSK has been implemented. The block diagram of the system is shown in Figure 3.2(a) and the presented system is illustrated in Figure 3.2(b).

At the transmitter, a BeagleBone board, which is a low-power open-source hardware single-board computer produced by Texas Instruments (TI), is connected to a FPGA board ValentFX MARK-1 which features the Xilinx Spartan-6 FPGA. The GSSK encoder is implemented using the FPGA, which is capable of generating 16 individual outputs simultaneously. An LED driver board is connected to the FPGA via 16 cables and the 16 ports on the driver board can be separately and digitally controlled by the FPGA. The driver board is attached to a daughterboard which can hold a maximum of 16 μLEDs. Each μLED is connected with a transistor on the driver board which enables the on-off operation controlled by the FPGA. On top of each μLED, a plastic aspheric lens is added which collimates the light and reduces the semi-angle of μLED to 4 degrees.

At the receiver end, there are several separate analog receiver boards which can be used depending on the experimental requirements. Each board consists of a high-sensitivity LEC-RP0508 pin PD, a trans-impedance amplifier (TIA), a Sallen-Key low pass filter, a voltage-controlled amplifier (VCA) and a set gain non-inverting amplifier. Each PD contains 65 pixels which individually gets a responsivity of 0.39 A/W with the active area being around 66.3 mm^2 with a half power angle of 10○. No automatic gain control is implemented in this system. The received analog signal then goes through the TI TLC5540 analog-to-digital converter (ADC). Another BeagleBone and MARK-1 combination is used as the end of the receiver circuitry.

The ADCs operate with a sampling clock of up to 40 MHz and are capable of outputting 8-bits digital signals. Only 5 bits from the most significant bit (MSB) are employed due to the number limits of FPGA input pins.

For the applied firmware and software, a real-time Linux driver is implemented in the Bea-

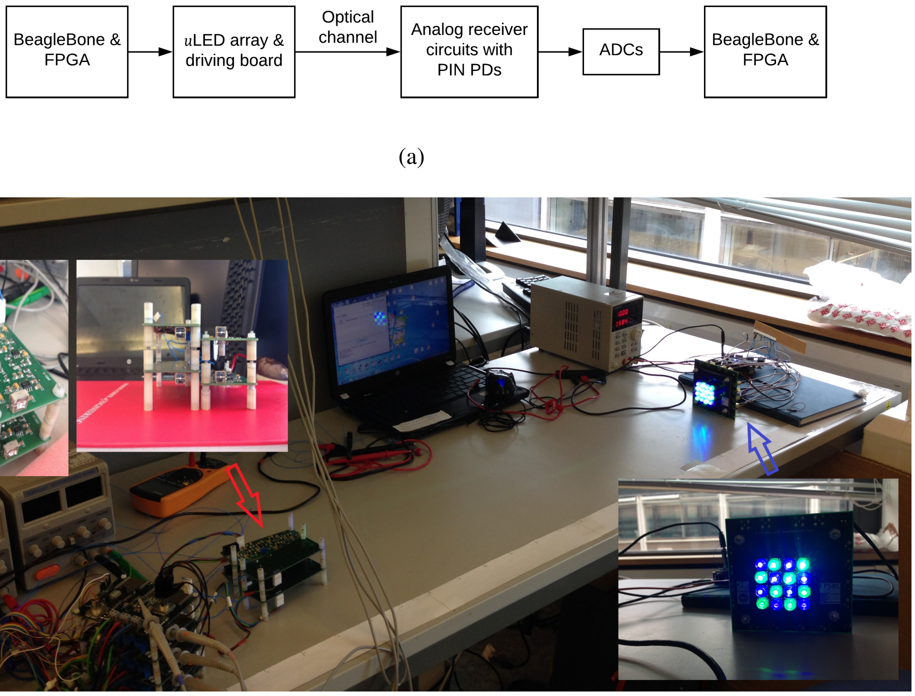

(a)

(b)

Figure 3.2: *The implemented 4-by-4 real-time GSSK system: (a) System block diagram; (b) System set-up with three insets, from left to right, showing: the receiver board, the PD arrangement and the μLED array.*

gleBone Linux system to govern the communication between the BeagleBone and FPGA. The data exchange is realised by using the general purpose memory controller (GPMC) interface. A random bit stream is generated by the BeagleBone, inspected by the user terminal, encoded by the FPGA and sent to different μLEDs. The training estimation signal is added at the beginning of every frame, activating all the GSSK symbols in turn for 4 cycles. One cycle of the training estimation signal for 4-GSSK operation is illustrated in Figure 3.3. The signal is captured by scope and it shows the 16 4-bit GSSK symbols.

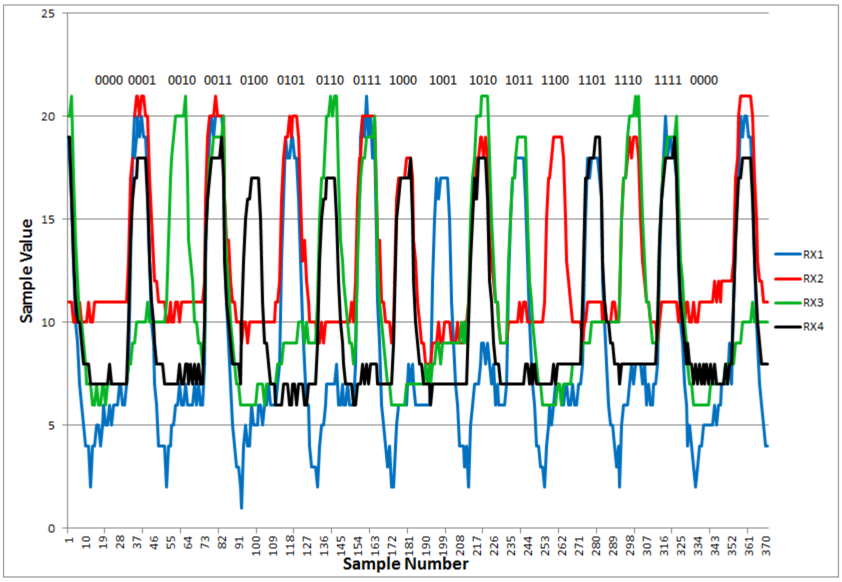

Figure 3.3: *One cycle of the captured training estimation signal for 4-GSSK operation showing the 16 4-bit GSSK symbols.*

On the receiver side, the FPGA receives the digital outputs from the ADCs. With the estimation symbol values acquired from Figure 3.3, the digital signal is decoded by a maximum likelihood decoder implemented inside the FPGA. Results can be accessed by the BeagleBone for saving or displaying on the user terminal. The whole procedure runs in real-time.

3.3.2 Performance Results and Discussion

Experiments are taken for the purpose of evaluating the system's BER performance while varying specific settings: spectral efficiency, receiver number and the position of the receiver. The experiments use up to 4 blue μLEDs and 2 PDs with the coordinates given in Table 3.2 and illustrated in Figure 3.4. All the transmitters are tilted to point directly to RX1. The link distance is 55 cm.

Table 3.2: *Coordinates of the chosen transmitter and receiver locations*

Transmitter position	Receiver position
TX1 (55,22,5) TX2 (55,22,2) TX3 (55,25,2) TX4 (55,24,5)	RX1 (0,22,5) RX2 (0,21,4)

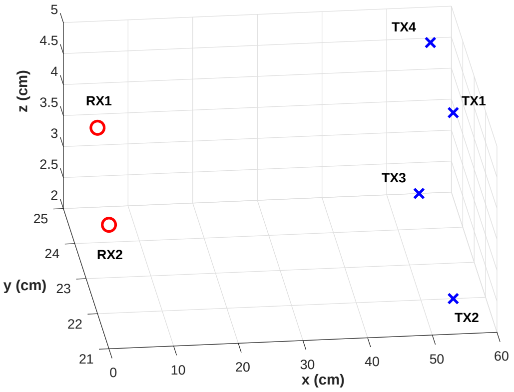

Figure 3.4: *Illustration of the transmitter and receiver arrangement. Transmitter position: TX1, TX2, TX3, TX4; Receiver position: RX1, RX2*

In the first experiment, one single receiver (RX1) is used for operation with a transmitter number of 2, 3 and 4 giving different spectral efficiencies from 2 bits/symbol up to 4 bits/symbol. Figure 3.5 shows the BER performance against the received electrical signal-to-noise ratio (SNR) by comparing to simulation results with measured channel gains. The received electrical SNR is estimated with the received electrical power and the noise deviation. The best achieved BER in the 2-LED case (TX1, TX2) is 1.6×10^{-5} and 2.4×10^{-4} for 3-LED case (TX1, TX2, TX3). The BER increases dramatically when the fourth LED (TX4) is added. This is because there are natural differences in channel gains between each LED and the receiver. These differences are then exploited at the receiver to estimate which symbol has been sent. Comparing the 2-LED and 3-LED cases, the results show that about 6 dB higher SNR is required for the same BER of 10^{-3} when one more LED is added.

To evaluate how the additional receiver will affect the BER performance, the second experiment is conducted based on the previous set-up. The second receiver (RX2) is placed at the given position in Table 3.2. The same GSSK signals with spectral efficiencies of both 3 bits/symbol and 4 bits/symbol are sent and this time there are two receivers working simultaneously to

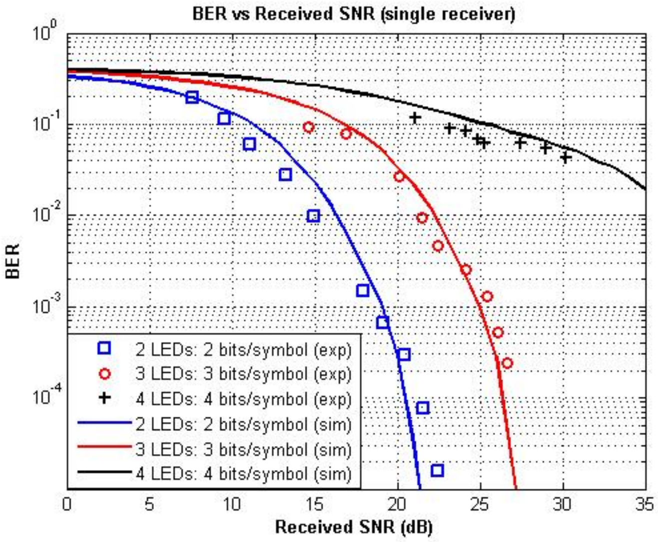

Figure 3.5: *BER vs Received SNR for both experiment and simulation results. Up to 4 LEDs and a single receiver are used.*

distinguish the activated LED combination. Figure 3.6 shows the results using both a single receiver and two receivers at given spectral efficiencies. Results show that the BER performance is significantly improved when an extra receiver is employed. For the 3 bits/symbol case, there is an improvement of around 5 dB for the required received SNR to achieve a BER of 10^{-3}. A BER of 2.7×10^{-3} is achieved with the received SNR of 24.7 dB in the 4 bits/symbol case.

The third measurement is taken to evaluate how the BER performance behaves against receiver mobility. The set-up uses two μLEDs (TX1, TX2) and one receiver (RX1). RX1 is set to different positions. Figure 3.7 shows the BER results against different y-coordinates and z-coordinates (height) while the x-coordinate is kept unchanged (x = 0). The unit of the coordinate is in cm. The red blocks within the figure indicate the measured BER is over 3.8×10^{-3} while the other colours represent better BER results. The coordinates of the two μLEDs are (55, 22, 5), (55, 22, 2) and they are adjusted pointing to the original position of RX1 which is (0, 22, 5) as described above. As a result, the region with a low BER result appears in the upper-right of the plot (2D View) where the received SNR should be relatively higher. It is shown that there is about a 16 cm^2 area with an achieved BER of better than 3.8×10^{-3}. This indicates that the system contains flexibility against receiver mobility to a certain extent rather than requiring a precise alignment. However, the performances within such a region do vary according to the position of the receiver. This is because the two channels conditions keep changing when the receiver changes position, and the system performance depends on the similarity or difference

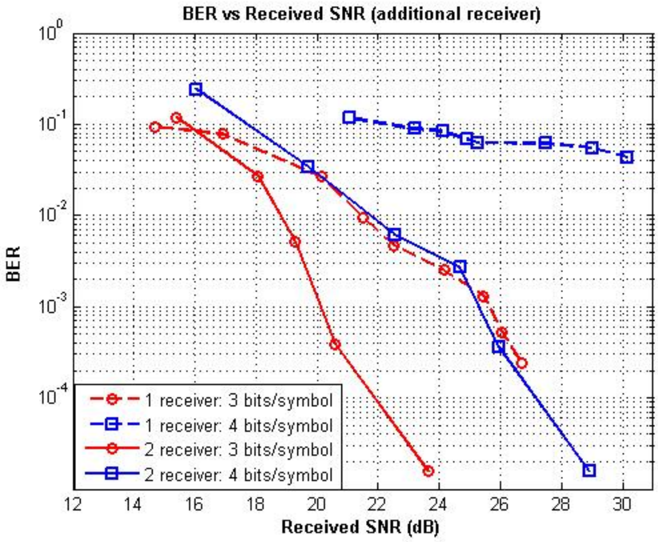

Figure 3.6: *The measured BER vs received SNR results for single and dual receivers at different spectral efficiencies.*

of these channel gains.

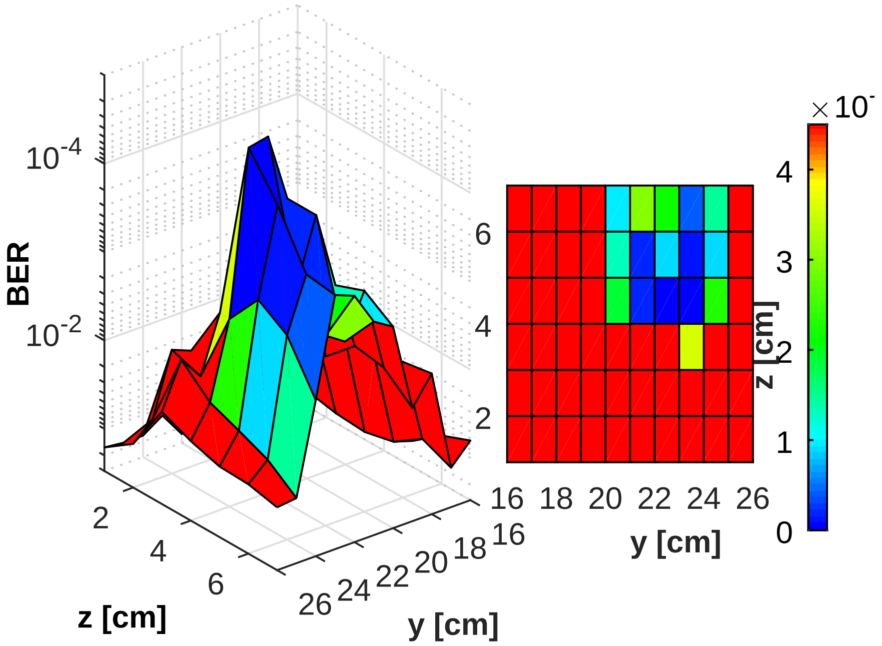

Figure 3.7: *The measured BER with single receiver at different locations within a 60* cm^2 *area.*

The maximum operating spectral efficiency is 4 bits/symbol when 4 μLEDs are used. The analog receiver board has a -3 dB bandwidth of less than 2 MHz, thus no high speed measurement has been carried out using this real-time system. Replacing the receiver boards with higher bandwidth devices can offer higher data rates. Considering the decoder design with FPGA, there is a trade-off between the clock frequency required and the gate source required. For instance, to decode a 4 bits/symbol GSSK signal, it is possible to compare the received signal with the 16 estimation values in series during each symbol cycle or in parallel. The former requires a higher clock source - i.e. 16 times higher than the baud rate to get 1 sample per symbol - while the latter requires more gate source from FPGA in order to operate in parallel. Current system accomplishes the procedure in series, however, the gate source is also limited. Thus real-time GSSK operation with orders higher than 4 is not implemented.

3.4 16-by-4 GSSK Set-up with APDs

3.4.1 Experimental Set-up

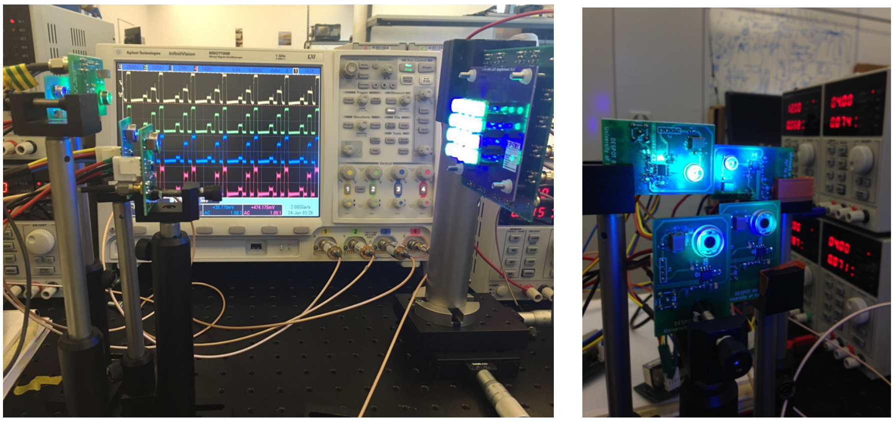
(a) (b)

Figure 3.8: *(a) 16-by-4 System set-up with 16 μLEDs and 4 APD receiver boards; (b) the 4 custom-designed APD receiver boards.*

The experimental set-up is shown in Figure 3.8. At the transmitter side, a GSSK encoder is implemented with the Nexys3 board, which features the Xilinx Spartan-6 LX16 field programmable gate array (FPGA) and offers a higher system clock compared to MARK-1 which is introduced in the previous section. The 16 μLEDs are plugged into a daughterboard with 1 cm distance between each other forming a 4 by 4 array. The daughterboard is attached to a motherboard which connects to a DC power supply and 16 individual output ports of the FPGA. Each μLED has a plastic aspheric lens to collimate the light and this reduces the semi-angle to 4 degrees. The arrangement of the μLED array can be illustrated in Figure 3.9. The 16 μLEDs are numbered from 1 to 16 starting from the top left corner to the lower right corner. At the

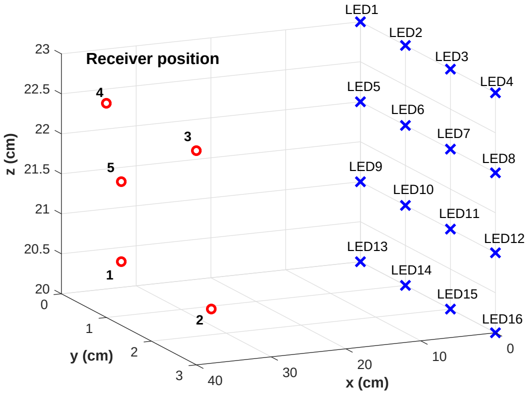

Figure 3.9: *Illustration of the arrangement for both μLED array and APD receiver boards. Up to 16 μLEDs are used and 5 possible receiver locations are chosen.*

receiver end, up to 4 individual APD receiver boards are available, with no lens on the receiver side being used in this work. The receivers are set to different positions regarding different experiments and the coordinates of these positions are given in Table 3.3 and also illustrated in 3.9. The link distance is either 35 cm or 37 cm depending on the receiver positions.

Table 3.3: *Coordinates of the 5 chosen receiver positions*

Receiver position	Coordinates (cm)
1	(35, 0.5, 20.5)
2	(35, 2.5, 20.5)
3	(37, 2.5, 22.5)
4	(37, 0.5, 22.5)
5	(35, 0.5, 21.5)

The data packets for measurements are generated by the FPGA and contain three parts: the synchronisation symbols, channel estimation symbols and data symbols. The synchronisation symbols are used to trigger the signal. In the channel estimation part, all the possible combinations of LEDs are activated sequentially and this entire sequence is sent repeatedly for 4 cycles. The purpose of this is to train the ML decoder by capturing the power level for each known GSSK symbol. After the channel estimation symbols, 6.4×10^4 bits of data are encoded and sent. In the designed FPGA encoder, varying the duty cycle τ is supported, which shows that the encoder is a potential candidate for VLC application where dimmed control is required. Figure 3.10(a) and Figure 3.10(b) show the examples of captured signals when $\tau = 0.5$ and $\tau = 1$ respectively running at 4 bits/symbol. The x-axis refers to time while the y-axis represents the voltage values of received signals.

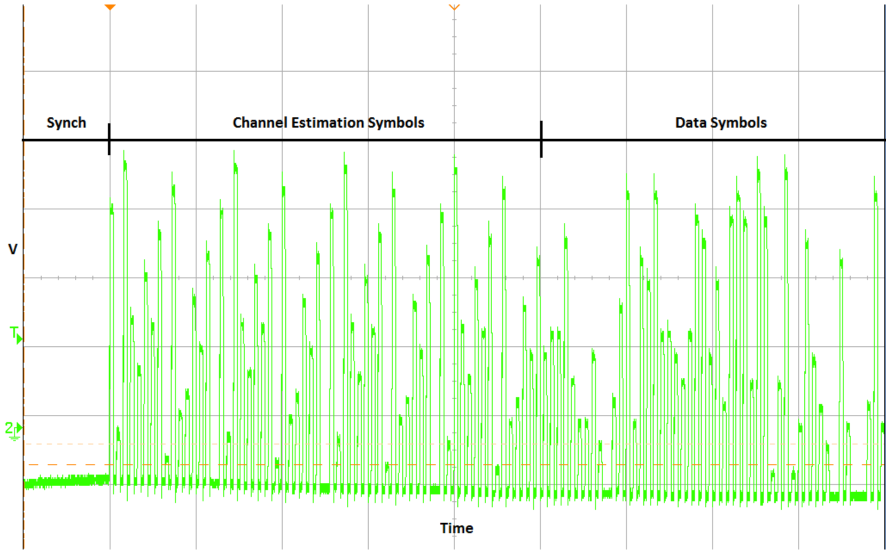

(a)

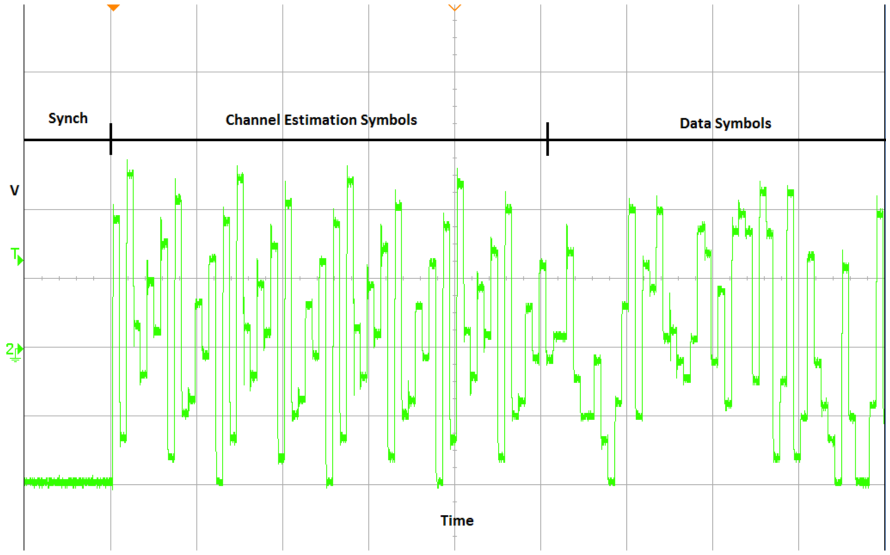

(b)

Figure 3.10: *Captured signal showing 4 bits/symbol operation with: (a)* $\tau = 0.5$*; (b)* $\tau = 1$.

There are four sets of measurements. The first experiment measures the channel gain between 4 selected LEDs and 2 receivers at different positions. The result shows how each channel gain differs from the others. The second measures the bit error ratio (BER) performance when using a single receiver and multiple transmitters. The third experiment shows how the BER performance behaves when setting the receiver at different positions and using more receivers. The last experiment employs the entire 16 LEDs and 4 receivers measuring the BER performance against the achieved data rate while running at different spectral efficiencies. The switching frequency for each LED is set to 5 MHz where 5 Msamples are sent per second.

3.4.2 Results and Discussion

The experiments evaluate the channel gains and BER performances at different spectral efficiencies. Four μLEDs are chosen from the array for the first three experiments. The LED numbers and their coordinates are given as: LED1 (0, 0, 23), LED2 (0, 1, 23), LED9 (0, 0, 21) and LED10 (0, 1, 21) (in cm). As the direction of each LED is irregular when being plugged into the daughterboard, all four LEDs are tilted towards position 5, forming an overlapping covering area.

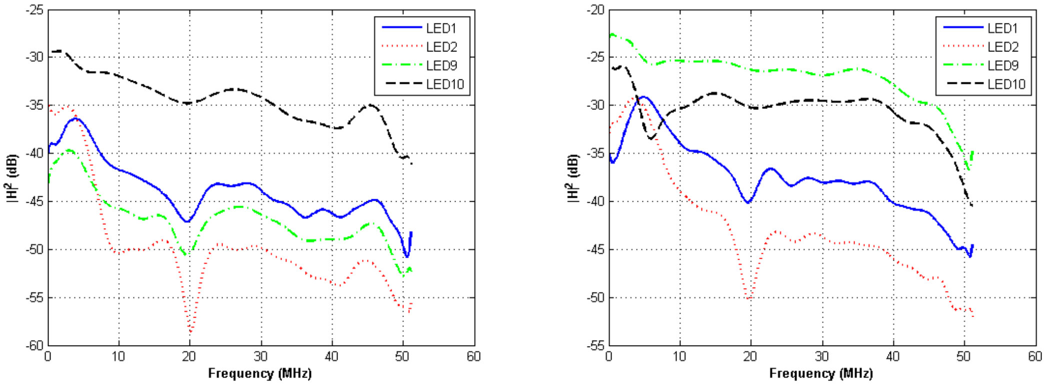

(a) (b)

Figure 3.11: *Measured channel gain with 4 LEDs and single receiver: (a) receiver at position 1; (b) receiver at position 2.*

In the first experiment, the APD receiver is set at position 1 and then the channel gains between each of the four LEDs and the receiver are measured. The result in Figure 3.11(a) shows the natural differences of channel gains between each LED and the same receiver. These differences are exploited at the receiver to estimate which symbol has been transmitted. The measurement is then repeated by setting the receiver to position 2. The result is shown in Figure 3.11(b). By comparing the two figures, it is clear that the channel gain also differs between links from one LED to receivers at different positions. This is a key feature exploited by GSSK. If receiver mobility is to be supported, the system needs to periodically send training information in order to be able to decode information correctly. The dip in both figures at 20MHz is possibly caused by the APD boards. The surface of the APDs are metal and these boards are put quite close which may form the on board capacitance which may affect the channel gains.

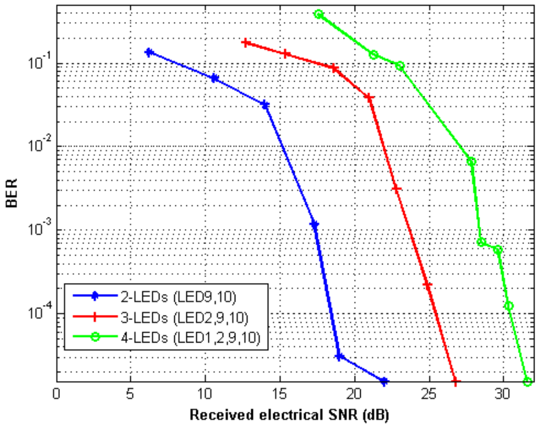

Figure 3.12: *Measured BER vs received electrical SNR for operation of single receiver with 2, 3 and 4 LEDs.*

In the second experiment, the error performance is evaluated when using one single receiver and multiple transmitters. Figure 3.12 shows the BER performance against the received electrical signal-to-noise ratio (SNR) when using 2, 3 and 4 transmitters which results in a spectral efficiency of 2 bits/symbol, 3 bits/symbol and 4 bits/symbol respectively. The channel gain for LED1, LED2, LED9, LED10 are measured and then normalised giving [0.14, 0.244, 0.477, 1] respectively. The received signal for each case is similar to PAM signals at the same spectral efficiency. However the received power levels are not equally spaced. When the modulation order is increased, there are more GSSK symbols that need to be distinguished. The results show that when one more LED is used, about 5 dB higher SNR is required to achieve the similar BER of 1.56×10^{-5} for this experimental set-up.

The error performance in the previous experiment is different when the receiver moves. Therefore, in the next experiment, two receivers are put at position 1 and 2. The BER performance is firstly evaluated based on each receiver and then the received signals from both receivers are processed jointly. Results are shown in Figure 3.13 and the measured normalised channel gain values for LED1, LED2, LED9 and LED10 are [0.25, 0.37, 0.15, 1] at position 1 and [0.31, 0.61, 1, 0.79] at position 2. As discussed in Figure 3.11(a) and Figure 3.11(b), the channel gain differs from the same LED set to the receiver at different positions. The result in Figure 3.13 shows that the error performance of GSSK is strongly dependent on the dissimilarity of the channel gain values. In addition, by using two receivers, the error performance is significantly improved.

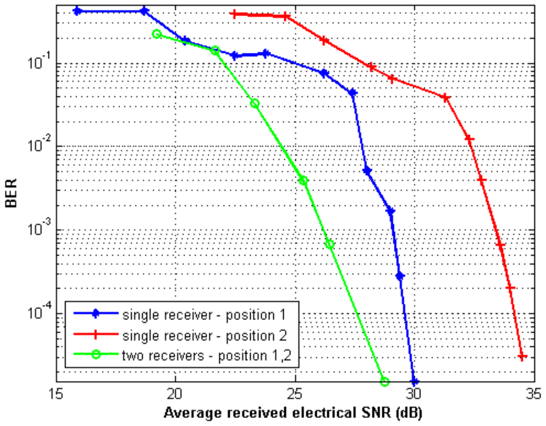

Figure 3.13: *Measured BER vs received electrical SNR for 4 LEDs with different receiver arrangements.*

In the last experiment, all 16 μLEDs and 4 APD receivers are used. The measurements are taken while running GSSK at different spectral efficiencies up to 16 bits/symbol. Results are shown in Table 3.4.

Several switching frequencies for the LEDs are selected from 5 MHz to 100 MHz. For a spectral efficiency of 8 bits/symbol, the measured BER is 1.6×10^{-5} at a switching frequency of 50 MHz (i.e. 400 Mbits/s). When the switching frequency is increased to 100 MHz resulting in a data rate of 800 Mbits/s, the BER degrades to 2×10^{-2}. This is because when the frequency increases, especially beyond the -3 dB bandwidth of the LED, the power gain of each LED drops resulting in a lower received SNR. For a switching frequency of 50 MHz and a spectral efficiency of 12 bits/symbol, the BER is 1.6×10^{-1} which is much higher than that of the case of 8 bits/symbol. As shown in the previous result, it requires higher SNR to achieve the same BER performance at a higher spectral efficiency.

An operation at the maximum spectral efficiency of 16 bits/symbol while using 16 LEDs is demonstrated. The measured BER are 1.6×10^{-5} and 1×10^{-1} for 80 Mbits/s and 160 Mbits/s. There are some restrictions for the current 16 by 4 experimental set-up. Currently only 4 receiver boards are used without using any lens and each of them has a small active area thus there is significant optical power loss. In some links, only a small part of the optical power from the LED is captured by the receiver. For such links when the switching frequency increases, the channel SNR drops significantly thus errors occur. In this work, no lens is used for the received SNR enhancement. One reason for this is that, this work investigates how the natural channel

Table 3.4: *Achieved data rate and BER at different spectral efficiencies*

Spectral Efficiency (bits/symbol)	Data Rate (Mbits/s)	BER
8	400	1.6E-5
8	800	2E-2
12	120	3.6E-4
12	300	8E-2
12	600	1.6E-1
16	80	1.6E-5
16	160	1E-1

gain affect the GSSK performance. As high data rate is not the primary target and it is better for understanding the system limitations without using lenses at such close distance. Even though the achieved data rate is limited, the demonstration still shows the high data rate potential of GSSK.

3.5 Further Implementation with CMOS APD Receiver Chip

3.5.1 System Set-up

An optical imaging-MIMO implementation is reported in [16] using an imaging lens and an integrated CMOS APD receiver. As two implementation of non-imaging GSSK have been presented, it is interesting to see how the system performs with the imaging receiver set-up. At the transmitter end, 4 blue GaN μLEDs are used as shown in Figure 3.14(a). Each μLEDs has a plastic aspheric lens to collimate the light output. At the receiver end, the integrated CMOS APD receiver chip equipped with an imaging lens is used as shown in Figure 3.14(b). This CMOS receiver chip contains a 3$\times$3 array of APD detectors. Each of the APDs has a responsivity of 2.61 A/W at 450 nm [16]. Four of these APDs from the 3$\times$3 array have been used for the 4-by-4 GSSK set-up. The link distance is 40 cm.

3.5.2 Results and Discussion

The 4-by-4 GSSK link provides a spectral efficiency of 4 bits per symbol. The switching frequency has been set to 50 MHz, 80 MHz and 100 MHz which result in the achieved data rate of 200 Mbits/s, 320 Mbits/s and 400 Mbits/s respectively. Examples of the received signals

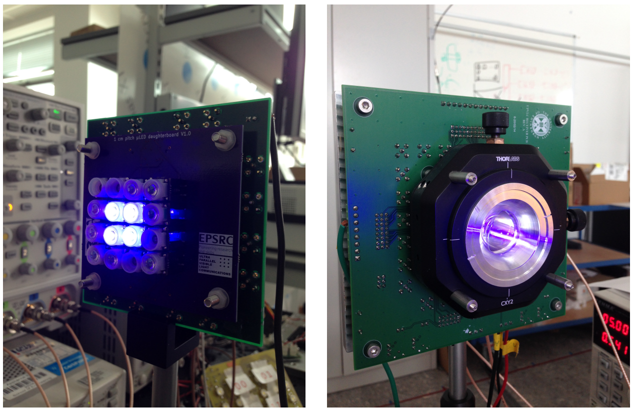

(a) (b)

Figure 3.14: *System set-up: (a) μLED array with 4 transmitters on; (b) CMOS APD receiver board with optics.*

at such switching frequencies are shown in Figure 3.15(a)-(c). The measured BER against the achieved data rate result is shown in Figure 3.15(d). At 200 Mbits/s, a BER of 1.56×10^{-5} is achieved and it increases to 2×10^{-4} when the data rate increases to 320 Mbits/s. It still meets the requirement for practical communication systems when the forward error correction (FEC) coding is applied. The BER decreases to 1.24×10^{-2} when the data rate further increases to 400 Mbits/s.

3.6 Summary

A FPGA based GSSK driver is implemented for the first time. Up to 16 individual optical sources can be directly driven simultaneously. Several GSSK links have been implemented showing the capacity of the driver and the performance of the set-ups. Firstly a real-time GSSK VLC system with μLEDs and PIN PDs is demonstrated for the first time with a FPGA based real-time GSSK decoder being applied. The implementation of both hardware and software are introduced in detail. Several measurements have been carried out to evaluate the system BER performance against different conditions. It is shown that one single receiver is capable of distinguishing 2 and 3 LEDs' GSSK operation with the measured BER of 1.6×10^{-5} and 2.4×10^{-4} giving the spectral efficiencies of 2 bits/symbol and 3 bits/symbol. The BER increases dramatically when the fourth LED is added. However, adding another receiver significantly improves the system performance as shown in the given results with the 3-LED and 4-LED case. The experiments also indicate that the system is relatively flexible against receiver mobility.

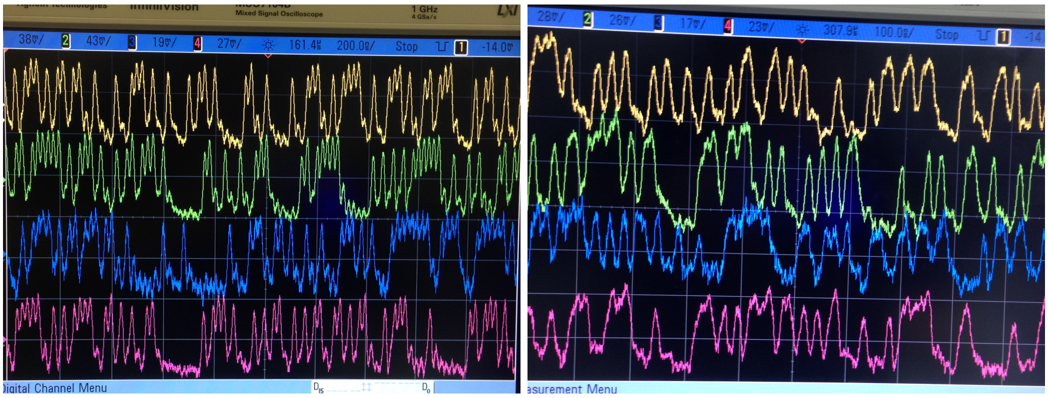

(a) Signal at 200 Mbits/s

(b) Signal at 320 Mbits/s

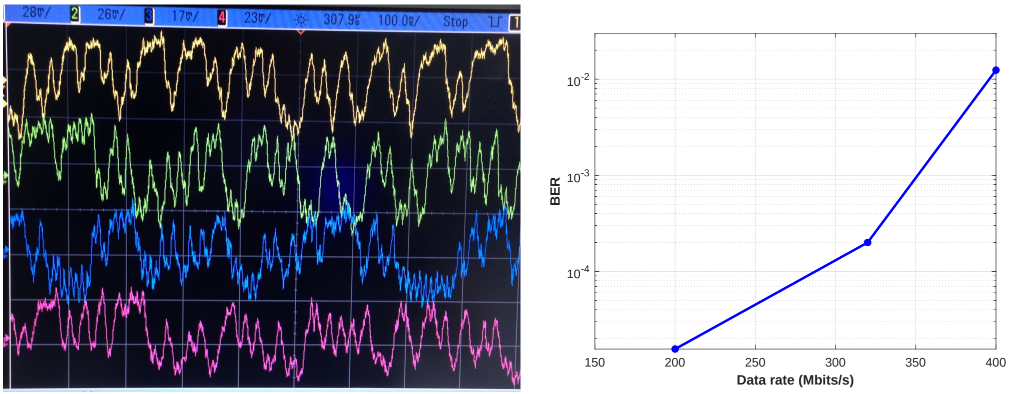

(c) Signal at 400 Mbits/s

(d) BER vs Data rate

Figure 3.15: *(a)-(c) Examples of received signals on scope at 200, 320 and 400 Mbits/s respectively. (d) Measured BER vs data rate.*

The constraint of this proof-of-concept system is also listed which lies in both hardware and software design.

The second experimental set-up of GSSK contains a μLED array and APD receivers, and is demonstrated in this work. An FPGA based GSSK encoder is implemented which is capable of driving up to 16 LEDs. An experiment is carried out showing the differences between the channel gain values of different links. This is the key concept of GSSK. It is shown that the channel gains differs from LEDs to the same receiver or from one LED to different receivers. More experiments are carried out evaluating the BER performance with different set-ups. The BER performance against received electrical SNR is presented in the cases where 2, 3 and 4 LEDs are used with a single receiver. For the demonstrated set-up, it is shown that about 5 dB higher SNR is required when one LED is added to the operation for achieving a similar BER of 1.56×10^{-5}. Results also show that the BER performance varies when receivers change their positions. It is a limitation of GSSK that the error performance is highly dependent on the dissimilarity of the channel gain values. However, the performance can be improved by applying more receivers. It is shown that about 4 dB and 8 dB lower SNR is required for achieving the same BER of 10^{-3} while using two receivers compared to using a single receiver at different positions respectively. The BER versus data rate measurements of applying different spectral efficiencies on a 16 by 4 GSSK set-up indicates the high data rate potential of GSSK. The BER results show that about 10^{-5} is achievable with the current set-up for the spectral efficiencies from 8 bits/symbol up to 16 bits/symbol.

The last experimental set-up uses an imaging receiver which contains a CMOS APD receiver chip and an imaging lens. A 4-by-4 GSSK system has been demonstrated with the spectral efficiency of 4 bits/symbol. At data rates of 200 Mbits/s, 320 Mbits/s and 400 Mbits/s, the achieved BER are 1.56×10^{-5}, 2×10^{-4} and 1.24×10^{-2} respectively. This work shows that GSSK can be operated reliably in a small spot area while offering high data rates.

This study has shown the potential of the GSSK scheme as a candidate for VLC applications. The implementation complexity is low compared to other multi-level multi-carrier modulation techniques. No DAC is required which also reduces the cost. It has been shown that the GSSK system is relatively flexible against receiver mobility. Moreover, this flexibility can be further improved if an adaptive GSSK mapping technique is introduced and this concept is a possible direction of future study.

Chapter 4

Ultra-high Speed WDM based VLC System with off-the-shelf LEDs

4.1 Introduction

Different communication system structures have been adopted for visible light communication (VLC), in order to increase the achievable data rate and spectral efficiency [73–75]. Orthogonal frequency division multiplexing (OFDM) is regarded as a natural choice of modulation scheme due to its high spectral efficiency and immunity to channel frequency selectivity. The relatively low bandwidth of common phosphor-coated white light emitting diodes (LEDs) (i.e., several MHz) causes a significant limit on the achievable data rate [8]. This limitation originates from the slow response of the yellow phosphor coating. Therefore, several single colour LEDs, without any coating, with much larger bandwidths can be utilised for both communication and illumination. A combination of three or four colours can be used for both white illumination as well as high data rate wireless communication. This is referred to as wavelength division multiplexing (WDM), where each single colour LED can be modulated independently. As a result, parallel data streams can be transmitted leading to a high communication data rate.

Over the past few years, several giga-bit-per-second experimental WDM-VLC demonstrations have been reported [76]. Laser-based experiments have shown achievable data rates of up to 25 Gb/s for underwater VLC [54, 77–80]. However, high power lasers are potentially hazardous as they can burn the retina of the eye. So laser-based VLC requires the consideration of eye-safety limitation which may significantly reduce the achievable data rates. An ”eye-safe” data-rate of 8.8 Gb/s over 50 cm is reported in [81]. On the other hand, eye-safety is normally not an issue in LED-based VLC, but the available electrical bandwidth and optical power are much smaller in LEDs. Data rates up to 7.36 Gb/s are reported with custom-made micro-sized gallium nitride (GaN) LEDs (μLEDs) as the light source [82, 83]. μLEDs have much higher bandwidth but lower output optical power compared to commercially available LEDs. The combination of several single colour LEDs/μLEDs with WDM has enabled data rates of up to 10.7 Gb/s [18, 53, 84, 85].

In this Chapter, a record data rate of 15.73 Gb/s over 1.6 m link distance is reported using available inexpensive off-the-shelf LEDs at a price of less than £0.40. WDM is used with four LED colours, namely - red (R), green (G), blue (B) and yellow (Y). The single colour beams are combined at the transmitter side (Tx) and separated at the receiver side (Rx) using three commercially available dichroic mirrors. Moreover, OFDM with adaptive bit loading [86] is utilised to maximise the spectral efficiency of each LED. The chosen LEDs are designed for illumination rather than data communication, and thus, the system should be carefully optimised to reduce the effect of LED non-linearity, which can significantly affect the performance of OFDM. Also, the effect of crosstalk need to be addressed. A low lost custom-designed receiver circuit with inexpensive components is presented. Such receivers are applied to the WDM system and the trade-off between the system capacity and receiver complexity is investigated. This alteration results in 7.67 Gb/s of data rate.

4.2 System Design

In this section the basics of the data transmission method and elements of the communication system are presented. The optimisation procedure is also introduced.

4.2.1 Data Transmission

OFDM is proved to be a spectrally efficient modulation scheme and a favourable choice in VLC [87, 88]. Among possible choices of OFDM variants for VLC, direct current biased optical OFDM (DCO-OFDM) is chosen due to its simplicity and high spectral efficiency [73]. Since IM/DD is used in VLC, the signal should be both real and non-negative. Thus, Hermitian symmetry is imposed on the symbols of a subcarrier block $X[k]_{k=1}^{N_{\mathrm{FFT}}}$, where N_{FFT} is the number of subcarriers. This halves the number of available subcarriers for data transmission as $X^{*}[k] = X[N_{\mathrm{FFT}} - k]$. Also, $X[0] = X[N_{\mathrm{FFT}}/2] = 0$ because of the direct current (DC) bias. The resulting time domain signal is then clipped to avoid large values which increases the effect of non-linearity or may harm the LED. The upper and lower clipping values are set to $+3.2$ and -3.2 times of the signal's standard deviation. WDM can be utilised including several visible light wavelengths that allow parallel transmission of OFDM data streams at each wavelength.

Filters are used to separate signals at different wavelength. The corresponding channel model for ith wavelengths can be expressed as

$$y_i(t) = g_i\left(x_i(t)\right) + n_i(t), \tag{4.1}$$

where $g_i(.)$ is the overall channel, including the effects of the optical channel and front-end devices. $n_i(t)$ is an additive white Gaussian noise (AWGN) consisting any noise source, such as thermal and shot noise. It can be assumed that $g_i\left(x_i(t)\right) = h_i(t) * w_i\left(x_i(t)\right)$, where $h_i(t)$ is the optical channel response and $w_i(.)$ is the non-linear distortion of the LED [89]. It is shown that this non-linearity distortion can be modelled as a Gaussian process [90]. Usually, the LED can be assumed to be the dominant source of non-linearity. As it will be detailed in Section 4.2.2, the non-linearity of photoreceivers, amplifiers and other components are negligible compared to the LED.

Different phenomena in an experimental set-up affects the overall frequency response of the communication system and makes it frequency-dependent. For instance, the overall frequency response can be affected by: the interference from ambient light sources or other optical wavelengths, the frequency-dependent response of front-end devices, and the optical channel itself. Therefore, the modulation order can be selected adaptively at each subcarrier to maximise the achievable data rate at a target bit error rate (BER) [86]. Thus, SNR estimation is required at each subcarrier prior to data transmission. The channel and available SNR at each subcarrier SNR_k is estimated using pilots composed of several OFDM blocks. Details of the estimation method can be found in [54]. It should be noted that the overall communication channel is considered in this SNR estimation including all the affecting phenomena, such as attenuation, noise and non-linear distortion. M_k-QAM modulation format is considered where the modulation order at each subcarrier M_k is determined by the available SNR and target BER. The BER of a M_k-QAM modulation format with SNR_k can be approximated as [91]:

$$\begin{aligned} \mathrm{BER}\left(M_k, \mathrm{SNR}_k\right) \simeq & \frac{4\left(1 - \frac{1}{\sqrt{M_k}}\right)}{\log_2 M_k} \\ & \times \sum_{l=1}^{\min(2,\sqrt{M_k})} \mathrm{Q}\left((2l-1)\sqrt{\frac{3\mathrm{SNR}_k}{2\left(M_k - 1\right)}}\right) \end{aligned} \tag{4.2}$$

where $\mathrm{Q}(.)$ is the Q-function. Therefore, using the iterative algorithm for bit loading, the modulation orders M_k are determined, and the overall data rate is given by [54]

$$R = \frac{\sum_{k=1}^{\frac{N_{\mathrm{FFT}}}{2}} \log_2 M_k}{(N_{\mathrm{FFT}} + N_{\mathrm{CP}})/2B}, \tag{4.3}$$

where B is the single-sided modulation bandwidth of the system, and N_{CP} is the cyclic prefix size. It should be emphasised that after SNR estimation and adaptive bit loading, multiple OFDM blocks are transmitted through the communication channel according to the determined bit loading, and the actual BER is then measured. This ensures that the overall BER of the system is below the target BER. In this paper, a hard decision forward error correction coding (HDFEC) threshold of 3.8×10^{-3} which imposes 7% coding overhead [92] is considered.

4.2.2 Experimental Set-up

In this section, the details of the experimental set-up are presented. WDM can be realised in different structures. For instance, only bandpass filters at the receiver side may be used for detecting each wavelength individually [53], or a combination of bandpass filters at the Rx and dichroic mirrors at the Tx may be selected [54]. In this work, dichroic mirrors are used in both Tx and Rx because the spectrum of each single colour LED is large and available narrowband bandpass filters will result in significant power loss. Dichroic mirrors are basically high-pass filters. The wavelengths larger than a certain value travel through and the shorter wavelengths are reflected. Moreover, it is possible to efficiently (i.e., achieve minimal loss of optical power) combine and separate all four colours using the same combination of condenser lenses and dichroic mirrors respectively at Tx and Rx.

The LEDs chosen in this work are the commercial products by Vishay Semiconductors. There are two key features which lead to this decision: the high optical output power and smaller diode size. In general, the smaller diode size forms smaller diode capacitance which leads to higher bandwidth. With higher output optical power, higher optical signal power can reach the photodetector after travelling through the optical channel and multiple dichroic mirrors. The chosen LEDs are designed for small-scale high brightness applications [93]. The model number of RGBY LEDs are L1: VLMS1500-GS08, L2: VLMTG1300-GS08, L3: VLMB1500-GS08 and L4: VLMY1500-GS08, respectively. The dimensions of the LEDs are $1 \times 0.5 \times 0.35$ mm for red, blue and yellow LEDs, and $1.6 \times 0.8 \times 0.8$ mm for the green LED. Figure 4.1 shows the optical power spectrum of the LEDs used in this work at their nominal driving currents.

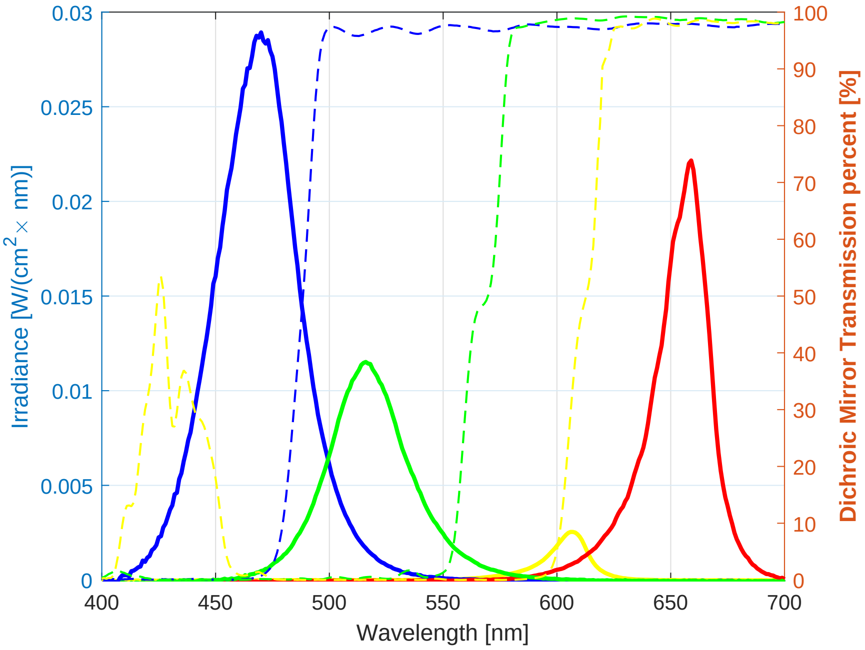

Figure 4.1: *Measured optical spectrum of RGBY sources and the transmission percent of the dichroic mirrors.*

Comparing to the RGB colours, the irradiance of Y LED is much smaller. Even though, this model of Y LED is still used for its small size, and thus, high bandwidth which is shown in the following sections.

Three dichroic mirrors are chosen based on the measured spectrum of LEDs. The transmission percent of the chosen dichroic mirrors is shown in 4.1 [94]. The arrangement of the dichroic mirrors is illustrated in Figure 4.2. One dichroic mirror (M1: Thorlabs DLMP605L) is used to reflect the yellow signal while it passes the red signal. The transmission band for this mirror is 620-800 nm with a cut-off wavelength of 605 nm. Another dichroic mirror (M2: Thorlabs DLMP567L), with transmission band 584-800 nm and cut-off wavelength 567 nm, is used to reflect the green signal while it passes the other two colours. The third one, (M3: Thorlabs DMLP490L), with transmission band 505-800 nm and cut-off wavelength 490 nm, reflects the blue signal and passes the others. It can be seen from Figure 4.1 that the optical crosstalk between each colour is attenuated by the dichroic mirrors. However, M1 is sub-optimal for the Y LED as only a part of light has been reflected towards the photodetector while the other part of light travelling through the mirror. It should be noted that mirrors are chosen among commercially available dichroic mirrors.

The system block diagram and pictures are shown in Figure 4.2. The DCO-OFDM signal generation and analysis is performed on a personal computer (PC) using MATLAB. Generated signals are sent to the arbitrary waveform generator (AWG: Keysight M8195A). The sampling rate of the AWG is 16 GSa/s and the resolution of the digital-to-analog (DAC) unit of the AWG is 8 bits. Each output signal from AWG is amplified by an amplifier module (Amp: Mini-Circuits ZHL-1A-S+) and fed into Bias-Tees (Mini-Circuits ZFBT-4R2GW). The Bias-Tee is used to combine the OFDM information signal with the DC bias which comes from a DC power supply. The Bias-Tee's output is connected to the LED source. Since the half-power semi-angle of LEDs are wide (i.e., about 65° [93], aspheric condenser lenses (A1-4: Thorlabs ACL4532) are used at Tx to collimate the output light of each LED. At the receiver side at a link distance of 1.6 m, the same configuration of mirrors (M4-6) and aspheric condenser lenses (A5-8) is applied to separate each colour and focus the light into the detection area of the high bandwidth positive-intrinsic-negative (PIN) diode photo detector (PD: New Focus 1601 AC). This receiver has a -3 dB bandwidth of 1 GHz. The gain of the receiver built-in transimpedance amplifier (TIA) is 10 V/mA. The received signal is captured by a high-speed oscilloscope (OSC: Agilent DSA90804A) and then sent back to PC to be processed.

4.3 Data Transmission Results

In this section, details of the data transmission results are presented. First, the system optimisation procedure is introduced with a comparison of multiple experimental results. Next, the full WDM operation is demonstrated and results are presented in detail. Finally, an inexpensive, low complexity receiver circuit is presented and used to investigate the change in achievable data rate against a lower receiver implementation complexity.

4.3.1 System Optimisation

As the chosen LEDs are designed for illumination rather than data communication, thus, system parameters, such as LED bias points and signal peak-to-peak amplitude, should be carefully optimised to reduce the effect of LED non-linearity, which can significantly affect the performance of OFDM. In addition, the OFDM parameters should be optimised for the LEDs' characteristics as well as the arrangement of the mirrors.

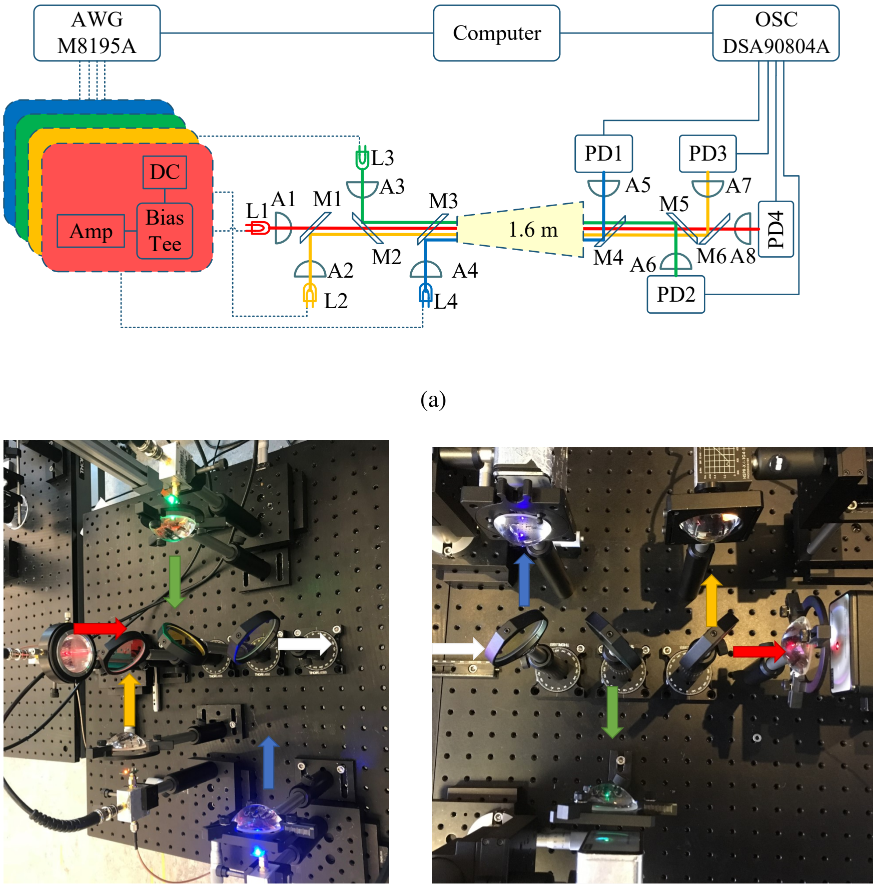

(a)

(b)

(c)

Figure 4.2: *(a) Block diagram of the experimental WDM system, (b) Picture of the set-up at the transmitter side (Tx), (c) Picture of the set-up at the receiver side (Rx).*

4.3.1.1 LED Driving Conditions

One crucial parameter of the experiment is the driving current and signal peak-to-peak amplitude for each LED which determines the available signal amplitude range and the distortion caused by non-linearity. Since these LEDs are manufactured for purposes other than data communication, their communication characteristics differ for each model. It can be seen in Figure 4.3 that the output powers of LEDs are significantly different, and for instance, the output power of the yellow LED is small compared to other colours. Therefore, it is essential to carefully measure the effect of different driving points and choose the optimum point.

As stated before, driving points of LEDs determine achievable data rates and output optical powers. The driving point of each LED is found so that the amount of non-linear distortion is minimised, and consequently, the available SNR for data transmission is maximised. When the

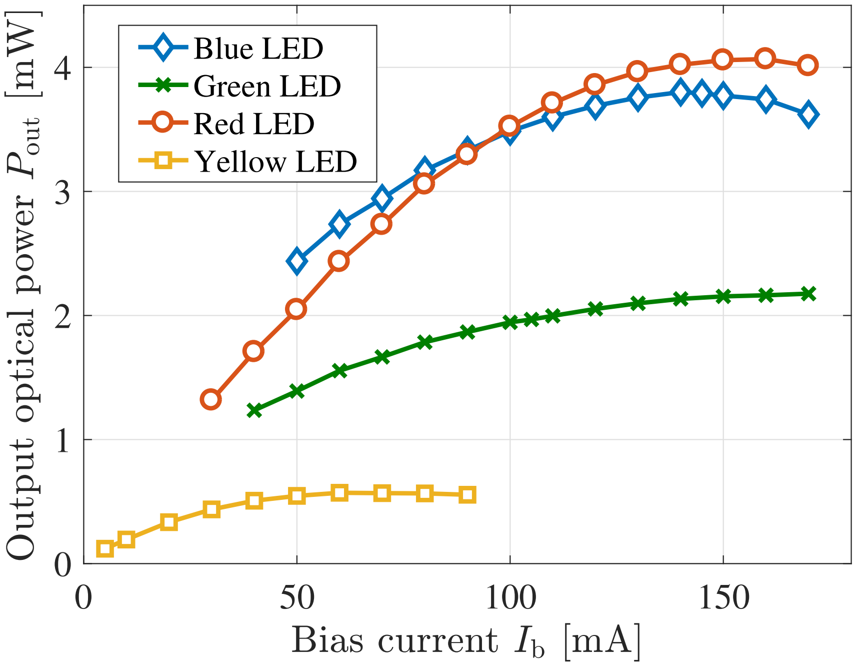

Figure 4.3: *Measured optical power output of RGBY LEDs at different driving currents.*

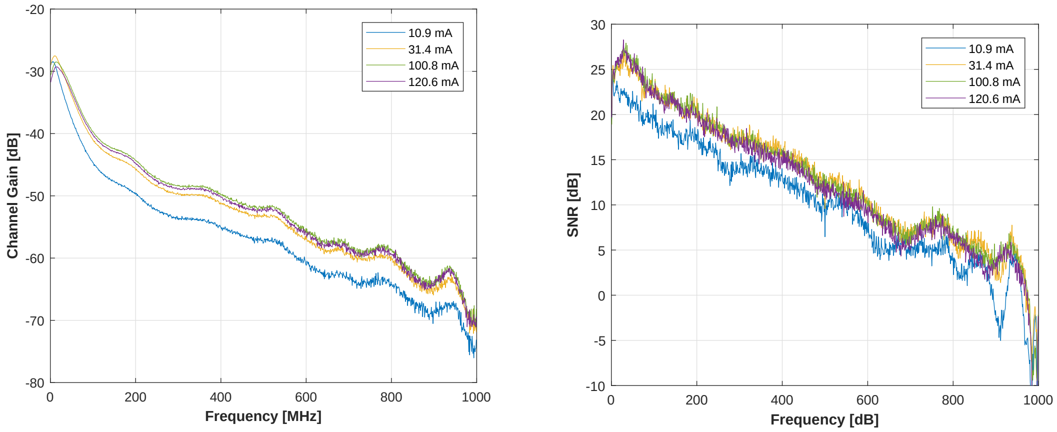

(a)

(b)

Figure 4.4: *Measured results for red LED at different I_{b}: (a) channel gain, (b) SNR.*

driving point is selected, the OFDM signal can be scaled to fit in the linear operation region of each LED. This is performed by adjusting the maximum peak-to-peak voltage (V_{pp}) at the output of the AWG. Note that the signal is amplified after the AWG before being applied to LEDs. The overall gain from AWG to LEDs is about 13 dB including losses in components such as the bias-Tee.

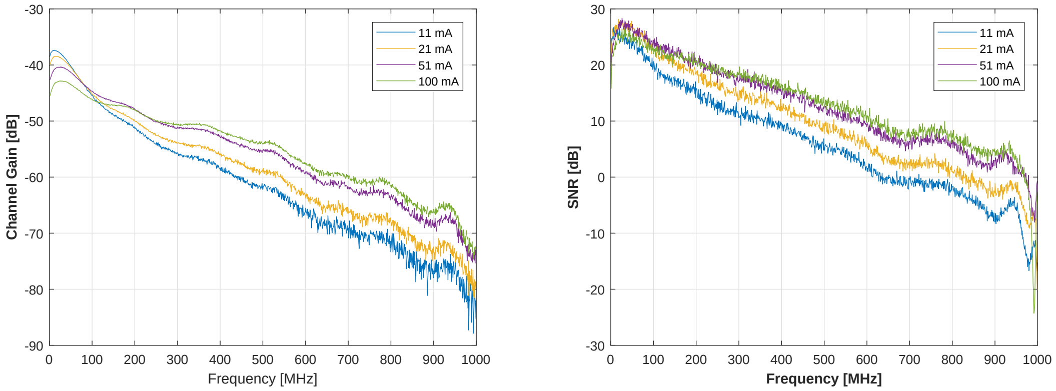

(a) (b)

Figure 4.5: *Measured results for green LED at different I_b: (a) channel gain, (b) SNR.*

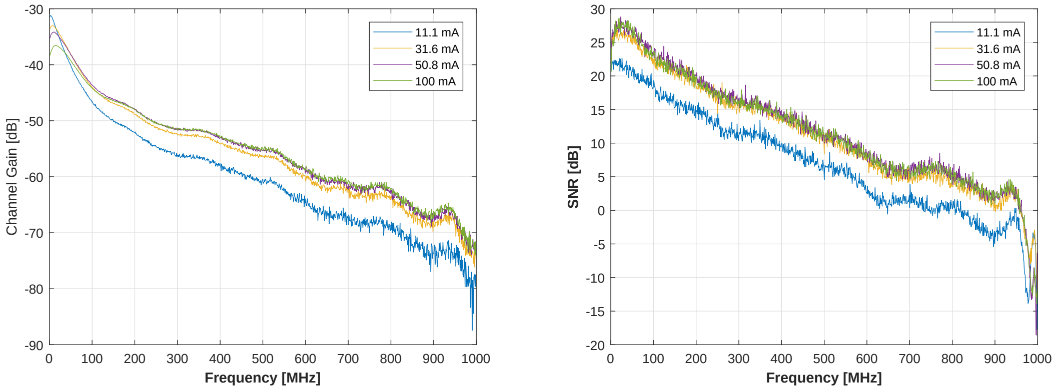

(a) (b)

Figure 4.6: *Measured results for blue LED at different I_b: (a) channel gain, (b) SNR.*

The same experimental set-up, as in Figure 4.2, is used for driving point optimisation. The modulation bandwidth is 1 GHz. First, the minimum possible V_pp of the AWG, equal to 75 mV, is chosen to minimise the non-linearity distortion of LEDs. Next, the bias current I_b is gradually increased and, the channel gain, SNR and data rate are measured. Results for red LED with several bias current points are shown in Figure 4.4. It shows within the bias current region of 10 - 100 mA, higher I_b leads to higher bandwidth and higher SNR values. When I_b increases to 120 mA, both channel gain and SNR reduce which is possibly due to the LED working outside the linear operation region.

The same measurements have been carried out for the other colours. Figure 4.5 and Figure 4.6 show the results for green and blue LED respectively. Similar trends have been observed

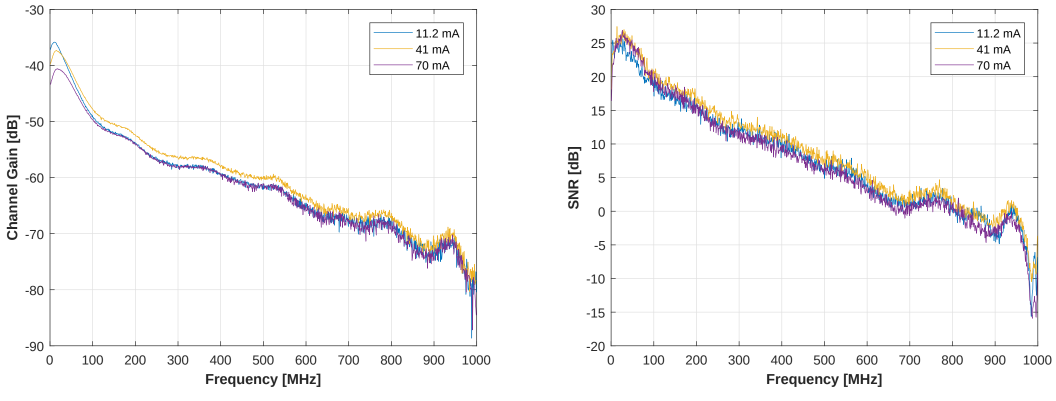

(a) (b)

Figure 4.7: *Measured results for yellow LED at different I_b: (a) channel gain, (b) SNR.*

in both green and blue LED while the channel gain in green is flatter than that of the red and the blue LEDs. As shown in Figure 4.7 for measuring the yellow LED, both channel gain and SNR are optimised at around 40 mA bias current and then start decreasing when the bias current increases. The data rate results are shown in Figure 4.8 and it can be seen that each LED demonstrates different behaviour. Maximum data rates are found at $I_\mathrm{b} = 100$ mA for RGB LEDs and $I_\mathrm{b} = 40$ mA for the yellow LED. The bias voltages of RGBY LEDs are, respectively, 2.38 V, 3.85 V, 4.01 V, and 2.15 V.

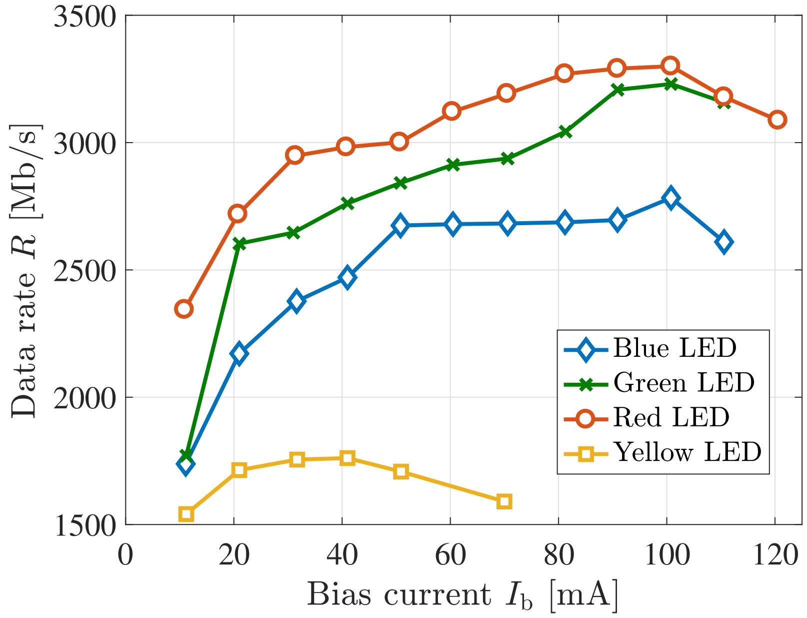

Figure 4.8: *Measured data rates for RGBY LEDs at different I_b.*

At the selected operating points of LEDs, the optimum V_{pp} for each LED is also found by gradually increasing its value and taking measurements. Figure 4.9 shows the measured channel gain and SNR for red LED. It shows the increasing V_{pp} leads to a higher SNR values until the signal amplitude reaches the the dynamic region of the LED source. In addition, it is also shown that the channel gain curve shifts up when V_{pp} increases. However, if considering the -3 dB bandwidth, the value roughly remains the same. This shows that the bandwidth of the LED device is determined by the selection of driving current and the V_{pp} is affecting the achievable SNR. Results for the G, B and Y LEDs are shown in Figure 4.10-4.12. Similar trends have been observed.

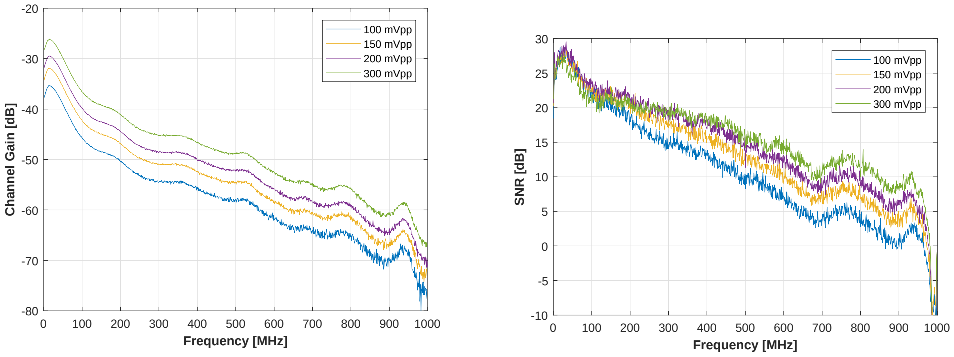

(a) (b)

Figure 4.9: *Measured results for red LED with different* V_{pp}*: (a) channel gain, (b) SNR.*

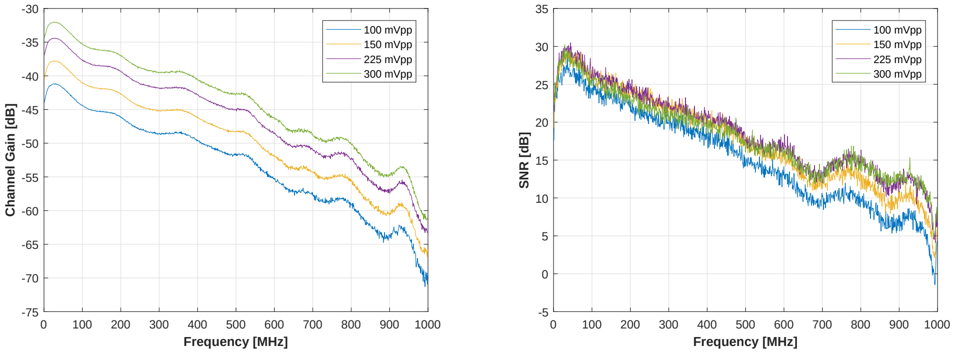

(a) (b)

Figure 4.10: *Measured results for green LED with different* V_{pp}*: (a) channel gain, (b) SNR.*

The corresponding data rate results are demonstrated in Figure 4.13. The optimum values of V_{pp} are 300 mV for red, blue and yellow LEDs, and 225 mV for the green LED. Note that the signal is amplified after the AWG before being applied to LEDs. As stated before, the overall gain from AWG to LEDs is about 13 dB. Therefore, the operation point of each LED is

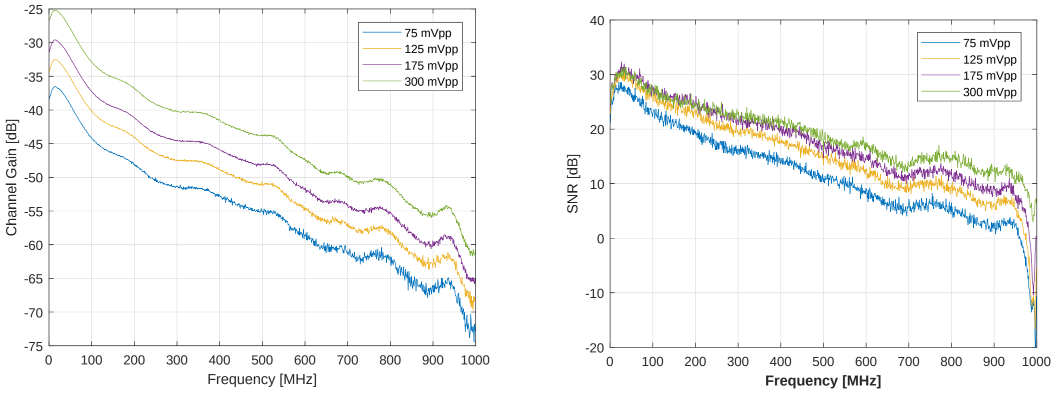

(a) (b)

Figure 4.11: *Measured results for blue LED with different* V_{pp}*: (a) channel gain, (b) SNR.*

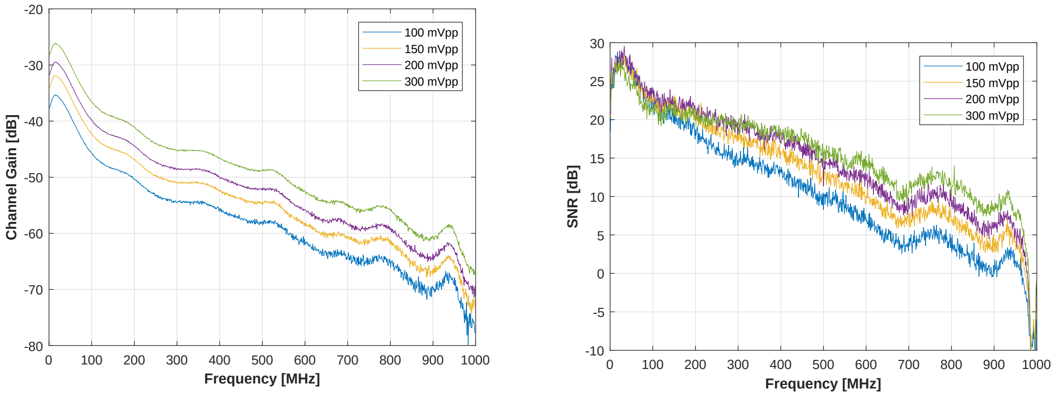

(a) (b)

Figure 4.12: *Measured results for yellow LED with different* V_{pp}*: (a) channel gain, (b) SNR.*

determined which results in the highest achievable data rate.

4.3.1.2 Arrangement of Dichroic Mirrors

A study on the placement of the dichroic mirrors has been carried out. The red beam is designed to pass through all the dichroic mirrors. The angle ψ_{dm} is defined as the incident angle when red beam reaches the dichroic mirror. The ψ_{dm} can be adjusted by rotating the dichroic mirrors and the corresponding positions of the front-end components in other channels would change. However, the position of red LED and the PD4 are fixed, and thus, it is necessary to investigate how the ψ_{dm} would affect the achievable data rate in red link. A measurement set-up shown in Figure 4.14 is implemented. The dichroic mirror M1 is used and the positive ψ_{dm} is defined

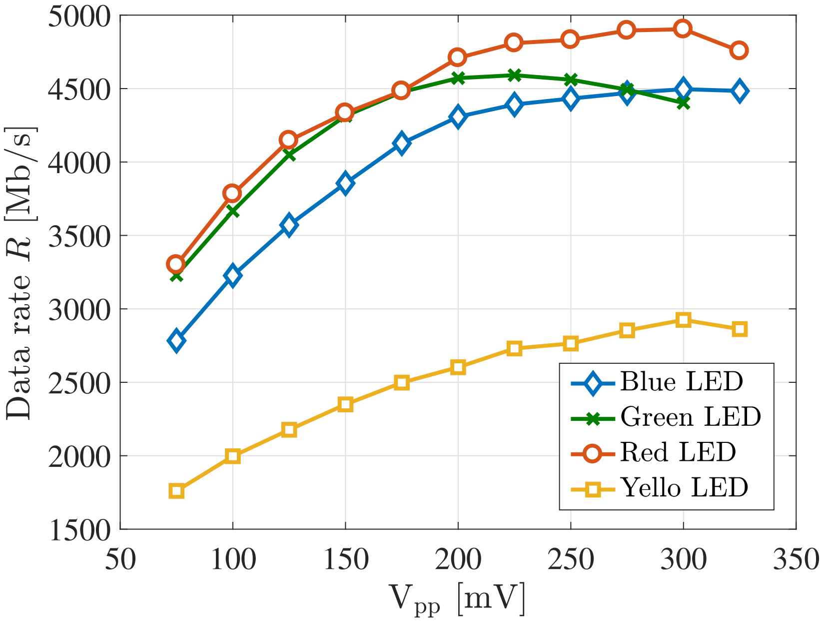

Figure 4.13: *Measured data rates for RGBY LEDs at different* V_{pp}.

when the M1 rotates clockwise. The measured results are shown in Figure 4.15. The worst position for achievable data rate is when $\psi_{\mathrm{dm}} = 0°$ and the maximum data rate is achieved when $\psi_{\mathrm{dm}} = 45°$. Based on this result, the placement of the dichroic mirrors are fixed as shown in Figure 4.2.

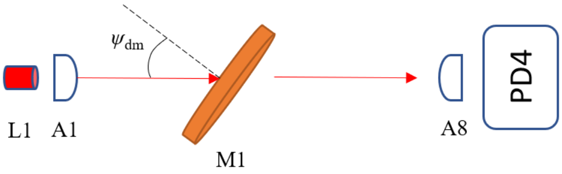

Figure 4.14: *Illustration showing the placement of* M1 with an incident angle of ψ_{dm} .

4.3.2 Results for Full WDM Operation

After the system parameters being optimised, the data transmission measurement is carried out with a full WDM operation. The summary of the data rate measurement results are provided in Table 4.1. An aggregate bit rate 16.92 G/s is achieved which reduces to 15.73 Gb/s after removing the 7% HDFEC coding overhead. It can be seen that the BER is below the threshold

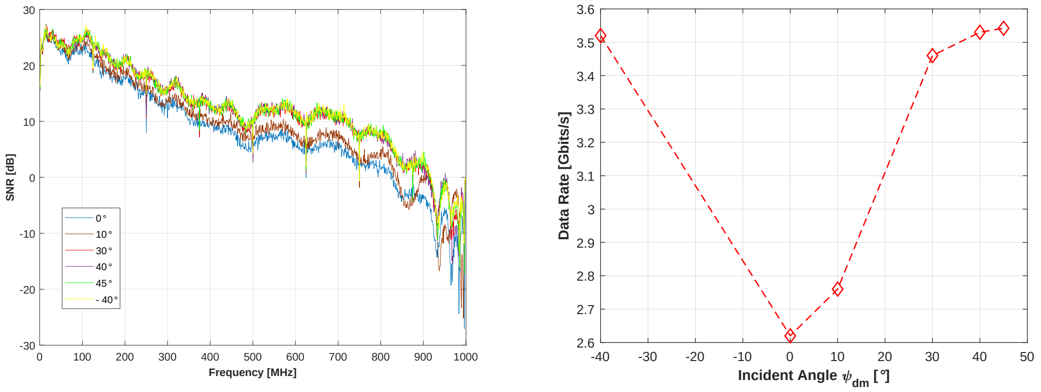

(a)

(b)

Figure 4.15: *Measured results for different incident angle ψ_{dm}: (a) SNR, (b) data rates.*

of 3.8×10^{-3} for all LEDs. The number of active subcarriers N_{act} (i.e., non-zero modulation order) and the output optical power P_{out} of each LED is also included in Table 4.1. The data rate for the white LED of the same series (VLMW1300-GS08) was also measured using the same procedure (a direct link and no dichroic mirror) for comparison with the aggregate data rate achieved with the WDM system. It was observed that only 3.53 Gb/s can be achieved with a BER of 1.2×10^{-3}. The measured output optical power of the white LED was 7.13 mW. This implies that while the output optical power of the white LED is 42% lower that the aggregate output optical powers of RGBY LEDs, its measured data rate is 79% lower. This confirms that utilising WDM significantly increases the power efficiency of VLC systems. The chromaticity diagram with measured values is also shown in Figure 4.16. The mixture colour of the RGBY beams is illustrated while the measured value for the white LED (VLMW1300-GS08) is also presented. Adjusting the output power of the individual RGBY LED by controlling the bias current, the mixed colour can be modified and white illumination is possible to be produced.

Table 4.1: *Measured results of the WDM system.*

	P_{out} [mW]	N_{act}	BER	R [Gb/s]
Red	3.52	890	0.0025	4.904
Green	1.94	887	0.0027	4.591
Blue	3.49	865	0.0036	4.796
Yellow	0.5	811	0.0028	2.925

The overall frequency responses of the system for each colour are depicted in Figure 4.17. The measured SNR and bit loading results are also shown in Figure 4.18. Frequency responses

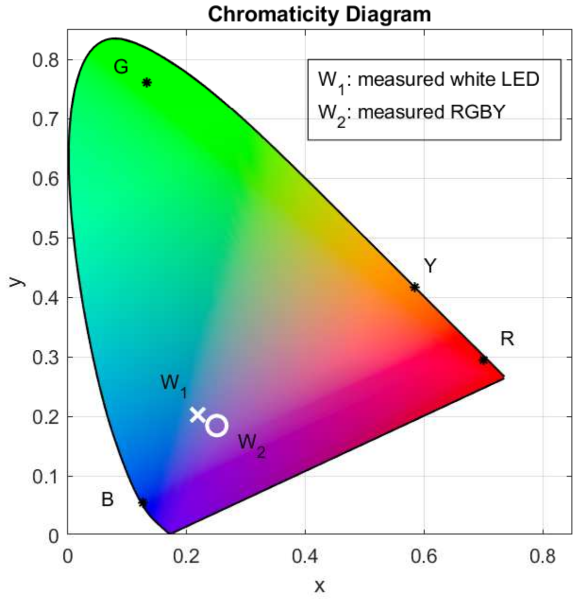

Figure 4.16: *Chromaticity diagram for the measured RGBYW LEDs.*

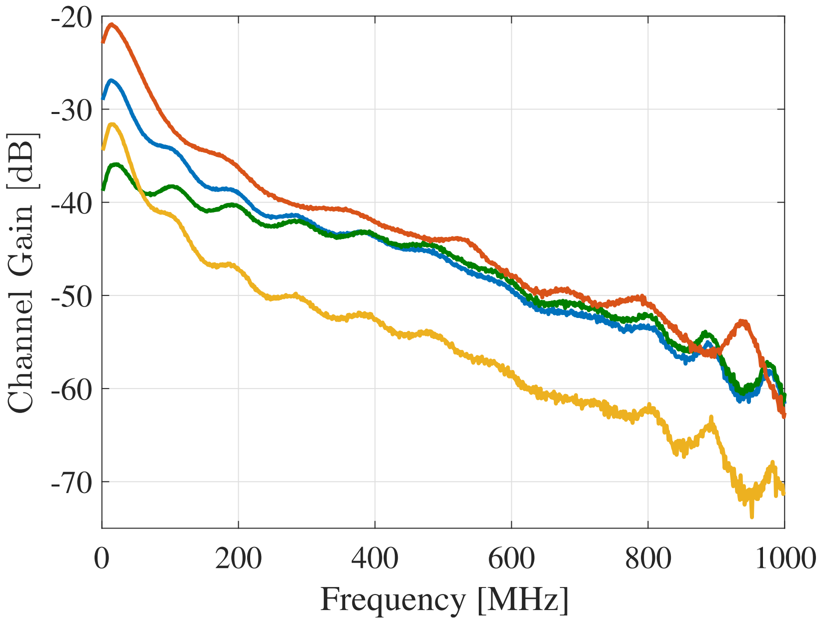

Figure 4.17: *Measured channel gains of RGBY LEDs in the optimised WDM system.*

are affected by all individual components of the communication. For instance, the frequency response and the responsivity of the PD at each wavelength affects the overall frequency response. In the presented set-up, the crosstalk between each colour is significantly attenuated by the dichroic mirrors as shown in Figure 4.1. However, the amount of the optical power reach-

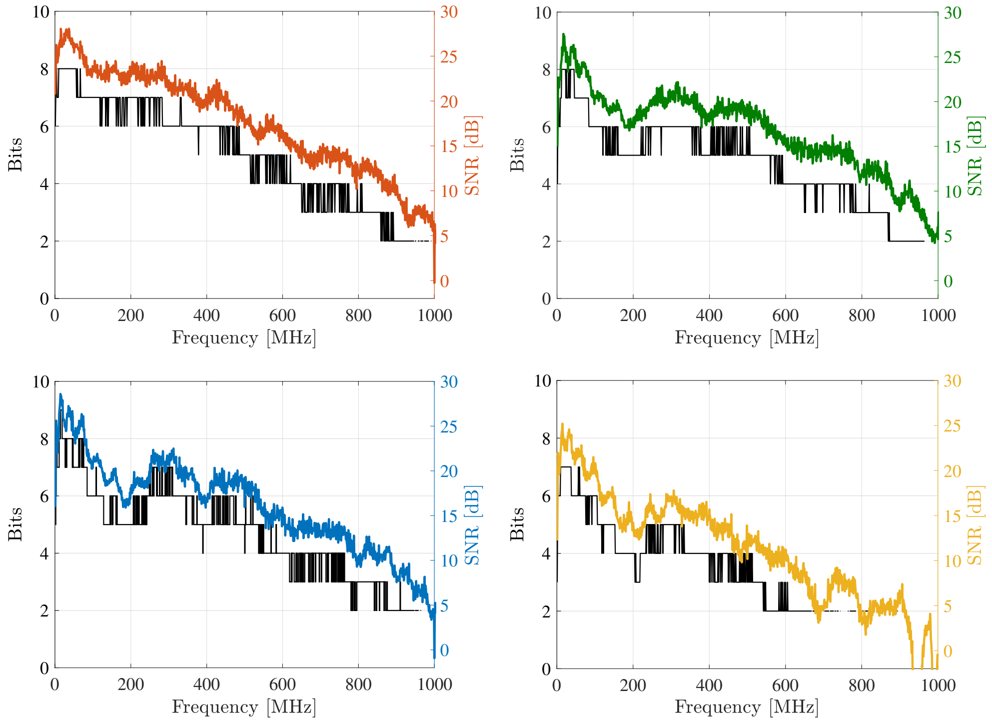

Figure 4.18: *Measured SNR and adaptively allocated bit to each subcarrier for RGBY LEDs respectively.*

ing the receiver is a determining factor for the achievable data rate. Since LEDs and dichroic mirrors are chosen from commercially available products, their spectrum is not as optimum as possible, and some part of the energy is lost at the mirrors. For instance, the mirror M1 in Figure 4.2 passes some part of the incident light from the yellow LED which does not reach the receiver. In a separate experiment with the same link distance, the achievable data rate for single colour transmission was measured. Each single LED was placed at the position of the red LED in Figure 4.2 without any mirror. The obtained data rates where 5.13 Gb/s, 5.26 Gb/s, 5.22 Gb/s and 4.15 Gb/s corresponding to the respective data rate decrease of 4%, 11%, 14%, and 30% when the full WDM system is used. If optimum mirrors were available, a potential data rate of 19.66 Gb/s could be achieved (i.e., 18.28 Gb/s after 7% HDFEC coding overhead reduction).

4.3.3 Results for using Low-cost Receivers

An ultra-high speed full WDM operation using low cost transmitters has been demonstrated. Another study on investigating how the achievable data rate scales with a low-cost receiver being used, has been carried out. Several custom-designed receiver boards have been implemented using inexpensive commercial components and a low-complexity circuit design. The design is shown in Figure 4.19. The board contains a silicon PIN diode PD (OSRAM SFH2400) followed by a transimpedance amplifier (TIA) circuit based on an operational amplifier chip (TEXAS INSTRUMENTS: LMH6629). This receiver circuit could be developed at the cost of under £5. The frequency response of the circuit has been measured and simulated using LT-Spice, and results are shown in Figure 4.20. The -3 dB bandwidth is higher than the measured results for the four LEDs shown in Figure 4.17.

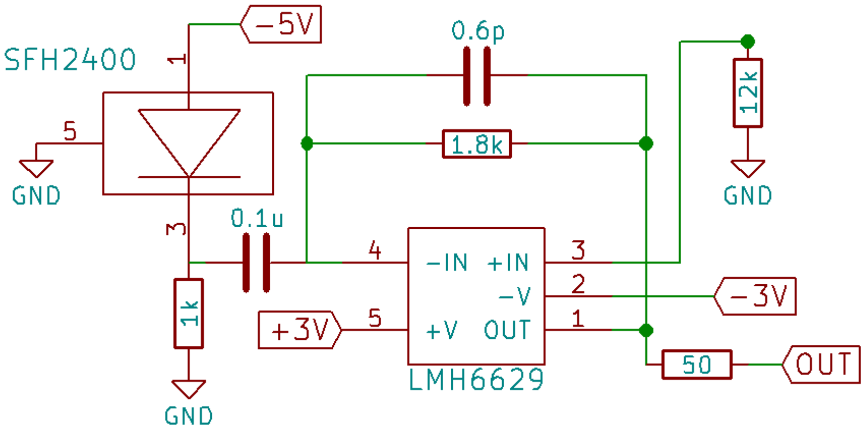

Figure 4.19: *The circuit design of the receiver board.*

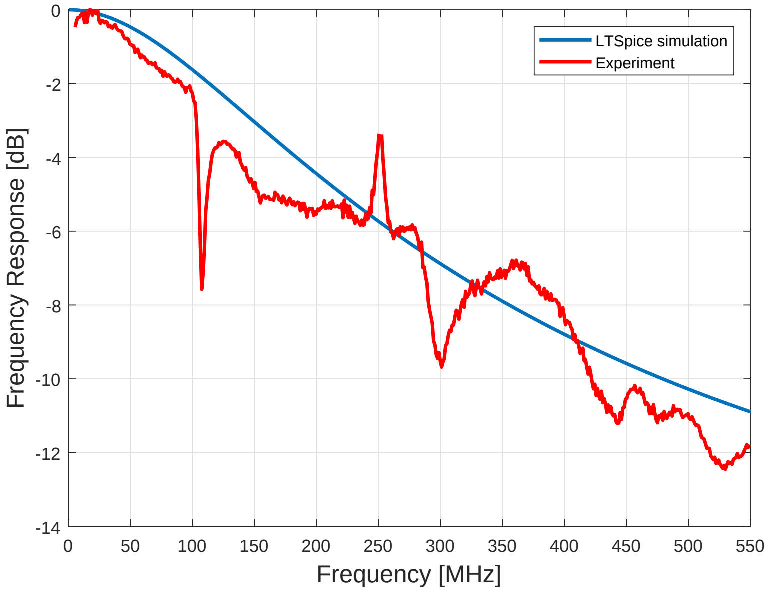

Figure 4.20: *The measured and simulated frequency response of the receiver circuit.*

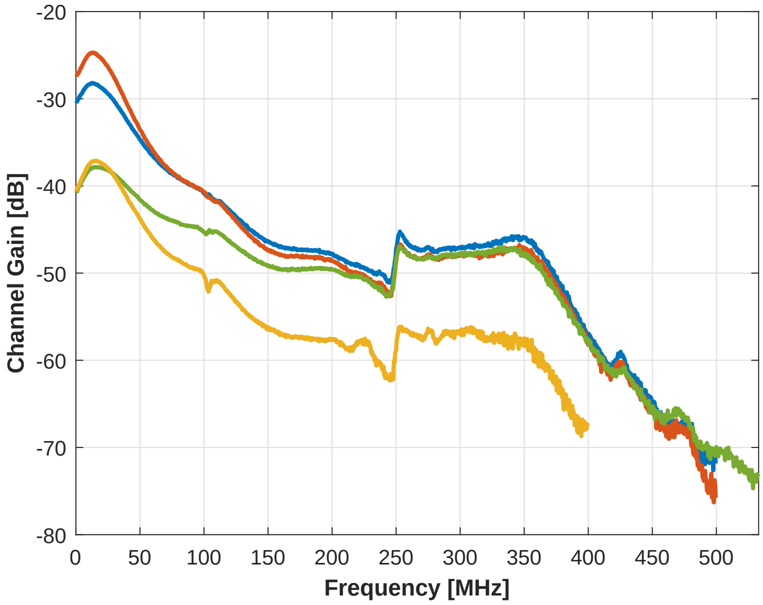

Figure 4.21: *Measured channel gains of RGBY LEDs with the low-cost receivers.*

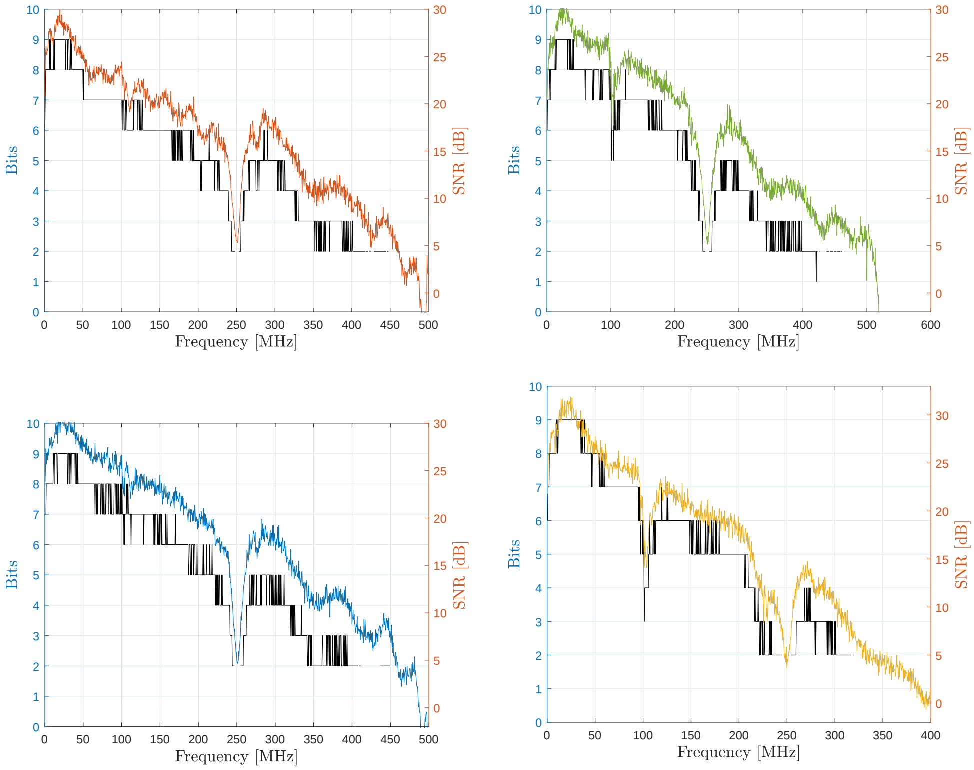

Figure 4.22: *Measured SNR and adaptively allocated bit to each subcarrier for RGBY LEDs with low-cost receivers.*

The overall frequency responses of the system for each colour are depicted in Figure 4.21. The measured SNR and bit loading results are also shown in Figure 4.22. The available modulation bandwidth has decreased to around 500 MHz for RGB LEDs and 320 MHz for the yellow LED. It can be seen from these results that a dip occurs at 250 MHz for all links. This may be caused by the on board capacitance of the receivers. Even though, with these low-complexity receiver boards, in total a data rate of 8.24 Gb/s (7.67 Gb/s after 7% HDFEC coding overhead reduction) is achieved. The measured data rates and corresponding BER are presented in Table 4.2. This investigation of inexpensive low-complexity receivers confirms the high capacity of VLC systems.

Table 4.2: *Measured results of the WDM system with low-cost receivers.*

	BER	R [Gb/s]
Red	0.0021	2.183
Green	0.0032	2.262
Blue	0.0021	2.180
Yellow	0.0033	1.618

4.4 Summary

In this Chapter, the investigation of ultra-high speed VLC system using inexpensive low-complexity front-end components has been presented. A WDM system with four low-cost commercially available LEDs (RGBY) has been implemented. Each wavelength is modulated using DCO-OFDM with adaptive bit-loading. A full WDM operation with all four colour links being active simultaneously has been demonstrated. The optimisation process for driving the LED source has been introduced and analysed with experimental results. The arrangement of dichroic mirrors has also been discussed with numerical results. A data transmission rate of 15.73 Gb/s is achieved with a BER below the 7% HDFEC limit of 3.8×10^{-3} over a 1.6 m wireless link. The effect of crosstalk has been addressed and the limitations of current set-up have been discussed. Another investigation on the achievable data rate with low-complexity receiver has been introduced. A custom-designed receiver circuit has been introduced with inexpensive commercial components and a low-complexity circuit design. A data rate of 8.24 Gb/s is reported. By investigating the inexpensive low-complexity front-end components, this work confirms that high capacity of VLC systems can be achieved with such components when suitable optimisation techniques are applied.

Chapter 5

Multiple-input Multiple-output VLC System with Simultaneously Energy Harvesting using Organic Photovoltaics

5.1 Introduction

The modern solar cell was invented in 1954 at Bell Laboratories and since then there have been three generations of development [95]. They are used to convert light energy directly into electricity by the photovoltaic (PV) effect. The current generation of solar panels have a conversion efficiency of over 40% [96]. In the early 1960s it was discovered that many dyes had semiconducting properties [97] and these dyes were used in organic materials as they exhibit PV effect [98]. The first organic photovoltaic (OPV) device was invented in the 1980s with very limited power conversion efficiency (PCE) below 0.1%. Several years later the PCE of OPV was increased to 1% by using a donor and an acceptor together in one cell [99]. Currently, the OPVs are still less efficient than most inorganic solar cells (1-11% compared to 15-40%) [96].

Typically, VLC data links use photodiodes as receivers, which require an external power supply. However, recent studies have shown the promising potential of using solar cells as optical receivers in VLC, enabling simultaneous energy harvesting and data detection [37]. These dual function optical receivers have great potential in a variety of applications in smart self-power devices, wearable optoelectronic devices and especially in future internet of things (IoT) applications. Emerging IoT technology is expected to connect 50 billion devices by 2020 [12]. The heavy deployment of an IoT wireless network using radio/microwaves will further saturate the RF spectrum and increase electromagnetic (EM) interference. Moreover, considering the huge number of objects being connected in IoT, the use of power distribution wires or batteries is complex, expensive and an environmental issue. Hence powering them by PVs is a cost and energy efficient alternative.

However, using Silicon solar panels as VLC receivers is challenging as Silicon solar cells are designed for outdoor applications while indoor light intensity levels are a factor of $\sim 10^4$ less than the 1000 W/m^2 intensity of 1-Sun standard test conditions (STC). Despite the high-power conversion efficiency of Silicon solar cells under Air Mass 1.5 Global (AM 1.5G) spectrum, the poor spectral overlap with indoor light sources such as LEDs make them quite lossy due to thermalisation and non-absorption leading to poor performance under low light intensities [100]. Compared to inorganic PVs, organic solar cells, which are constituted by the conjugated organic semiconductors, have good spectral overlap with indoor light sources. In addition, they are band-gap tunable, printable, lightweight, flexible and are amenable to roll-to-roll processing on customised and non-customised substrates, which makes them easily integrated with VLC and IoT applications.

In [37], a model of a solar panel for simultaneous energy harvesting and data communication is analysed and it reports a data rate of 11.84 Mbits/s while generating approximately 2 mW electrical power. Later a self-reverse-biased solar panel optical receiver is presented in [101] while showing an achieved data rate of 17.05 Mbits/s. Employing solar cells for indoor and outdoor light-fidelity (LiFi) applications is studied in [102]. The promising potential of OPVs in VLC has also been demonstrated in [14] with data rates up to 42 Mbits/s.

In this Chapter, the simultaneous energy harvesting and data detection properties of the OPV are investigated. Both single-input single-output (SISO) and MIMO experimental set-ups are presented. Record data rates have been achieved for both SISO and MIMO cases. A system model for OPV MIMO set-up is proposed for the first time. This model has been validated by comparing simulation results to experimental results. The scalability of the MIMO system has also been analysed numerically using the proposed methods.

5.2 Organic Photovoltaics

In this work, three types of OPV cells have been fabricated and used for the experimental implementation. Table 5.1 shows the symbols used in this Chapter and the molecular formula they represented.

The molecular structures, the schematic of the OPV device structure and an example of the actual fabricated solar cells are shown in Figure 5.1 [103]. On a single device there are eight individual solar cells (the darker area) and four common ground pads at the corners. The eight

Table 5.1: *Molecular Formula of the used OPV cells*

Symbol	Molecular Formula
Type-1	PTB7:PC$_{71}$BM
Type-2	PTB7-Th:PC$_{71}$BM
Type-3	PTB7-Th:EH-IDTBR

solar cells are not inter-connected and each of them could be used as an individual receiver.

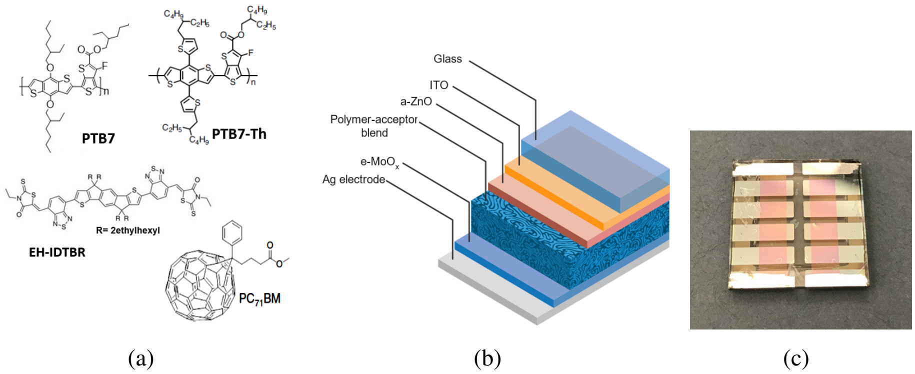

(a) (b) (c)

Figure 5.1: *(a) Molecular structures of donors and acceptor molecules; (b) Schematic of the OPV device architecture; (c) The fabricated organic photovoltaic sample including 8 individual solar cells and 4 common ground pads.*

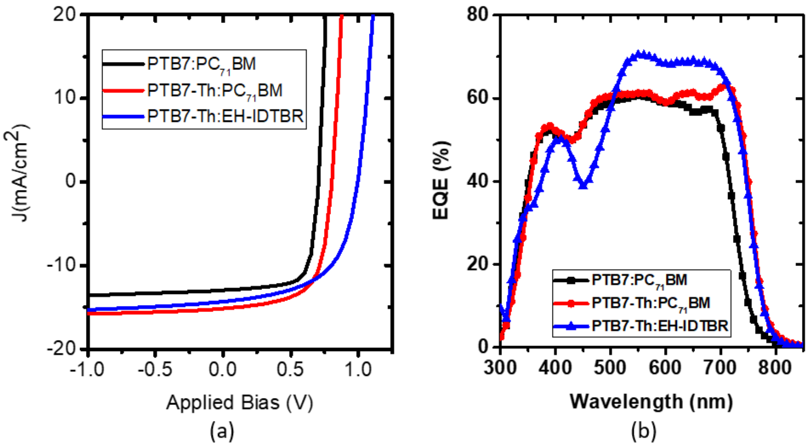

Figure 5.2: *(a) J-V characteristics of the best OPV devices used in the present study and the corresponding (b) EQE spectra.*

The power conversion efficiency of the solar cells was measured in [103] based on their J-V characteristics using 100 mW/cm^2 (AM 1.5 G) output light intensity from a solar simulator. The corresponding J-V characteristics and the photovoltaic performance parameters are listed in Figure.5.2 and Table.5.2 [103].

Table 5.2: *Solar cell performance parameters of different active layer blends based OPVs used in the present study*

Active layer	J_{sc} (mA/cm^2)	V_{oc} (V)	FF (%)	R_s $(Ohmcm^2)$	R_{sh} $(Ohmcm^2)$	PCE (avg.%)
Type-1	13.1 ± 0.20	0.708 ± 0.004	72.9 ± 0.64	0.99 ± 0.22	1477 ± 403	6.78
Type-2	14.5 ± 0.64	0.793 ± 0.009	64.9 ± 0.82	1.23 ± 0.23	899 ± 139	7.44
Type-3	14.2 ± 0.26	0.997 ± 0.004	55.3 ± 1.93	1.73 ± 0.32	576 ± 102	7.82

5.2.1 Model Analysis of Photovoltaics for Simultaneous Energy Harvesting and Communication

5.2.1.1 A Solar Panel Model for Energy Harvesting

The direct current (DC) model for a solar panel has been well studied since the 1960s [95, 104]. The equivalent circuit of the single-diode model for a solar panel is shown in Figure 5.3. In this model, a diode is connected in parallel with the photo-current source I_{PH}. I_{D} is the forward current through the diode. The leakage current in the solar panel is modelled with a shunt resistor R_{SH} while the internal voltage loss within the solar panel is modelled with a series resistor R_{S} [105]. Based on the model, the general I-V characteristic of the solar panel could be expressed as follows [105]:

$$I = I_{\mathrm{PH}} - I_{\mathrm{D}} - \frac{V + IR_{\mathrm{S}}}{R_{\mathrm{SH}}} \tag{5.1}$$

where I is the output current of the solar panel, V is the voltage across the load resistor R_{L} and $V = R_{\mathrm{L}}I$. I_{D} is given by:

$$I_{\mathrm{D}} = I_0 \exp(\frac{V + IR_{\mathrm{S}}}{n_{\mathrm{s}}V_{\mathrm{T}}} - 1) \tag{5.2}$$

where I_0 is the dark reverse saturation current of the diode, n_{s} is the number of solar cells which have been connected in series within the solar panel [106], and V_{T} is the junction thermal voltage of the diode which is given by:

$$V_{\mathrm{T}} = \frac{Ak_{\mathrm{B}}T}{q}, \tag{5.3}$$

where A is the diode quality (ideality) factor, $k_{\mathrm{B}} = 1.38^{-23}\mathrm{J/K}$ denotes the Boltzmann's constant, q is the charge of the electron and T is the temperature in Kelvin [106].

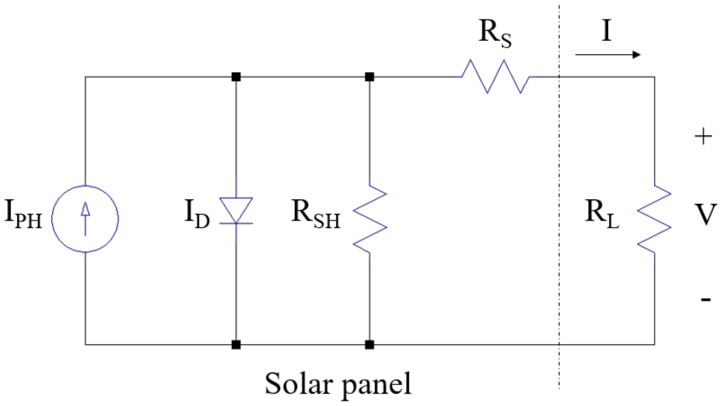

Figure 5.3: *Solar panel model for energy harvesting*

5.2.1.2 A Solar Panel Model for Simultaneous Energy Harvesting and Communication

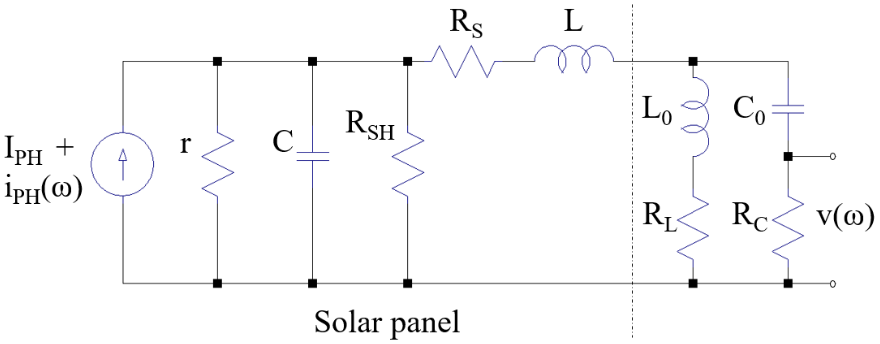

Figure 5.4: *Solar panel model for simultaneous energy harvesting and data communication*

The model of a solar panel for frequency domain characterisation is also introduced and studied [107, 108]. The circuit shown in Figure 5.4 is proposed and studied in [37] for analysing simultaneous energy harvesting and communication. The photo-current source contains both the DC component I_{PH} and the alternating current (AC) component i_{PH}. The diode in the DC model is replaced with its small single equivalent resistor r. A capacitor C is used in parallel with R_{SH} to model the internal capacitance of the solar panel. An inductor L is set in series with R_{S} to model the inductance of wire connections within the solar panel [108]. The output of the solar panel is connected to two branches: the communication branch and the energy harvesting branch. In the communication branch, a capacitor C_0 is connected to the output of the solar panel to block the DC signal and to pass the AC signal. The energy harvesting branch includes an AC signal filtering inductor L_0 and a load resistor R_{L}. The electrical power gain of the circuit can be determined as follows [37]:

$$\left|\frac{v(\omega)}{i_{\mathrm{PH}}(\omega)}\right|^2 = \left|\frac{\frac{R_{\mathrm{LC}}}{R_{\mathrm{S}}+j\omega L+R_{\mathrm{LC}}}\frac{R_{\mathrm{C}}}{\frac{1}{j\omega C_0}+R_{\mathrm{C}}}}{\frac{1}{r}+\frac{1}{\frac{1}{j\omega C}}+\frac{1}{R_{\mathrm{SH}}}+\frac{1}{R_{\mathrm{S}}+j\omega L+R_{\mathrm{LC}}}}\right|^2 \tag{5.4}$$

where $\omega = 2\pi f$ is the angular frequency, $j = \sqrt{-1}$ and R_{LC} is the equivalent resistance of the two parallel branches and is calculated as follows:

$$R_{\mathrm{LC}} = \frac{1}{\frac{1}{j\omega L_0+R_{\mathrm{L}}}+\frac{1}{\frac{1}{j\omega C_0}+R_{\mathrm{C}}}} \tag{5.5}$$

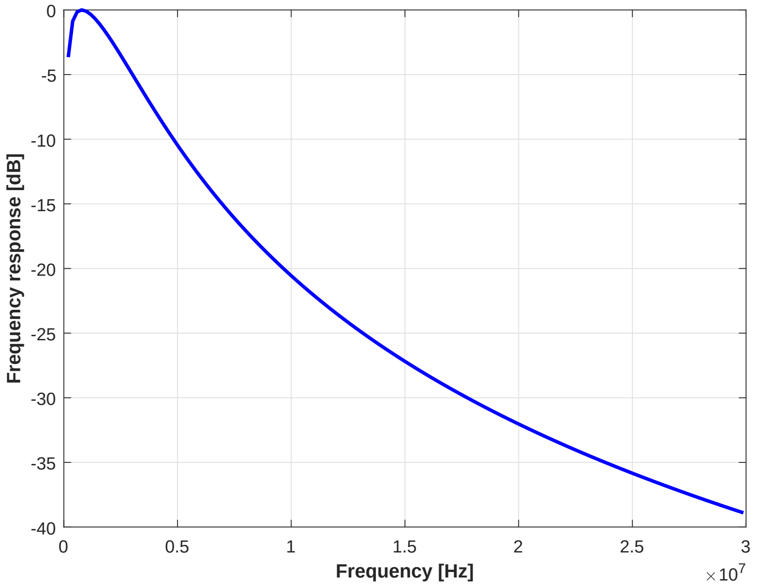

Figure 5.5: *Frequency response for single OPV cell: LTSpice simulation results compared to theory results using* (5.4).

Figure 5.5 shows the frequency response results of a single OPV cell based on (5.4). The values of the parameters are from Table 5.2.

5.3 Communication System Model

5.3.1 SISO Optical Link

In the SISO point-to-point link, the received signal can be expressed as follows:

$$S_{\mathrm{r}}(f) = S_{\mathrm{t}}(f)H_{\mathrm{t}}(f)H_{\mathrm{o}}(f)RH_{\mathrm{OPV}}(f)H_{\mathrm{AMP}}(f) + N^{\mathrm{sh}}(f) + N^{\mathrm{th}}(f), \tag{5.6}$$

where $S_{\mathrm{t}}(f)$ is the frequency component of the transmitted signal, $H_{\mathrm{t}}(f)$ the frequency response of the transmitter electrical-to-optical (E-O) gains, $H_{\mathrm{o}}(f)$ if the gain of the optical channel, R_{OPV} denotes the responsivity in A/W, $H_{\mathrm{OPV}}(f)$ is the magnitude frequency response of the LRC circuit model for OPV as shown in Figure 5.4, $H_{\mathrm{AMP}}(f)$ is the frequency response of the amplifier stages in the receiver circuit, $N^{\mathrm{sh}}(f)$ denotes the AWGN shot noise and $N^{th}(f)$ refers to the AWGN thermal noise. As lasers are used as the optical source and a line-of-sight (LoS) configuration is applied with good alignment, the gains of the transmitter and optical channel are assumed to be flat within the used modulation bandwidth in this work.

The responsivity R_{OPV} (in A/W) of the OPV for a given wavelength λ (in nm) can be appropriated as follows [22]:

$$R_{\mathrm{OPV}} = \frac{\lambda q \eta_{\mathrm{eqe}}}{hc} = \frac{\lambda \eta_{\mathrm{eqe}}}{1240}, \tag{5.7}$$

where $q = 1.602 \times 10^{-19}\mathrm{C}$ is the charge of an electron, $h = 6.626 \times 10^{-34}\mathrm{J}\cdot\mathrm{s}$ donates the Plank's constant, c refers to the speed of light and η_{eqe} refers to the external quantum efficiency (EQE).

5.3.2 MIMO System Model

Figure 5.6 illustrates a basic 2-by-2 spatial multiplexing set-up with OPVs being connected in series. The model for this MIMO transmission system is expressed as:

$$\mathbf{y} = \mathbf{G}\mathbf{H}\mathbf{x} + \mathbf{w}, \tag{5.8}$$

where **y** is the received signal vector, **G** is the electrical channel gain matrix formed by the series connection of multiple OPVs, **H** is the optical channel matrix, **x** refers to the transmitted signal vector and **w** is the AWGN vector. $\mathbf{x} = \begin{bmatrix} x_1 \cdots x_{N_{\mathrm{t}}} \end{bmatrix}^T$, with $[\cdot]^T$ being the transpose operator. $x_{n_{\mathrm{t}}}$ refers to the signal transmitted by the n_{t} transmitter. The $N_{\mathrm{r}} \times N_{\mathrm{t}}$ channel matrix

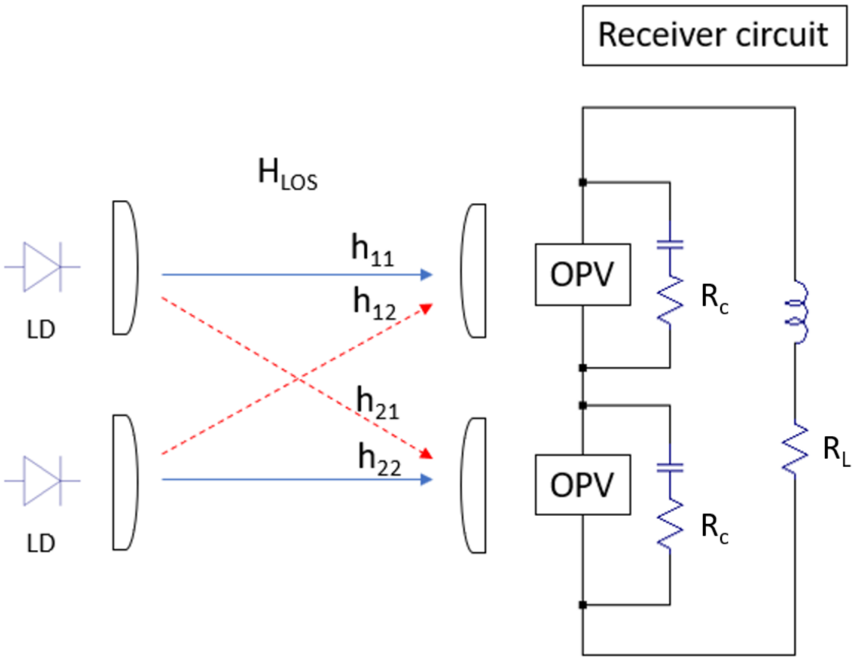

Figure 5.6: *Illustration of the 2-by-2 MIMO system with OPVs connected in series*

H is expressed as:

$$\mathbf{H} = \begin{pmatrix} h_{11} & \cdots & h_{1N_\mathrm{t}} \\ \vdots & \ddots & \vdots \\ h_{N_\mathrm{r}1} & \cdots & h_{N_\mathrm{r}N_\mathrm{t}} \end{pmatrix} \tag{5.9}$$

where $h_{n_\mathrm{r}n_\mathrm{t}}$ denotes the optical channel gains from the transmitter n_t to the receiver n_r. The optical gain of a given path can be calculated from (2.3). The $N_\mathrm{r} \times N_\mathrm{r}$ electrical gain matrix **G** is introduced by the series connection of multiple OPVs. Due to the connection, electrical crosstalk occurs between cells. **G** can be expressed as:

$$\mathbf{G} = \begin{pmatrix} g_{11} & \cdots & g_{1N_\mathrm{r}} \\ \vdots & \ddots & \vdots \\ g_{N_\mathrm{r}1} & \cdots & g_{N_\mathrm{r}N_\mathrm{r}} \end{pmatrix} \tag{5.10}$$

where g_{nm} denotes the electrical gain between the output of the n_th OPV and the photocurrent generated by the m_th OPV. That is, when $n = m$, the gain $g_{(n=m)}$ is the signal gain. And when $n \neq m$, the gain $g_{(n\neq m)}$ is the crosstalk gain.

5.3.2.1 Electrical Gains

These electrical gain values can be derived from the LRC circuit which is formed by connecting multiple circuits shown in Figure 5.4 together. Considering a set-up with N_{cell} OPV cells being connected in series, the electrical gains when $n = m$ can be expressed as:

$$g_{(n=m)} = \frac{(N_{\text{cell}}-1)R_{\text{x}} + R_{1,\text{L}}}{(N_{\text{cell}}-1)R_{\text{x}} + R_{1,\text{L}} + R_{1,\text{c}}} \times \frac{R_0}{R_{1,\text{s}} + ((N_{\text{cell}}-1)R_{\text{x}} + R_{1,\text{L}})//R_{1,\text{c}} + R_0)} \times R_{\text{c}} \tag{5.11}$$

and when $n \neq m$, the crosstalk gain can be expressed as:

$$\begin{aligned} g_{(n\neq m)} = {} & \frac{R_0 + R_{1,\text{s}}}{R_{1,\text{c}} + R_0 + R_{1,\text{s}}} \times \frac{R_{1,\text{c}}}{(N_{\text{cell}}-1)R_{\text{x}} + R_{1,\text{L}} + R_{1,\text{c}}} \\ & \times \frac{R_0}{R_{1,\text{s}} + ((N_{\text{cell}}-1)R_{\text{x}} + R_{1,\text{L}})//R_{1,\text{c}} + R_0} \times R_{\text{c}} \end{aligned} \tag{5.12}$$

where $//$ denotes connected in parallel, and:

$$R_{1,\text{L}} = R_{\text{L}} + j\omega L_0,$$

$$R_{1,\text{c}} = R_{\text{c}} + \frac{1}{j\omega C_0},$$

$$R_{1,\text{s}} = R_{\text{s}} + j\omega L,$$

$$R_0 = r//R_{\text{SH}}//\frac{1}{j\omega c},$$

and

$$R_{\text{x}} = (R_0 + R_{1,\text{s}})//R_{1,\text{c}}.$$

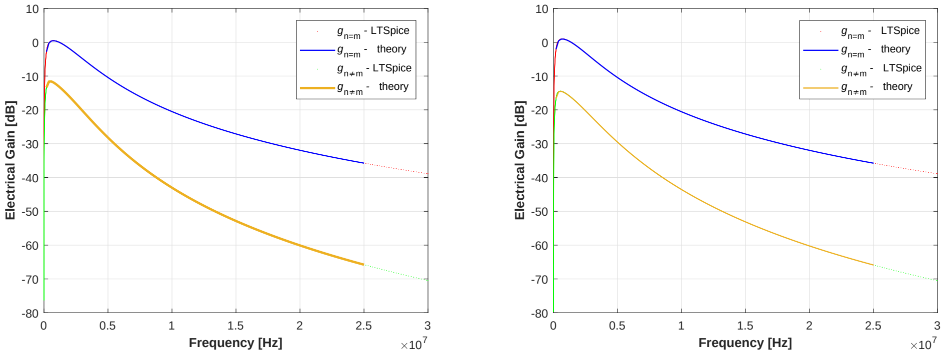

(a) (b)

Figure 5.7: *Theory and simulation results of $g_{(n=m)}$ and $g_{(n\neq m)}$ for: (a) $N_{\text{cell}} = 2$, (b) $N_{\text{cell}} = 4$.*

A circuit simulation using LTSpice has been carried out to validate (5.11) and (5.12). Both theory and simulation results are shown in Figure 5.7 for $N_{\text{cell}} = 2$ and $N_{\text{cell}} = 4$ respectively.

5.3.2.2 Noise and Crosstalk Study

In the MIMO system, while OPVs are connected, the shot noise or thermal noise generated in one cell will contribute to outputs of all the other cells with a gain. Such gains can be calculated from analysing the LRC circuits. In addition, the received signal in one cell will also contribute to the other cells with a gain, and this refers to the electrical crosstalk.

The power spectral density (PSD) of the shot noise (in A^2/Hz) can be calculated as follows [3]:

$$N_{\text{o}}^{\text{sh}} = 2qR_{\text{OPV}}(P_{\text{r,sg}} + P_{\text{r,bg}}), \tag{5.13}$$

where $P_{\text{r,sg}}$ is the signal optical power and $P_{\text{r,bg}}$ is the background optical power including the ambient light. Assuming both $P_{r,sg}$ and $P_{r,bg}$ are the same for all individual cells, the power of shot noise at one OPV output can be expressed as follows:

$$\delta_{\text{sh}}^2 = N_{\text{o}}^{\text{sh}}B\left|g_{(n=m)}\right|^2 + (N_{\text{cell}} - 1)N_{\text{o}}^{\text{sh}}B\left|g_{(n\neq m)}\right|^2. \tag{5.14}$$

The overall shot noise of one cell contain: shot noise from local cell which has a electrical power gain of $|g_{(n=m)}|^2$, and components contributed by the other $N_{\text{cell}-1}$ cells with a gain of $|g_{(n\neq m)}|^2$.

The thermal noise at each cell output also contains the noise power contributed from other cells. As shown in Figure 5.4, the thermal noise sources are: R_{SH}, R_{c}, r, R_{s} and R_{L}. The thermal noise generated by each source will contribute to the local cell with an electrical power gain of h_{self} and to the other cells with a gain of h_{else}. The method used in [37] is applied to analyse the different thermal noise contributors: an equivalent circuit can be formed by replacing the noise contributor resistor with a voltage source in series with an ideal noise-free resistor.

The PSD of thermal noise generated by R_{SH} can be calculated as follows [3]:

$$N_{\text{o,R}_{\text{SH}}}^{\text{th}} = 4k_{\text{B}}TR_{\text{SH}}. \tag{5.15}$$

The variance of thermal noise at one cell output can be calculated as follows:

$$\delta^2_{\mathrm{th,R_{SH}}} = N^{\mathrm{th}}_{\mathrm{o,R_{SH}}} B \left| h_{\mathrm{R_{SH},self}} \right|^2 + (N_{\mathrm{cell}} - 1) N^{\mathrm{th}}_{\mathrm{o,R_{SH}}} B \left| h_{\mathrm{R_{SH},else}} \right|^2 . \tag{5.16}$$

For each OPV cell, the thermal noise contributed by R_{SH} contains: the part from the local R_{SH} with an electrical power gain of $|h_{\mathrm{R_{SH},self}}|^2$ and parts from other $(N_{\mathrm{cell}} - 1)$ cells with a gain of $|h_{\mathrm{R_{SH},else}}|^2$. A noise-equivalent LRC circuit can be formed adding a voltage source in series with R_{SH} and such gains in (5.16) can be derived as follows:

$$h_{\mathrm{R_{SH},self}} = \frac{R_{\mathrm{r,c}}//(R_{\mathrm{1,s}} + R_{\mathrm{1,x}})}{R_{\mathrm{SH}} + R_{\mathrm{r,c}}//(R_{\mathrm{1,s}} + R_{\mathrm{1,x}})} \times \frac{R_{\mathrm{1,x}}}{R_{\mathrm{1,s}} + R_{\mathrm{1,x}}} \times \frac{R_{\mathrm{c}}}{R_{\mathrm{1,c}}}, \tag{5.17}$$

and

$$h_{\mathrm{R_{SH},else}} = \frac{R_{\mathrm{r,c}}//(R_{\mathrm{1,s}} + R_{\mathrm{1,x}})}{R_{\mathrm{SH}} + R_{\mathrm{r,c}}//(R_{\mathrm{1,s}} + R_{\mathrm{1,x}})} \times \frac{R_{\mathrm{1,x}}}{R_{\mathrm{1,s}} + R_{\mathrm{1,x}}} \times \frac{R_{\mathrm{x}}}{(N_{\mathrm{cell}} - 1)R_{\mathrm{x}} + R_{\mathrm{1,L}}} \times \frac{R_{\mathrm{c}}}{R_{\mathrm{1,c}}}, \tag{5.18}$$

where

$$R_{\mathrm{r,c}} = \frac{r}{1 + j\omega C},$$

and

$$R_{\mathrm{1,x}} = ((N_{\mathrm{cell}} - 1)R_{\mathrm{x}} + R_{\mathrm{1,L}})//R_{\mathrm{1,c}}.$$

Similarly, the PSD of thermal noise generated by R_c can be calculated as follows:

$$N^{\mathrm{th}}_{\mathrm{o,R_c}} = 4k_{\mathrm{B}}TR_{\mathrm{c}}. \tag{5.19}$$

The variance of thermal noise at one cell output can be calculated as follows:

$$\delta^2_{\mathrm{th,R_c}} = N^{\mathrm{th}}_{\mathrm{o,R_c}} B \left| h_{\mathrm{R_c,self}} \right|^2 + (N_{\mathrm{cell}} - 1) N^{\mathrm{th}}_{\mathrm{o,R_c}} B \left| h_{\mathrm{R_c,else}} \right|^2 . \tag{5.20}$$

The electrical gains can be derived as follows:

$$h_{\mathrm{R_c,self}} = \frac{R_{\mathrm{c}}}{R_{\mathrm{1,c+(R_0+R_{1,s})//((N_{cell}-1)R_x+R_{1,L})}}}, \tag{5.21}$$

and

$$h_{\mathrm{R_c,else}} = \frac{(R_0 + R_{1,\mathrm{s}})//((N_{\mathrm{cell}} - 1)R_{\mathrm{x}} + R_{1,\mathrm{L}})}{R_{1,\mathrm{c}+(\mathrm{R_0}+\mathrm{R_{1,s}})//((\mathrm{N_{cell}}-1)\mathrm{R_x}+\mathrm{R_{1,L}})}} \times \frac{R_{\mathrm{x}}}{(N_{\mathrm{cell}} - 1)R_{\mathrm{x}} + R_{1,\mathrm{L}}} \times \frac{R_{\mathrm{c}}}{R_{1,\mathrm{c}}}. \quad (5.22)$$

The PSD of thermal noise generated by r can be calculated as follows:

$$N_{\mathrm{o,r}}^{\mathrm{th}} = 4k_{\mathrm{B}}Tr. \quad (5.23)$$

The variance of thermal noise at one cell output can be calculated as follows:

$$\delta_{\mathrm{th,r}}^2 = N_{\mathrm{o,r}}^{\mathrm{th}}B\left|h_{\mathrm{r,self}}\right|^2 + (N_{\mathrm{cell}} - 1)N_{\mathrm{o,r}}^{\mathrm{th}}B\left|h_{\mathrm{r,else}}\right|^2. \quad (5.24)$$

The electrical gains can be derived as follows:

$$h_{\mathrm{r,self}} = \frac{R_{\mathrm{SH,c}}//(R_{1,\mathrm{s}} + R_{1,\mathrm{x}})}{r + R_{\mathrm{SH,c}}//(R_{1,\mathrm{s}} + R_{1,\mathrm{x}})} \times \frac{R_{1,\mathrm{x}}}{R_{1,\mathrm{s}} + R_{1,\mathrm{x}}} \times \frac{R_{\mathrm{c}}}{R_{1,\mathrm{c}}}, \quad (5.25)$$

and

$$h_{\mathrm{r,else}} = \frac{R_{\mathrm{SH,c}}//(R_{1,\mathrm{s}} + R_{1,\mathrm{x}})}{r + R_{\mathrm{SH,c}}//(R_{1,\mathrm{s}} + R_{1,\mathrm{x}})} \times \frac{R_{1,\mathrm{x}}}{R_{1,\mathrm{s}} + R_{1,\mathrm{x}}} \times \frac{R_{\mathrm{x}}}{(N_{\mathrm{cell}} - 1)R_{\mathrm{x}} + R_{1,\mathrm{L}}} \times \frac{R_{\mathrm{c}}}{R_{1,\mathrm{c}}}, \quad (5.26)$$

where

$$R_{\mathrm{SH,c}} = \frac{R_{\mathrm{SH}}}{1 + j\omega C}.$$

the PSD of thermal noise generated by R_s can be calculated as follows:

$$N_{\mathrm{o,R_s}}^{\mathrm{th}} = 4k_{\mathrm{B}}TR_{\mathrm{s}}. \quad (5.27)$$

The variance of thermal noise at one cell output can be calculated as follows:

$$\delta^2_{\mathrm{th,R_s}} = N^{\mathrm{th}}_{\mathrm{o,R_s}} B \left| h_{\mathrm{R_s,self}} \right|^2 + (N_{\mathrm{cell}} - 1) N^{\mathrm{th}}_{\mathrm{o,R_s}} B \left| h_{\mathrm{R_s,else}} \right|^2 . \tag{5.28}$$

The electrical gains can be derived as follows:

$$h_{\mathrm{R_s,self}} = \frac{R_{1,\mathrm{x}}}{R_0 + R_{1,\mathrm{x}} + R_{1,\mathrm{s}}} \times \frac{R_{\mathrm{c}}}{R_{1,\mathrm{c}}}, \tag{5.29}$$

and

$$h_{\mathrm{R_s,else}} = \frac{R_{1,\mathrm{x}}}{R_0 + R_{1,\mathrm{x}} + R_{1,\mathrm{s}}} \times \frac{R_{\mathrm{x}}}{(N_{\mathrm{cell}} - 1) R_{\mathrm{x}} + R_{1,\mathrm{L}}} \times \frac{R_{\mathrm{c}}}{R_{1,\mathrm{c}}}. \tag{5.30}$$

the PSD of thermal noise generated by R_L can be calculated as follows:

$$N^{\mathrm{th}}_{\mathrm{o,R_L}} = 4 k_{\mathrm{B}} T R_{\mathrm{L}}. \tag{5.31}$$

The variance of thermal noise at one cell output can be calculated as follows:

$$\delta^2_{\mathrm{th,R_L}} = N^{\mathrm{th}}_{\mathrm{o,R_L}} B \left| h_{\mathrm{R_L}} \right|^2 . \tag{5.32}$$

The resistance load in energy harvesting branch, R_{L}, generates thermal noise and contributes to each cell with a gain of $|h_{\mathrm{R_L}}|^2$ which can be calculated as follows:

$$h_{\mathrm{R_L}} = \frac{R_{\mathrm{x}}}{R_{1,\mathrm{L}} + N_{\mathrm{cell}} R_{\mathrm{x}}} \times \frac{R_{\mathrm{c}}}{R_{1,\mathrm{c}}}. \tag{5.33}$$

The variance of the overall thermal noise δ^2_{th} at one OPV cell output can be calculated as follows:

$$\delta^2_{\mathrm{th}} = \delta^2_{\mathrm{th,R_{SH}}} + \delta^2_{\mathrm{th,R_c}} + \delta^2_{\mathrm{th,r}} + \delta^2_{\mathrm{th,R_s}} + \delta^2_{\mathrm{th,R_L}}. \tag{5.34}$$

The signal crosstalk here is defined as the amount of electrical power at one OPV output contributed by other OPV cells from receiving the incident optical signal $P_{\mathrm{r,sg}}$. The power of the signal crosstalk at one OPV output can be calculated as follows:

$$P_{\mathrm{ct}} = (N_{\mathrm{cell}} - 1)P^2_{\mathrm{r,sg}}R^2_{\mathrm{OPV}}\left|g_{(n\neq m)}\right|^2. \tag{5.35}$$

Thus, the signal-to-noise ratio (SNR) γ can be estimated as:

$$\gamma = \frac{P^2_{\mathrm{r,sg}}R^2_{\mathrm{OPV}}|g_{(n=m)}|^2}{\delta^2_{\mathrm{sh}} + \delta^2_{\mathrm{th}} + P_{\mathrm{ct}}}. \tag{5.36}$$

Then the capacity for each channel can be estimated by:

$$\mathrm{Capacity} = \int_0^{\mathrm{B}} \log_2(1 + \gamma(\mathrm{f}))\mathrm{df}. \tag{5.37}$$

5.4 Experimental Set-up and Results

The basic experimental set-up is illustrated in Figure 5.8. On the transmitter side, a red laser (ThorLab, HL6544FM) with a dominant wavelength of 660 nm is used as the light source. The DC component supplied by the bench power supply (TENMA 72-10505) and the AC component generated by the Keysight 81180A Arbitrary Waveform Generator (AWG) are combined with a bias-tee (Mini-Circuit, ZFBT-4R2GW+) and sent to the LDs. The link distance is set to 40 cm and aspheric lenses are used on both the transmitter and receiver side. On the receiver end, OPVs from Figure 5.1(c) are used as the receivers and each output from the OPV cell is connected to a custom-designed receiver circuit which contains the two branches in Figure 5.4 and an amplifier circuit for the AC component within the output signal from the solar cell. The amplified AC signal is captured by an oscilloscope (Keysight, MSO7104B) and sent to the user laptop. All data processing is accomplished using Matlab.

5.4.1 Energy Harvesting Measurement

For measuring the energy harvesting performance, the LD is driven at 100 mA and measured output optical power is 56.2 mW. The optical power on the surface of the used solar cell receiver

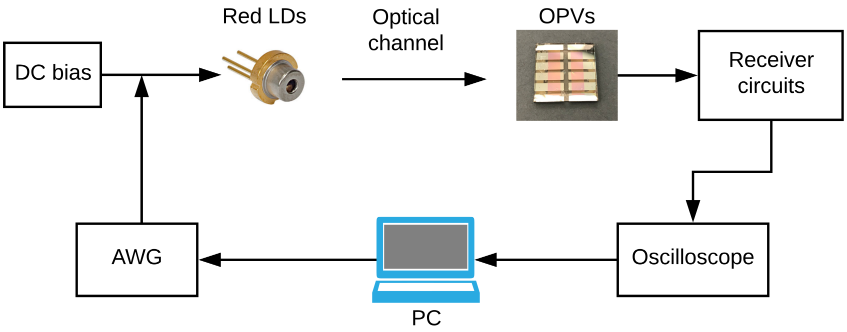

Figure 5.8: *Diagram of the OPV based VLC measurement.*

is 49.6 mW. No AC signal is sent to the LD and a variable resistor is connected to the output of the solar cell. By varying the resistance, sets of I-V data are obtained. Figure 5.9 shows the measured I-V results using 4 different pixels on the same Type-1 material blend solar cells. The estimated curves are also presented by applying the measured data (5.1) and (5.2). A least-square-error fitting method is used. There is a good match between the measured data and estimated data. It is shown that the open circuit voltage is similar for different cells while the short circuit current varies between 10 mA and 14 mA under this luminance condition. Considering the capability of energy harvesting, the P-V curve is shown in Figure 5.10 with both measured and estimated results. The result shows a similar trend for each cell but different capabilities on generating power. The maximum measured output power is 3.3 mW at a load resistance of 47 Ω.

Another measurement has also been taken using the Type-1 blends to validate the capability of energy harvesting by the MIMO set-up. The measured and fitted I-V curve is shown in Figure 5.11(a). Compared it with the I-V curve of a single cell shown in Figure 5.9, the short circuit current is similar while the open circuit voltage is approximately doubled. This is because by connecting two single solar cells in series, the voltage is added up while the current is limited with the lower value of these two cells. The corresponding P-V result is shown in Figure 5.11(b). The achieved highest generated power with the Type-1 blend is 6.8 mW.

5.4.2 Communication Results

An implementation of DCO-OFDM is used in this work to maximise the achievable spectral efficiency. A block diagram for the key elements in a DCO-OFDM communication system

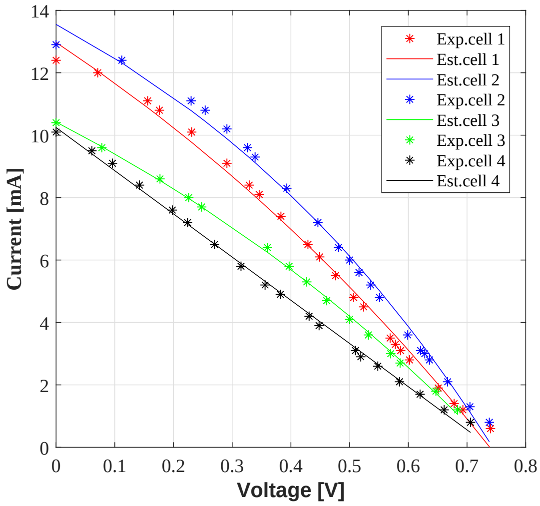

Figure 5.9: *Measured and fitted I-V curves of the solar panel under an optical power of 50 mW on the surface.*

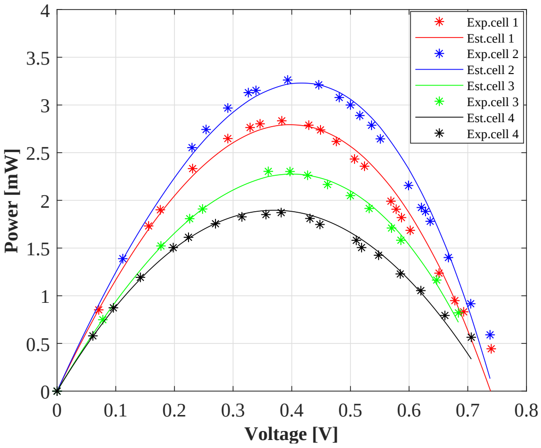

Figure 5.10: *Measured and estimated P-V curves of the solar panel under an optical power of 50 mW on the surface.*

is shown in Figure 5.12 [3]. The input bit stream is coded and mapped to M-QAM symbols. The time-domain OFDM symbols are generated after having the inverse fast Fourier transform (IFFT) operation for the M-QAM symbols. $X(k)$ is the k^{th} M-QAM symbol for a DCO-OFDM frame containing N_{FFT} subcarriers and $k = 1, 2, \cdots, \frac{N_{\text{FFT}}}{2} - 1$. As Hermitian symmetry is imposed to generate real-valued signal, there are $N_{\text{FFT}}/2 - 1$ subcarriers carrying information with index $k = 1, \cdots N_{\text{FFT}}/2 - 1$. In addition, $X(0) = X(\frac{N_{\text{FFT}}}{2}) = 0$ because of the DC bias and $X(N_{\text{FFT}} - k) = X^*(k)$ where $[\cdot]^*$ denotes the complex conjugate operation. For having a non-negative signal, a positive DC bias is added. A cyclic prefix (CP)

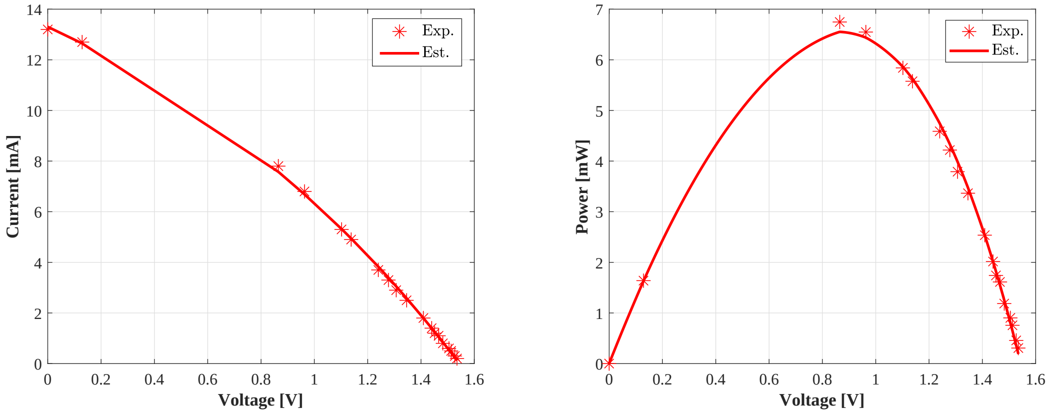

(a) (b)

Figure 5.11: *DC measurement of two solar cells in series: (a) measured and fitted I-V curve, (b) measured and estimated P-V curve.*

extension with a length of N_{CP} is added at the beginning of the OFDM symbols to mitigate the inter-symbol interference (ISI) and the inter-carrier interference (ICI) [44].

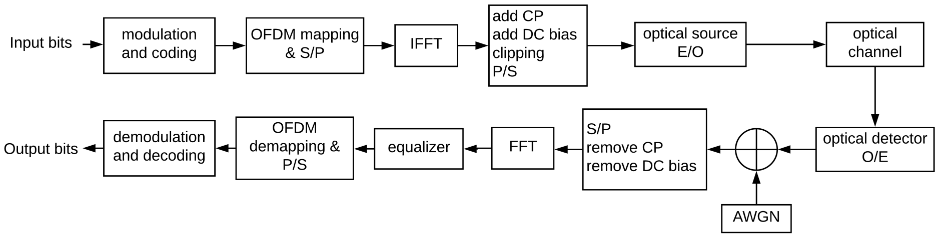

Figure 5.12: *The block diagram of the implemented DCO-OFDM based optical wireless communication system.*

An adaptive bit and power loading system has been implemented in this work. The modulation order can be selected adaptively at each subcarrier to maximise the achievable data rate at a target bit error rate (BER) [48]. The modulation order at each subcarrier M_k is determined by the available SNR and target BER. The BER of a M-QAM modulation format with SNR_k can be approximated as [49]

$$\begin{aligned} \text{BER}\left(M_k, \text{SNR}_k\right) &\simeq \frac{4\left(1-\frac{1}{\sqrt{M_k}}\right)}{\log_2 M_k} \\ &\times \sum_{l=1}^{\min(2,\sqrt{M_k})} \text{Q}\left((2l-1)\sqrt{\frac{3\text{SNR}_k}{2\left(M_k-1\right)}}\right) \end{aligned} \tag{5.38}$$

where Q(.) is the Gaussian Q-function. Therefore, using the iterative algorithm for bit loading, the modulation orders M_k are determined, and the overall data rate R is given by [50]

$$R = \frac{\sum_{k=1}^{\frac{N_{\text{FFT}}}{2}} \log_2 M_k}{(N_{\text{FFT}} + N_{\text{CP}})/2B}, \tag{5.39}$$

where B is the single-sided modulation bandwidth of the system, and N_{CP} is the cyclic prefix size.

5.4.2.1 Single-input single-output

The measured frequency responses of the whole VLC system using three different active layer blends - Type-1, Type-2, and Type-3 - are shown in Figure 5.13. Considering the -3 dB bandwidth, the Type-3 blend achieves 2.44 MHz while 1.32 MHz for Type-1 blends and 1.26 MHz for Type-2 blends are achieved. The measured signal-to-noise ratio (SNR) and the associated optimised bit loading are shown in Figure 5.14. Data rates of 90.3 Mbits/s, 78.4 Mbits/s and 102.2 Mbits/s with bit error rate of 3.6×10^{-3}, 1.6×10^{-3} and 3.1×10^{-3} have been achieved for the blends Type-1, Type-2, and Type-3 respectively.

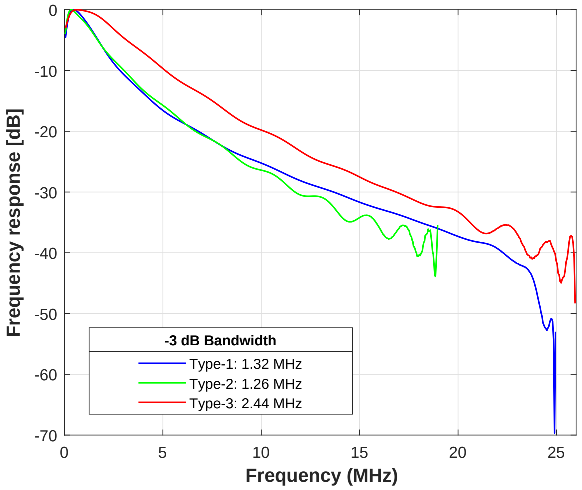

Figure 5.13: *Measured frequency response of each OPV type.*

By applying the measured parameter values for the Type-3 device in Table 5.2 to (5.4), the frequency response can be calculated and the result is shown in Figure 5.15(a). The experimental frequency response is also given and both results match. After applying the measured values to (5.13)-(5.36), the calculated SNR result is shown in Figure 5.15(b) and by using the

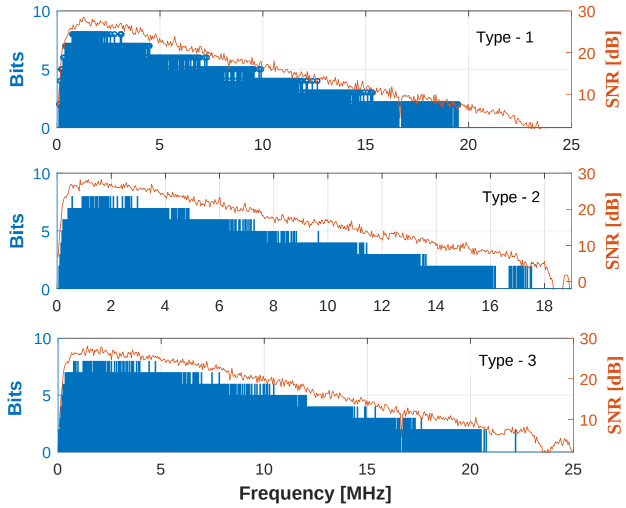

Figure 5.14: *Measured SNR and optimal bit loading of each OPV type.*

system model given previously, the simulation results are also shown. As it is a SISO set-up ($N_{\text{cell}} = 1$), all components with a gain of h_{else}, which refers to the noise or crosstalk contributed by other cells, are removed in the calculation. The experimental result is also given. Both results match in general and there are two possible reasons which cause the differences. The first reason is that the noise at the input of the oscilloscope tends to dominate the shot noise and the thermal noise components [37]. This will decrease the measured SNR in general. The other possible reason is that the applied values for the OPV parameters are the typical values from Table 5.2. The exact values of the measured cell sample can be different and this would lead to a difference between the calculated and measured results. However, the results are acceptably matched which validates the proposed calculations. It is worth mentioning that the SNR drops significantly around low frequencies. This is caused by the applied bias-tee which has a pass band of 0.1 MHz to 4200 MHz thus frequencies below 100 kHz is blocked.

Using the proposed system model and (5.39), the SISO system capacity using the Type-3 device against different R_{c} and R_{L} can be estimated. The result is shown in Figure 5.16. It is also shown that a smaller R_{c} leads to a higher capacity. In the measurement, the achieved maximum data rate 102.2 Mbits/s of Type-3 cell with R_{c} =50 Ω and R_{L} =50 Ω is slightly below the estimated value 105.8 Mbits/s.

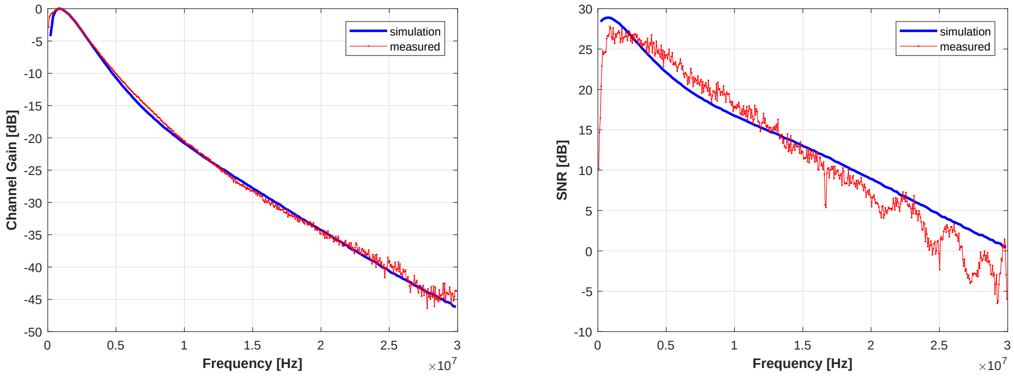

(a) (b)

Figure 5.15: *Measured SISO experimental and simulation results using Type-3 OPV cell: (a) channel gain, (b) SNR.*

5.4.2.2 Multiple-input multiple-output

The MIMO set-up is illustrated in Figure 5.17. Two red laser diodes (HL6544FM) are used with the same power supply being applied. Two OFDM data streams are sent to the two LDs individually with a peak-to-peak voltage of 1.6 V. Blends Type-1 and Type-3 have been measured for the MIMO set-up. Two cells of the same device are applied as two receivers. Two 10 nF capacitors are used in the two communication branches and a 10 μH inductor is used in the energy harvesting branch. Aspheric condenser lenses (Thorlabs ACL4532) are used on both transmitter and receiver side and in the simulation, the optical channels are treated as independent channels between each transmitter and receiver. The electrical crosstalk, as calculated in (5.35), is the main interference which comes from the series connection of multiple OPV cells.

With this 2-by-2 MIMO set-up, the maximum achieved data rates are 122 Mbits/s and 146 Mbits/s with a BER of 3.5×10^{-3} and 3.7×10^{-3} for blends Type-1 and Type-3 respectively. The frequency response and SNR results are calculated using the proposed (5.11) and (5.36) by applying the Type-3 device parameters. The result is shown in Figure 5.18 and Figure 5.19. The experimental result is also given to validate the proposed method. In Figure 5.18, $h^{\mathrm{o}}_{n_{\mathrm{r}}n_{\mathrm{t}}}$ represents the overall channel gain between the t_{th} transmitter and the r_{th} receiver which includes the optical channel gain $h_{n_{\mathrm{r}}n_{\mathrm{t}}}$, and the electrical channel gain g_{nm}. As shown in Figure 5.18, both simulated and measured h^{o}_{11} have a good match. An oscillation in the measured h^{o}_{22} is observed in the frequency region of 0.5 to 2 MHz. One possible reason causing this issue is the hardware implementation. Currently, the printed circuit board (PCB) based circuitry prototype has not been optimised in reliability against electrical oscillations. In addition, wires

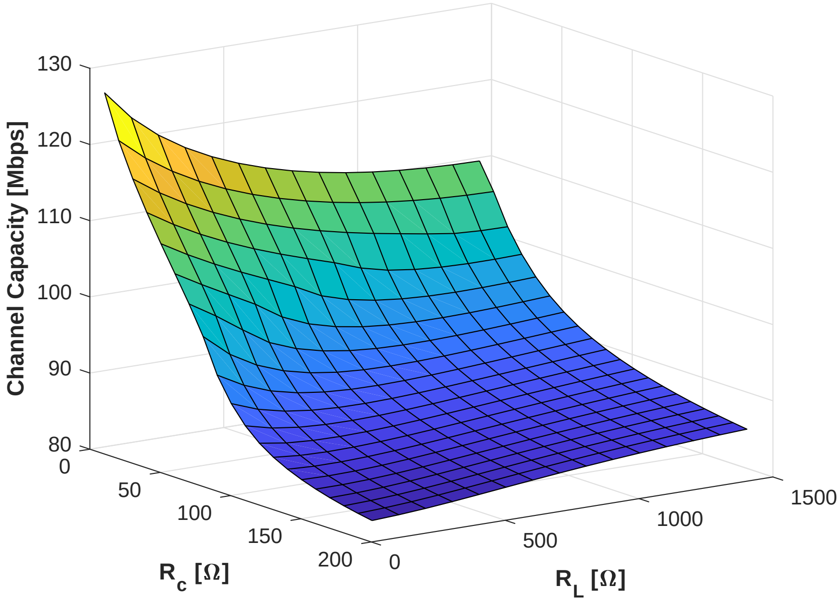

Figure 5.16: *Estimated SISO system capacity using Type-3 OPV cell with different* R_c *and* R_L*.*

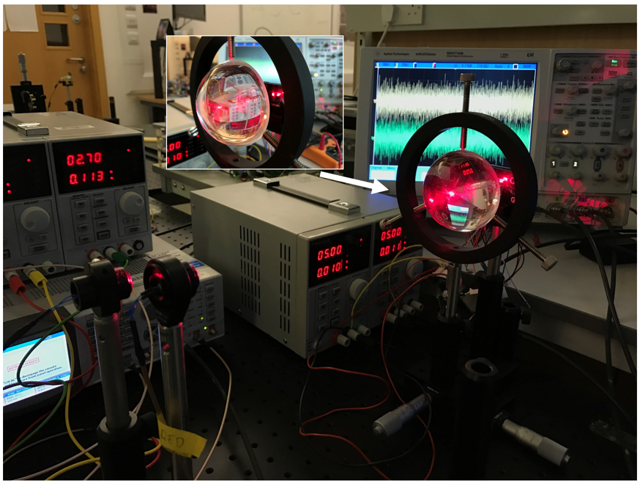

Figure 5.17: *Image of the 2-by-2 OPV MIMO set-up.*

are used to connect OPV cells and receiver board. These wires offer enough bandwidth for the measurements, however, the contacts could cause some oscillations.

Moving on, the SNR results can be obtained using (5.13)-(5.36). As shown in Figure 5.19, $\gamma_{n_\mathrm{r}n_\mathrm{t}}$ represents the SNR result of the link between the t_th transmitter and the r_th receiver. The same issue has been observed in γ_{22} where its value oscillates in the frequency region of 0.5 to 2 MHz which is possibly caused by the unoptimised hardware. Besides, the comparison

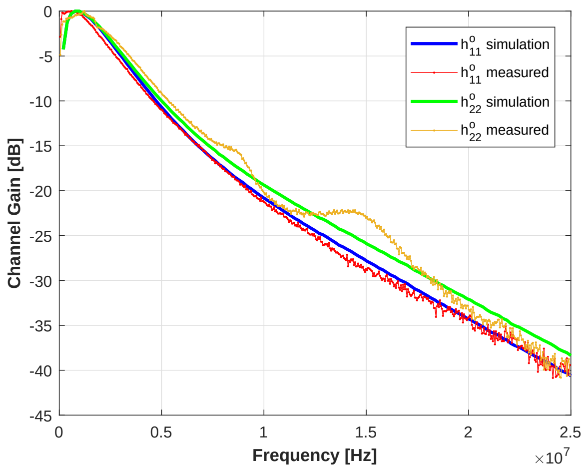

Figure 5.18: *Measured and simulation results of the MIMO channel gain using Type-3 OPV cells.*

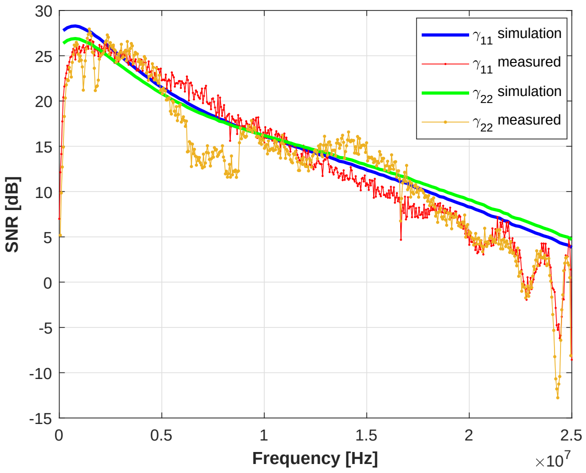

Figure 5.19: *Measured and simulation results of the MIMO SNR using Type-3 OPV cells.*

between the simulated and measured results shows similar differences as discussed in Figure 5.15(b). However, the match between both results is acceptable considering the several reasons been discussed.

As the proposed method has been validated by the 2-by-2 measurement, the system capacity with larger N_{cell} can be estimated. By increasing N_{cell}, all the following values would change: $g_{(n=m)}$, $g_{(n\neq m)}$, δ^2_{sh}, δ^2_{th} and P_{ct}. It is interesting to investigate how these values change with N_{cell}. The Type-3 device parameter is used for the following numerical analysis.

Figure 5.20 shows the electrical gains $g_{(n=m)}$ and $g_{(n\neq m)}$ with different N_{cell}. It can be seen

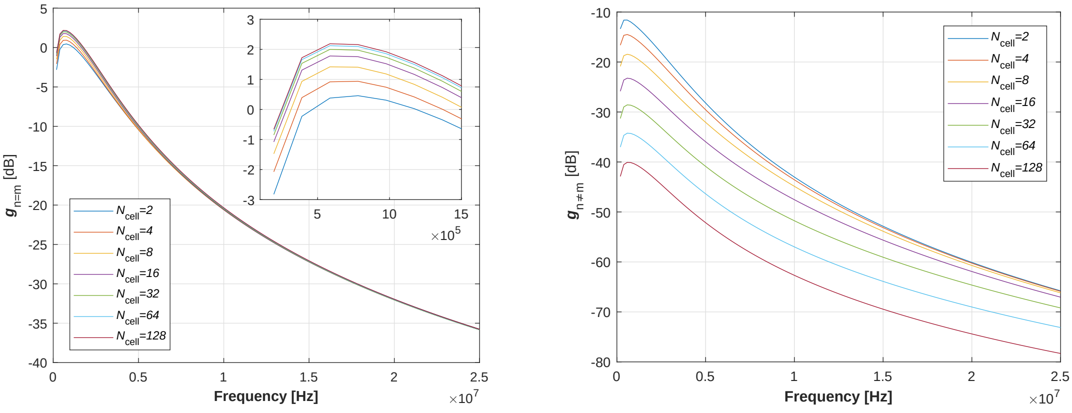

(a) (b)

Figure 5.20: *Simulation results of electrical gains against* N_{cell}*: (a)* $g_{(n=m)}$*, (b)* $g_{(n\neq m)}$*.*

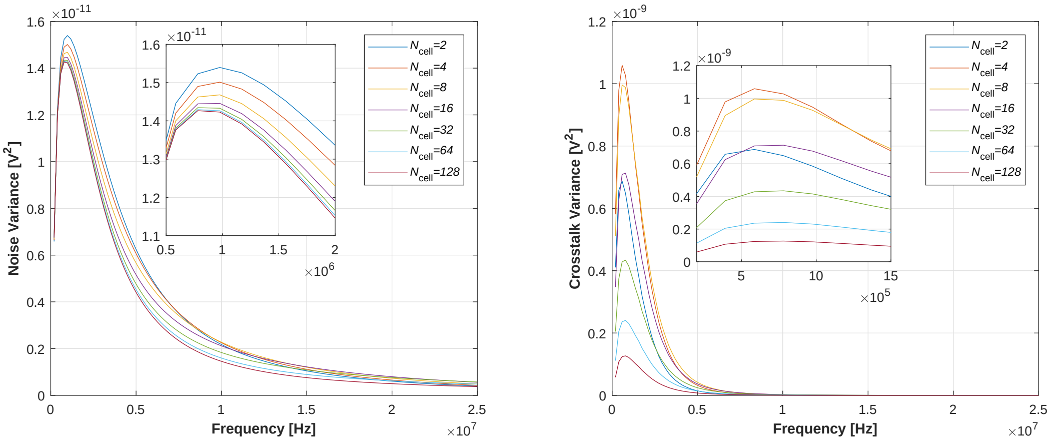

(a) (b)

Figure 5.21: *Simulation results of noise and crosstalk variances against* N_{cell}*: (a) noise, (b) crosstalk.*

that when the N_{cell} becomes larger, $g_{(n=m)}$ increases and $g_{(n\neq m)}$ decreases. In addition, $g_{(n\neq m)}$ decreases at a higher rate comparing to the change in $g_{(n=m)}$. Thus, the lower cross-channel gain leads to higher SNRs.

Figure 5.21 shows the noise power and crosstalk power with different N_{cell}. In Figure 5.21(a), it shows the noise variances decreases when the N_{cell} becomes larger. An interesting observation to make is that, as shown in Figure 5.21(b), when N_{cell} increases from 2 to 4, the crosstalk power increases. Then with larger N_{cell}, the crosstalk power decreases gradually. The N_{cell} which gives maximum crosstalk power in this case is 4 and this number may differ when using other OPV devices which have different parameter values. Finally, the capacity per channel (in

Mbits/s) can be estimated against N_{cell} and the result is shown in Figure 5.22. It is important to notice that this estimated result is based on the Type-3 OPV device with typical parameter values. As shown in Figure 5.22, the channel capacity per channel drops from 90.42 Mbits/s with $N_{\text{cell}} = 2$ to 84.45 Mbits/s with $N_{\text{cell}} = 16$. When N_{cell} increases from 16, the capacity per channel increases and saturates around 102 Mbits/s. This trend matches the changes in crosstalk power against N_{cell} as shown in Figure 5.21(b).

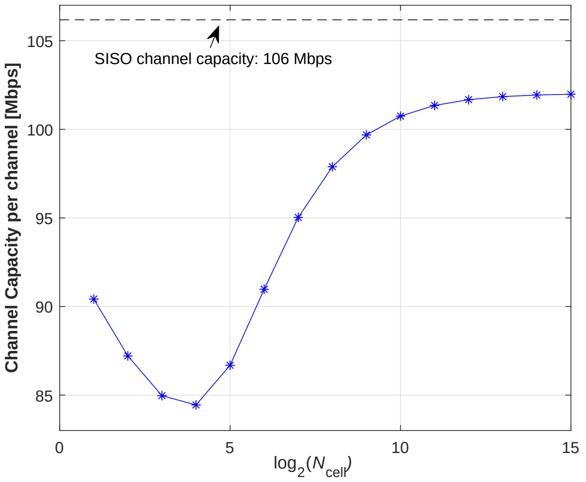

Figure 5.22: *Estimated capacity per channel against* N_{cell} *based on the Type-3 OPV cell.*

5.5 Summary

The first VLC MIMO set-up using OPVs for simultaneous energy harvesting and communication is presented. Three types of OPV cells, which are originally introduced in [103], have been used. A system model for OPV MIMO set-up is proposed for the first time. The model is validated with comparison to experimental results for both SISO and MIMO implementations. In the SISO case, the estimated frequency and SNR results show a close match to the measured results. A record data rate of 102.2 Mbits/s is achieved compared to the currently published results using OPV and this value is slightly below the estimated channel capacity of 105.8 Mbits/s by the proposed method. In the MIMO study, a 2-by-2 set-up has been implemented. The proposed system model has further been validated by comparing the estimated frequency response and SNR results to the measured ones. Limitations of current set-up are addressed. After validating the system model, more simulation results are given for investigating the scalability of the system. The electrical gains, noise power and crosstalk power have been analysed numerically with different N_{cell}. An estimated capacity per channel has been presented against applied OPV cell numbers. The crosstalk has been shown as the main factor which limits the capacity per channel. Another record data rate of 146 Mbits/s has been presented by the 2-by-2 experimental set-up.

Chapter 6

Conclusions, Limitations and Future Research

6.1 Summary and Conclusions

In this thesis, three objectives have been addressed. The first objective is to evaluate the performance of an implementation spatial modulation (SM) system and to understand the practical limitation of the system. To address this target, several generalised space shift keying (GSSK) system have been implemented. Experimental results and simulation results are given to evaluate the system performance. Current limitations have been discussed. The second objective is to investigate and develop techniques to achieve ultra-high speed data transmission using low-cost commercial front-end components. A wavelength division multiplexing (WDM) based MIMO VLC system has been implemented using low-cost off-the-shelf red, green, blue and yellow (RGBY) LEDs. A careful optimising on the system design has been performed and a record data rate is achieved. The factors which determines the achievable data rate have been discussed with experimental results being presented. The third objective is to establish a system model for MIMO VLC system using organic photovoltaics (OPVs) featuring simultaneous data communication and energy harvesting. An practical system has been implemented and the system model is proposed. Record data rates have been achieved and the system model has been validated with experimental results.

In Chapter 2, the relevant background of VLC technology has been presented. Firstly, the history of optical wireless communication (OWC) has been introduced. In addition, the dramatical growth of the LED lighting has provided a great opportunity for OWC. A typical VLC system structure has been described. Then the key elements in a VLC system have been introduced, including the VLC front-end elements, the channel and the noise sources. Some of the common digital modulation techniques in VLC have been introduced, which includes single carrier modulation and multi-carrier modulation. The M-QAM DCO-OFDM scheme has been briefly described. Finally, MIMO techniques for VLC have been presented. The concepts of repetition coding (RC), spatial multiplexing (SMP), wavelength division multiplexing (WDM) and spatial modulation (SM) have been introduced. An illustration of a 4-PAM SM system with 4 transmitters has been provided. Imaging-MIMO and non-imaging MIMO techniques are briefly introduced.

In Chapter 3, several practical implementations of GSSK have been presented. The concepts of both space shift keying (SSK) and GSSK have been introduced. A FPGA based GSSK driver has been implemented which contains a real-time GSSK encoder and can drive up to 16 optical sources at the same time. Firstly, a real-time system is presented with PIN photodiode (PD) receiver circuits, analog-to-digital convertors (ADCs) and FPGA based GSSK decoder at the receiver end. It is shown from the experimental results that one single receiver is capable of distinguishing 2 and 3 LEDs' GSSK operation with the measured BER of 1.6×10^{-5} and 2.4×10^{-4} giving the spectral efficiencies of 2 bits/symbol and 3 bits/symbol. The BER increases dramatically when the fourth LED is added. However, adding another receiver significantly improves the system performance as shown in the given results with the 3-LED and 4-LED case. The experiments also indicate that the system is flexible against receiver mobility.

In the second set-up, an array of 16 μLEDs and 4 APDs are used. An experiment is carried out showing the natural differences between the channel gain values of different links. This is the key concept of GSSK. The BER performance against received electrical SNR is presented in the cases where 2, 3 and 4 LEDs are used with a single receiver. For the demonstrated set-up, it is shown that about 5 dB higher SNR is required when one LED is added to the operation for achieving a similar BER of 1.56×10^{-5}. Results also show that the BER performance varies when receivers change their positions. It is a limitation of GSSK that the error performance is highly dependent on the dissimilarity of the channel gain values. It is shown that about 4 dB and 8 dB lower SNR is required for achieving the same BER of 10^{-3} while using two receivers compared to using a single receiver at different positions respectively. The BER versus data rate measurements of applying different spectral efficiencies on a 16 by 4 GSSK set-up indicates high spectral efficiency can be achieved. The BER results show that about 10^{-5} is achievable with the current set-up for the spectral efficiencies from 8 bits/symbol up to 16 bits/symbol.

Finally, an imaging receiver, which contains a complementary metal-oxide-semiconductor (CMOS) APD array receiver chip and an imaging lens, has been applied to the system. A 4-by-4 imaging GSSK system has been demonstrated with the spectral efficiency 4 bits/symbol. At the data rates of 200 Mbits/s, 320 Mbits/s and 400 Mbits/s, the achieved BERs are 1.56×10^{-5}, 2×10^{-4} and 1.24×10^{-2} respectively.

In Chapter 4, an investigation of the ultra-high speed VLC system with inexpensive, low-cost commercial front-end components has been carried out. A WDM system with four visible light wavelengths - red (R), green (G), blue (B) and yellow (Y) - has been implemented based on dichroic mirrors and off-white light is generated. The required optimisation for achieving high data rate has been addressed. The LED characteristic has been carefully studied. Both the crosstalk between each links and the optics placement may affect the overall achievable data rate. These factors have been considered as well. As a result, a data transmission rate of 15.73 Gb/s is achieved with the BER below the 7% HDFEC limit of 3.8×10^{-3} over a 1.6 m wireless link. To further understand how data rate changes with the system complexity, four custom-designed receiver boards with inexpensive components and low-complexity design have been used. A data rate of 8.24 Gb/s is achieved which proves that the commercially available low-cost front-end components are also capable of delivering high speed optical wireless data if all the limitation factors are addressed correctly.

In Chapter 5, the first MIMO VLC implementation using organic solar cells is presented for simultaneous wireless data communication and energy harvesting. A system model for the OPV MIMO VLC system has been proposed for the first time. This model has been validated by a set of experimental measurements on OPV cells with three different structures. Record data rates have been reported for both single-input single-output (SISO) and MIMO set-up. Based on the proposed model, the digital communication behaviour of the OPV cell can be estimated with an acceptable difference from the measured results. The model can also been used for estimating the performance with a large scale MIMO set-up.

6.2 Limitations and Future Research

In this thesis, several practical MIMO VLC system have been implemented and new record data rates have been reported. However, there are limitations. In the practical GSSK set-ups, the system benefits from the low complexity while the achieved data rate is quite limited. Currently, in order to understand the performance of GSSK system under natural channel gain, no concentrator is used. This improves the performance against receiver movement, as no precise alignment with lens is required, however, at a loss of received SNR. This will lead to a lower achieved data rate. In future research, high bandwidth components can be used. As it has been shown that high spectral efficiency can be achieved, high speed operation can be established with high bandwidth components. Considering the performance against receiver mobility, an adaptive GSSK mapping algorithm can be developed. Currently, a fixed mapping between LED combination and GSSK symbol is applied. When channel gains change with the movement, the signature of original LED combination will change and differ from the estimation symbol. With an adaptive mapping between GSSK symbols and the combination of LEDs, the encoder will keep updating based on the instant channel conditions. Thus better BER performance can be achieved with some loss in the overall throughput for re-sending the estimation symbols.

A large space and good alignment are required for the current WDM system to transmit such a high data rate. In addition, the mixture of the R, G, B, Y links are not optimised for the generation of white light illumination. In future research, more wavelengths can be added to the WDM system with suitable dichroic mirrors or optical filters being applied. Thus, the achievable data rate of the system can be further increased. However, the crosstalk may become the main factor which determine the overall data rate. Thus, a study on the crosstalk is required.

In the study of the MIMO OPV VLC system, currently the independent optical channel between each transmitter and OPV cell is assumed. This is because in the current experimental set-up, LDs are used with aspheric lenses being applied on both transmitter and receiver ends. The optical link between each LD and OPV cell is assumed to be individual and the interference and crosstalk mainly stems from the equivalent OPV circuits and the receiver circuitry. In future research, a complete system model with more realistic optical channels can be implemented. In addition, the system performance under the LED lighting conditions should also be analysed. The system model need to be modified for the indoor VLC applications where more realistic cases would be considered such as the user movement. Understanding how the OPV cells would behave when the LED light shines on part of the surface and keeps moving would be both challenging and meaningful.

Appendix A
List of Publications

This chapter contains a list of published and submitted papers.

A.1 Journal Papers

R. Bian, I. Tavakkolnia, and H. Haas, " 15.73 Gb/s Visible Light Communication with off-the-shelf LEDs", *Journal of Lightwave Technology,* vol. 37, p. 2, 2019.

R. Bian, and L. K. Jagadamma, and I. Tavakkolnia, and P. P. Manousiadis, and S. Videv, and G. A. Turnbull, and I. D. W. Samuel, and H. Haas, "Organic Photovoltaics for Simultaneous Energy Harvesting and High Speed MIMO Optical Wireless Communications", to be submitted.

A.2 Conference Papers

R. Bian, I. Tavakkolnia, and H. Haas, " 10.2 Gb/s visible light communication with off-the-shelf LEDs", *2018 ECOC.*

R. Bian, and S. Videv, and A. D. Griffiths, and J. J. D. Mckendry, and E. Xie, and K. Cameron, and E. Gu, and S. Rajbhandari, and G. Faulkner, and D. O'Brien, and M. D. Dawson, and R. Henderson, and H. Haas, "A high speed generalised space shift keying link with micro-LEDs and CMOS APD receiver", *2016 IEEE SUM,* July, 2016.

R. Bian, and S. Videv, and A. D. Griffiths, and J. J. D. Mckendry, and E. Xie, and E. Gu, and M. D. Dawson, and H. Haas, "Experimental demonstration of generalised space shift keying for visible light communication", *2017 IEEE BlackSeaCom,* Jun 2017.

Appendix B
selected publications

This chapter contains all published work.

A High Speed Generalised Space Shift Keying Link With Micro-LEDs and CMOS APD Receiver

Rui Bian[1], Stefan Videv[1], Alexander D. Griffiths[2], Jonathan J. D. McKendry[2], Enyuan Xie[2], Katherine Cameron[1], Erdan Gu[2], Sujan Rajbhandari[3], Grahame Faulkner[3], Dominic O'Brien[3], Martin D. Dawson[2], Robert Henderson[1], and Harald Haas[1]

[1]University of Edinburgh, Email:{r.bian, s.videv, k.cameron, r.henderson, h.haas}@ed.ac.uk
[2]University of Strathclyde, Email:{alex.griffiths, jonathan.mckendry, enyuan.xie, erdan.gu, m.dawson}@strath.ac.uk
[3]University of Oxford, Email:{sujan.rajbhandari, grahame.faulkner, dominic.obrien}@eng.ox.ac.uk

***Abstract*—A low complexity high speed generalised space shift keying (GSSK) visible light communication (VLC) link is investigated. A 2×2 Gallium Nitride (GaN) micro-LED array is used as transmitter and a complementary metal-oxide-semiconductor (CMOS) avalanche photo-diode (APD) array working as receiver. A bit error ratio (BER) of 2×10^{-4} up to a data rate of 320 Mbits/s is achieved which allows for error-free communication after applying forward error correction (FEC) coding. The implementation of the experiment is introduced in detail and experimental results are given.**

***Index Terms*—Visible light communication, optical modulation, space shift keying, spatial modulation, micro-LED, CMOS APD.**

I. INTRODUCTION

VISIBLE Light Communication (VLC) is a rapidly advancing optical wireless communication (OWC) technology.

A VLC system uses intensity modulation (IM) and direct detection (DD) for data modulation via visible light. Incoherent solid-state lighting elements such as light emitting diodes (LEDs) are employed as VLC transmitters. An optical link with data rates up to 3 Gbits/s with a single high bandwidth Gallium Nitride (GaN) micro-LED was demonstrated in [1]. However, such a high speed system requires a highly complex implementation.

Spatial Modulation (SM), which was first proposed in [2], is a new technique for low-complexity implementations of multiple input multiple output (MIMO) wireless systems. SM introduces additional information bits in the spatial domain thus enhancing the achieved throughput. Space Shift Keying (SSK) [3] and generalised SSK (GSSK) [4] are special cases of SM where only spatial information is sent.

This work presents a low-complexity GSSK link with micro-LEDs and an integrated complementary metal-oxide-semiconductor (CMOS) avalanche photo-diode (APD) receiver. The remainder of this paper is organized as follows: In Section II the concept of GSSK is introduced. In Section III the system set-up in detail is discussed. Results and discussions are given in Section IV. Finally, conclusions are given in Section V.

II. GENERALISED SPACE SHIFT KEYING

A SSK system consists of a transmitter array and a receiver array. As each transmitter is simply switched on and off in an on-off keying (OOK) pattern, SSK benefits from the simplicity and low cost in implementation and also is robust against LED non-linearities. SSK also increases the spectral efficiency by exploiting the spatial dimension.

Considering a SSK system with N_t transmitters and N_r receivers, each transmitter represents a unique binary index and this index is termed a spatial symbol. Data is encoded by activating one of these N_t LEDs during each symbol period. The achieved spectral efficiency is $\log_2(N_t)$ bits per symbol (bps). In GSSK, the limitation of activating only one LED is removed and in the N_t GSSK system the maximum spectral efficiency is N_t bps.

In a 4 GSSK system the maximum likelihood decoder takes signatures from the estimation signal and generates a 4×1 vector for each spatial symbol during the particular symbol period. This means that a 4×16 matrix is established for all of the 16 symbols. The decoder compares the received signal $\mathbf{x}$ to each signature value $\mathbf{s}^y$ for the symbol y. The Euclidean distance of the received signal and the signature is calculated as:

$$\mathrm{d} = \sqrt{\sum_{i=1}^{N_r} (\mathbf{x}_i - \mathbf{s}_i^y)^2} \tag{1}$$

The spatial symbol which has the minimum distance from the received signal is chosen to be the transmitted one.

III. SYSTEM SET-UP

At the transmitter side, a Nexys3 board, which features the Xilinx Spartan-6 LX16 field programmable gate array (FPGA), is employed to generate random signals and then encode them into GSSK symbols. This board drives the 4 blue GaN micro-LEDs directly, individually and digitally. The micro-LEDs are attached to a daughterboard with 1 cm distance between each. Each micro-LED has a plastic aspheric lens to collimate the light and this reduces the semi-angle to 4 degrees.

At the receiver end, an integrated CMOS APD array is used. There are 49 individual APDs on the CMOS chip of which

978-1-5090-1900-7/16/$31.00 ©2016 IEEE

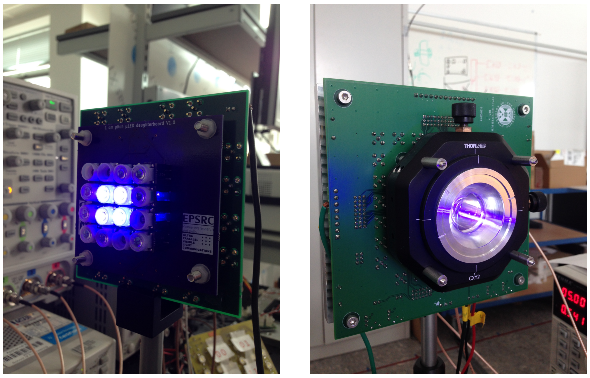

(a) Transmitter (b) Receiver

Fig. 1: System set-up

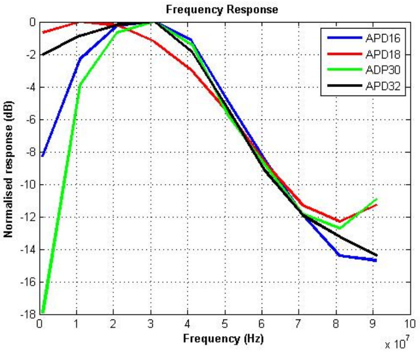

Fig. 2: Frequency response

4 in the middle are chosen (numbered 16, 18, 30, 32). An imaging lens is equipped to focus the light beams onto the APD array. The link distance is 40 cm.

IV. Results and Discussion

The frequency response of each chosen APD and the signal-to-noise ratio (SNR) of the established channels are measured and results are shown in Fig. 2 and Fig. 3. The average -3 dB bandwidth of the 4 APDs is around 45 MHz. The SNR condition of each channel differs because of the alignment between transmitters and receivers. The results show that APD No.18 and No.32 are not aligned perfectly thus the received optical power is less compared with the other two.

With these channel conditions, the bit error ratio (BER) performance is studied at different switching frequencies and the results are given in Fig. 4. At a switching frequency of 50 MHz, the achieved data rate is 200 Mbits/s with a BER of 1.56×10^{-5}. When the switching frequency increases to 80 MHz giving a data rate of 320 Mbits/s, the BER increases to 2×10^{-4} which is still usable for error-free communication after applying forward error correction (FEC) coding. At a 100 MHz switching rate where it gives 400 Mbits/s, a BER of 1.24×10^{-2} is achieved. However with better channel conditions by having better alignment, the BER performance can be improved.

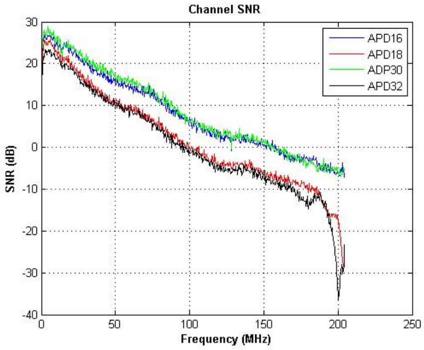

Fig. 3: Channel SNR

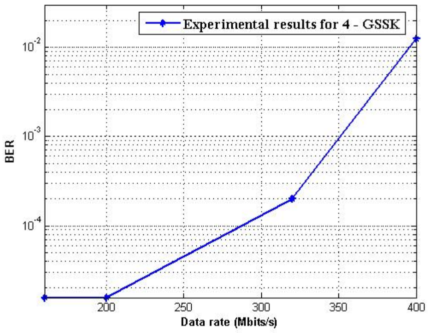

Fig. 4: BER vs Data rate

V. Conclusions

A low-complexity high speed GSSK VLC link with a 2×2 blue micro-LED array and an integrated CMOS APD array receiver is presented. The BER results are shown for data rate up to 400 MBits/s . In future research, an increase in the spectral efficiency, thus the data rate, with larger scale of transmitters and with the low-complexity implementation of GSSK will be considered.

Acknowledgment

This research was supported by the UK Engineering and Physical Sciences Research Council under Grant EP/K00042X/1.

References

[1] D. Tsonev, H. Chun, S. Rajbhandari, J. McKendry, S. Videv, E. Gu, M. Haji, S. Watson, A. Kelly, G. Faulkner, M. Dawson, H. Haas, and D. O'Brien, "A 3-Gb/s Single-LED OFDM-Based Wireless VLC Link Using a Gallium Nitride μLED," *IEEE Photon. Technol. Lett.*, vol. 26, no. 7, pp. 637–640, Apr. 2014.

[2] R. Mesleh, H. Haas, C. W. Ahn, and S. Yun, "Spatial Modulation – A New Low Complexity Spectral Efficiency Enhancing Technique," in *IEEE International Conference on Communication and Networking in China (CHINACOM)*, Beijing, China, Oct. 25–27, 2006, pp. 1–5.

[3] J. Jeganathan, A. Ghrayeb, L. Szczecinski, and A. Ceron, "Space Shift Keying Modulation for MIMO Channels," *IEEE Trans. on Wireless Commun.*, vol. 8, no. 7, pp. 3692–3703, Jul. 2009.

[4] J. Jeganathan, A. Ghrayeb, and L. Szczecinski, "Generalized Space Shift Keying Modulation for MIMO Channels," in *Proc. IEEE 19th Intern. Symp. on Personal, Indoor and Mobile Radio Commun. PIMRC 2008*, Cannes, France, 15–18 Sep. 2008, pp. 1–5.

Experimental Demonstration of Generalised Space Shift Keying for Visible Light Communication

Rui Bian[1], Stefan Videv[1], Alexander D. Griffiths[2], Jonathan J. D. McKendry[2], Enyuan Xie[2], Erdan Gu[2], Martin D. Dawson[2], and Harald Haas[1]

[1]University of Edinburgh, Email:{r.bian, s.videv, h.haas}@ed.ac.uk
[2]University of Strathclyde, Email:{alex.griffiths, jonathan.mckendry, enyuan.xie, erdan.gu, m.dawson}@strath.ac.uk

***Abstract*—A low complexity generalised space shift keying (GSSK) experimental set-up for visible light communication (VLC) is demonstrated. The GSSK encoder is implemented in a field programmable gate array (FPGA) board. No digital-to-analog converter (DAC) is required and up to 16 output channels are supported which greatly exceeds that of an arbitrary waveform generator (AWG). A 4×4 Gallium Nitride (GaN) micro-LED array is used as transmitter while 4 avalanche photo diode (APD) receiver boards are acting as receivers. GSSK exploits the natural differences between the multiple communication links. The bit error ratio (BER) performances are evaluated for different transmitter and receiver arrangements. It is also shown that how different receiver positions and increasing receiver number will affect the BER performance. The bit error performance greatly depends on the dissimilarity of the channel gains. A spectral efficiency of 16 bits/symbol is achieved by using all 16 micro-LEDs and 4 receivers. The implementation of the experiment is introduced in detail and experimental results are given.**

***Index Terms*—Visible light communication, optical modulation, space shift keying, spatial modulation, micro-LED, FPGA.**

I. INTRODUCTION

LIGHT emitting diodes (LEDs) are widely used for illumination and in recent years they have been given a new use - transmitting high speed wireless data. This is referred to as visible light communication (VLC). VLC has now become a rapidly advancing technology for optical wireless communication (OWC). VLC complements Radio Frequency (RF) technology and offers advantages in terms of capacity, efficiency, safety and security.

In VLC, visible light is the carrier of information and it is restricted to intensity modulation (IM) and direct detection (DD). Incoherent solid-state lighting elements such as LEDs are widely employed as VLC transmitters. The off-the-shelf commercial LEDs are designed for lighting and their -3 dB bandwidth are typically 2-3 MHz [1]. To achieve a higher communication data rate, great effort is directed towards developing higher bandwidth LEDs. The work in [2] introduced a Gallium Nitride (GaN) LED with diameter of 50 μm. With single micro-LED, an optical link with data rates up to 3 Gbits/s was demonstrated in [3]. As a trade-off, such high speed link requires a highly complex digital modulation scheme.

A wide range of modulation techniques have been proposed for VLC. Turning the LED on and off to represent binary information is known as on-off-keying (OOK). It offers low spectral efficiency but benefits from low complexity in implementation and is robust against LED non-linearity. Pulse amplitude modulation (PAM) and optical orthogonal frequency division multiplexing (OFDM) are also studied and compared in [4], [5] and [6]. Optical-OFDM offers high spectral efficiency but suffers from the LED non-linearity [7]. Solutions including predistortion are presented to counter the effect of LED non-linearity, but these measures require additional computational complexity. Multiple input multiple output (MIMO) techniques which offer high data rates by increasing the spectral efficiency are also studied for VLC [8]. In a typical MIMO system, all the transmitters are active during transmission and this causes inter-channel interference which should be mitigated at the cost of additional computational complexity.

Spatial modulation (SM), introduced in [9] and further enhanced in [10] and [11], describes a new low-complexity implementation for MIMO wireless systems. In SM, some information bits are conveyed in the additional spatial dimension which is the physical position of each transmitter. During each symbol transmission, only one transmitter is active so that inter-channel interference is avoided. In addition, the number of receivers can be smaller than the number of transmitters. SM is also studied for VLC in [12, 13] and is combined with OFDM to achieve high spectral efficiency. Space Shift Keying (SSK) [14] and generalised SSK (GSSK) [15] are special cases of SM where only spatial information is sent and each individual transmitter operates in OOK mode. SSK and GSSK have all been expanded to optical communication [16, 17]. Compared with OOK, SSK and GSSK inherit the robustness against LED non-linearity, meanwhile offer higher spectral efficiency by exploiting the spatial dimension for information transmission. Compared with PAM and direct current biased optical OFDM (DCO-OFDM), SSK and GSSK require much lower complexity in implementation and digital-to-analog converters (DACs) are not required which significantly reduce the complexity and the cost.

Both SSK and GSSK are well studied for optical communication [16–18] but there are little experimental results. Work in [19] and [20] present both SSK and GSSK using the digital camera as receiver. Image sensor receivers have

978-1-5090-5049-9/17/$31.00 ©2017 IEEE

several advantages against photo diodes (PDs) as the LED sources are well separated on the image because there are a large number of pixels which can detect the LED lights. Thus a higher order operation can be achieved easily by using more LEDs and the lights are prevented from being mixed by a high resolution camera receiver. However the data rate is limited by the camera's frame rate - up to 1000 frames per second as reported. The work in [21] shows an experimental set-up with 2 LEDs and 1 PD receiver and states that the experimental modulation order is limited by the Arbitrary Waveform Generator (AWG) which contains only two output ports.

This work presents a low-complexity GSSK experimental set-up with a FPGA based GSSK encoder while employing a 4 by 4 micro-LED array as transmitter and 4 avalanche photo-diode (APD) receiver boards. Up to 16 micro-LEDs can be activated for a high order GSSK operation. The bit error performances for different experimental set-up are evaluated.

The remainder of this paper is organised as follows: In Section II the concept of GSSK is introduced. In Section III the system set-up in detail is discussed. Results and discussions are given in Section IV. Finally, conclusions are presented in Section V.

II. GENERALISED SPACE SHIFT KEYING

A SSK system consists of a transmitter array and a receiver array. Considering a LED array with N_t LEDs, each LED has a unique spatial position and it can be represented by a unique binary index. In SSK operation, only one of the LEDs is active during each symbol duration. A maximum likelihood (ML) decoder is implemented on the receiver end to determine which LED was turned on based on the natural differences of channel gains between each LED and the receivers. Once the activated LED is found, its binary index is decoded as the transmitted data which is in $\log_2(N_t)$ bits. Thus a SSK operation with N_t LEDs offers a spectral efficiency of $\log_2(N_t)$ bits per symbol.

This operation can be generalised using GSSK by removing the limitation of turning on only one LED during each symbol duration. For a LED array of N_t LEDs, there are 2^{N_t} combinations of modulating LEDs including turning off all the LEDs. Thus in the N_t GSSK system the maximum spectral efficiency is N_t bits per symbol.

During a symbol clock T, a duty cycle τ can be introduced to control how long the LED will be on during each symbol duration. A non-return-to-zero (NRZ) pulse pattern is formed when $\tau = 1$ and each LED is on for the whole symbol duration. Using a NRZ pulse pattern offers the maximum spectral efficiency of N_t bits per symbol. When $\tau < 1$ each LED is turned on for part of each symbol duration and then turned off and the signal is in the return-to-zero (RZ) pulse pattern. The RZ pattern has better performance against signal's baseline drifting and it is helpful for synchronisation purposes. Varying the duty cycle will also make the LEDs work in dimmed conditions which supports the IEEE 802.15.7 standard [22]. An example GSSK scheme for two LEDs when $\tau = 1$ is shown in Fig. 1.

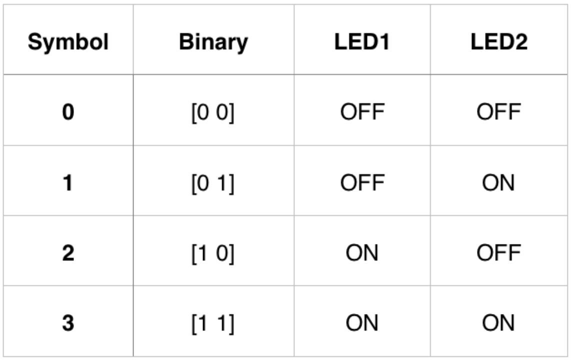

Symbol	Binary	LED1	LED2
0	[0 0]	OFF	OFF
1	[0 1]	OFF	ON
2	[1 0]	ON	OFF
3	[1 1]	ON	ON

Fig. 1: Example of GSSK scheme for two LEDs

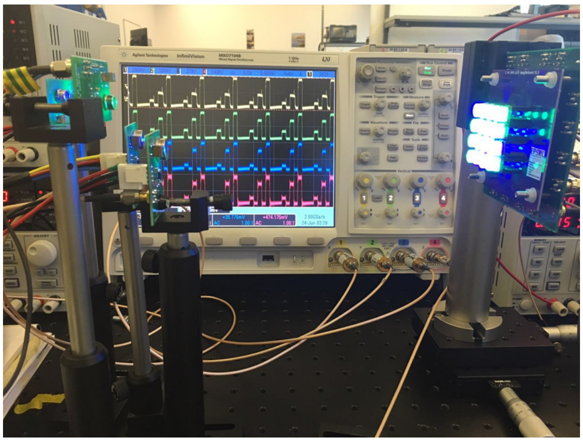

Fig. 2: Experimental Set-up

TABLE I

Receiver Position	Receiver coordinate (cm)
1	(35, 0.5, 20.5)
2	(35, 2.5, 20.5)
3	(37, 0.5, 22.5)
4	(37, 0.5, 22.5)
5	(35, 0.5, 21.5)

III. THE EXPERIMENTAL SET-UP AND DESCRIPTION

The experimental set-up is shown in Fig. 2. At the transmitter side, a GSSK encoder is implemented with a Nexys3 board, which features the Xilinx Spartan-6 LX16 field programmable gate array (FPGA). The 16 micro-LEDs are plugged into a daughterboard with 1 cm distance between each other forming a 4 by 4 array. The daughterboard is attached to a motherboard which connects to DC power supply and 16 individual output ports of the FPGA. Each micro-LED has a plastic aspheric lens to collimate the light and this reduces the semi-angle to 4 degrees. The 16 micro-LEDs are numbered from 1 to 16 starting from the top left corner one to the lower right corner one. At the receiver end, up to 4 individual APD receiver boards are available and no lens is used on the receiver side in this work. The receivers are set to different positions regarding different experiments and the coordinates of these positions

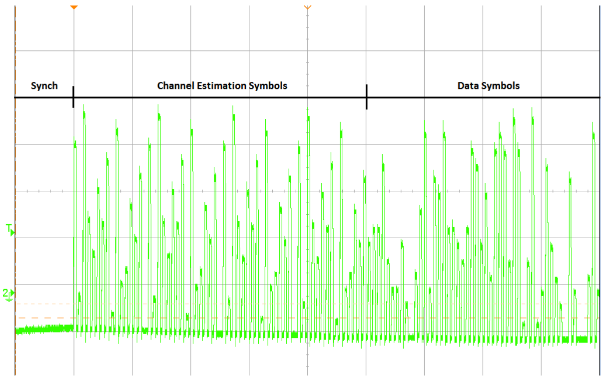

Fig. 3: Captured signal when $\tau = 0.5$

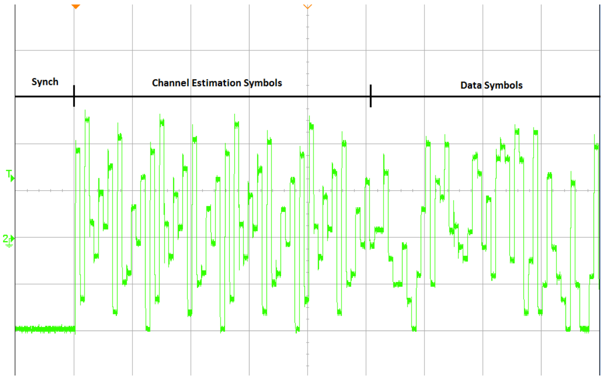

Fig. 4: Captured signal when $\tau = 1$

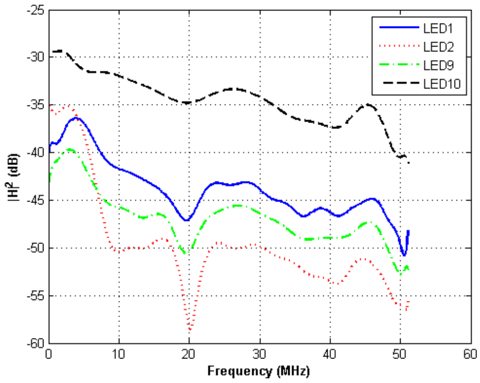

Fig. 5: Channel Gain: receiver position 1

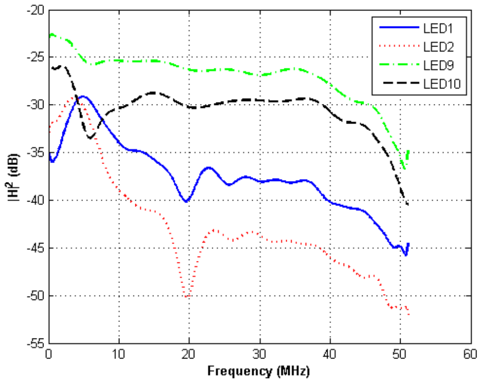

Fig. 6: Channel Gain: receiver position 2

are given in Table I. The link distance is 35 cm or 37 cm depending on the receiver positions.

The data packets for measurements are generated by the FPGA and contain three parts: the synchronisation symbols, channel estimation symbols and data symbols. The synchronisation symbols are used to trigger the signal. In the channel estimation part, all the possible combinations of LEDs are activated sequentially and this entire sequence is sent repeatedly for 4 cycles. The purpose of this is to train the ML decoder by capturing the power level for each known GSSK symbol. After the estimation symbols, 6.4×10^4 bits of data are encoded and sent. In the designed FPGA encoder, varying the duty cycle τ is supported which shows that the encoder is a potential candidate for VLC application where dimmed control is required. Fig. 3 and Fig. 4 show the sample captured signals when $\tau = 0.5$ and $\tau = 1$ respectively.

There are four sets of measurements. The first experiment measures the channel gain between 4 selected LEDs and 2 receivers at different positions. The result shows how each channel gain differs from the others. The second is measuring the bit error ratio (BER) performance when using a single receiver and multiple transmitters. The third experiment shows how the BER performance behaves when setting the receiver at different positions and using more receivers. The last experiment employs the entire 16 LEDs and 4 receivers measuring the BER performance against the achieved data rate while running at different spectral efficiencies. The switching frequency for each LED is set to 5 MHz where 5M symbols are sent per second.

IV. RESULTS AND DISCUSSION

The experiments evaluate the channel gains and BER performances at different spectral efficiencies. Four micro-LEDs are chosen from the array for the first three experiments. The LED numbers and their coordinates are given as: LED1 (0, 0, 23), LED2 (0, 1, 23), LED9 (0, 0, 21) and LED10 (0, 1, 21). As the direction of each LED is irregular when being plugged into the daughterboard, all the four LEDs are tilted towards position 5 resulting in forming an overlapping covering area.

In the first experiment, the APD receiver is set at position 1 and then the channel gains between each of the four LED and the receiver are measured. The result in Fig. 5 shows the natural differences of channel gains between each LED and the same receiver. These differences are exploited at the receiver to estimate which symbol has been transmitted. The measurement is then repeated by setting the receiver to position 2 and the result is shown in Fig. 6. By comparing the two figures it is clear that the channel gain also differs between links from one LED to receivers at different positions. This is a key feature exploited by GSSK. If receiver mobility is to be supported, the system needs to periodically send training information in order to be able to decode information correctly.

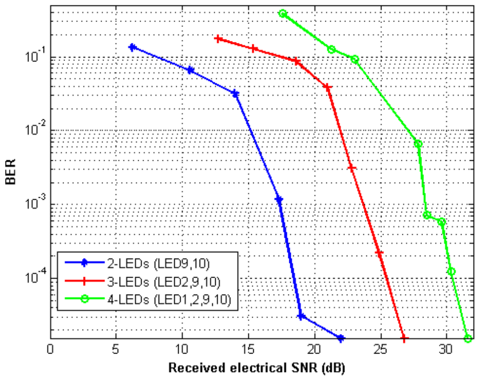

Fig. 7: BER vs received electrical SNR

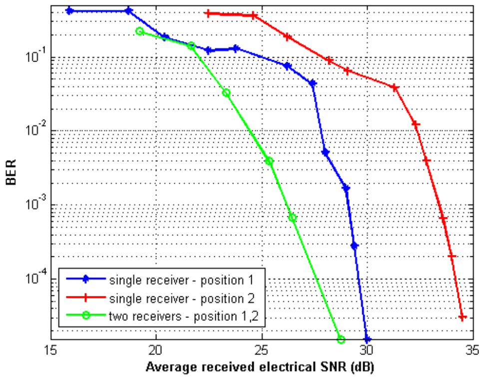

Fig. 8: BER vs received electrical SNR

In the second experiment, the error performance is evaluated when using one single receiver and multiple transmitters. Fig. 7 shows the BER performance against the received electrical signal-to-noise ratio (SNR) when using 2, 3 and 4 transmitters which results in a spectral efficiency of 2 bits/symbol, 3 bits/symbol and 4 bits/symbol respectively. The channel gain for LED1, LED2, LED9, LED10 are measured and then normalised giving [0.14, 0.244, 0.477, 1] respectively. The received signal for each case is similar to PAM signals at the same spectral efficiency. However the received power levels are not equally spaced. When the modulation order is increased, there are more GSSK symbols that need to be distinguished. The results show that when one more LED is used, about 5 dB higher SNR is required for achieving the similar BER of 1.56×10^{-5} for this experimental set-up.

The error performance in the previous experiment is different when the receiver moves. Therefore, in the next experiment two receivers are put at position 1 and 2. The BER performance is firstly evaluated based on each receiver and then the received signals from both receivers are processed jointly. Results are shown in Fig. 8 and the measured normalised channel gain values for LED1, LED2, LED9 and LED10 are [0.25, 0.37, 0.15, 1] at position 1 and [0.31, 0.61, 1, 0.79] at position 2. As discussed in Fig. 5 and Fig. 6, the channel gain differs from the same LED set to the receiver at different positions. The result in Fig. 8 shows that the error performance of GSSK is strongly dependent on the dissimilarity of the channel gain values. In addition, by using two receivers the error performance is significantly improved.

In the last experiment all 16 micro-LEDs and 4 APD receivers are used. The measurements are taken while running GSSK at different spectral efficiencies up to 16 bits/symbol. Results are shown in Table II and the results are measured without applying forward error correction (FEC). Several switching frequencies for the LEDs are selected from 5 MHz to 100 MHz. For a spectral efficiency of 8 bits/symbol, the measured BER is 1.6×10^{-5} at a switching frequency of 50 MHz (i.e. 400 Mbits/s). When the switching frequency is increased to 100 MHz resulting in a data rate of 800 Mbits/s, the BER goes up to 2×10^{-2}. This is because when the frequency increases, especially beyond the -3 dB bandwidth of the LED, the power gain of each LED drops resulting in a lower received SNR. For a switching frequency of 50 MHz and a spectral efficiency of 12 bits/symbol, the BER is 1.6×10^{-1} which is much higher than that of the case of 8 bits/symbol. As shown in previous result, it requires higher SNR for achieving the same BER performance at a higher spectral efficiency. The BER goes down while decreasing the switching frequency as the power gain of LED is higher at lower frequency. An operation at the maximum spectral efficiency of 16 bits/symbol while using 16 LEDs is demonstrated. The measured BER are 1.6×10^{-5} and 1×10^{-1} for 80 Mbits/s and 160 Mbits/s. There are some restrictions for the current 16 by 4 experimental set-up. Currently only 4 receiver boards are used without using any lens and each of them has a small active area thus there is significant optical power loss. In some links only a small part of the optical power from the LED is captured by the receiver. For such links when the switching frequency increases, the channel SNR drops significantly thus errors occur. However, the demonstration still shows the high data rate potential of GSSK.

TABLE II

Spectral Efficiency (bits/symbol)	Data Rate (Mbits/s)	BER
8	400	1.6E-5
8	800	2E-2
12	120	3.6E-4
12	300	8E-2
12	600	1.6E-1
16	80	1.6E-5
16	160	1E-1

V. CONCLUSIONS

An experimental set-up of GSSK using a micro-LED array and APD receivers is demonstrated in this work. A FPGA based GSSK encoder is implemented which is capable of driving up to 16 LEDs. An experiment is carried out showing the natural differences between the channel gain values of different links. This is the key concept of GSSK. It is shown that the channel gains can be quite unique from LEDs to the same receiver or from one LED to different receivers. More experiments are carried out evaluating the BER performance with different set-ups. The BER performance against received electrical SNR is presented in the cases of using 2, 3 and 4 LEDs with single receiver. For the demonstrated set-up, it is shown that about 5 dB higher SNR is required when one LED is added to the operation for achieving the similar BER of 1.56×10^{-5}. Results also show that the BER performance varies when receivers change their positions. It is a limitation of GSSK that the error performance is highly dependent on the dissimilarity of the channel gain values. However the performance can be improved by applying more receivers which increases the data dimensions in the ML decoder. It is shown that about 4 dB and 8 dB lower SNR is required for achieving the same BER of 10^{-3} while using two receivers compared to using single receiver at different positions respectively. The BER versus data rate measurements of applying different spectral efficiencies on a 16 by 4 GSSK set-up indicates the high data rate potential of GSSK. The BER results show that about 10^{-5} is achievable with the current set-up for the spectral efficiencies from 8 bits/symbol up to 16 bits/symbol. For further studies, the current experimental set-up will be improved by employing more receivers and using lenses to reduce the optical power loss.

ACKNOWLEDGMENT

This research was supported by the UK Engineering and Physical Sciences Research Council under Grant EP/K00042X/1.

REFERENCES

[1] A. M. Khalid, G. Cossu, R. Corsini, P. Choudhury, and E. Ciaramella, “1-Gb/s transmission over a phosphorescent white LED by using rate-adaptive discrete multitone modulation,” *IEEE Photon. J.*, vol. 4, no. 5, pp. 1465–1473, Oct. 2012.

[2] J. J. D. McKendry, D. Massoubre, S. Zhang, B. R. Rae, R. P. Green, E. Gu, R. K. Henderson, A. E. Kelly and M. D. Dawson, “Visible-light communications using a CMOS-controlled micro-light-emitting-diode array,” *J. Lightw. Technol.*, vol. 30, no. 1, pp. 61–67, 2012.

[3] D. Tsonev, H. Chun, S. Rajbhandari, J. McKendry, S. Videv, E. Gu, M. Haji, S. Watson, A. Kelly, G. Faulkner, M. Dawson, H. Haas, and D. O’Brien, “A 3-Gb/s Single-LED OFDM-Based Wireless VLC Link Using a Gallium Nitride μLED,” *IEEE Photon. Technol. Lett.*, vol. 26, no. 7, pp. 637–640, Apr. 2014.

[4] K.-I. Ahn and J. Kwon, “Capacity analysis of m-pam inverse source coding in visible light communications,” *Journal of Lightwave Technology*, vol. 30, no. 10, pp. 1399–1404, May 2012.

[5] J. Armstrong, “OFDM for Optical Communications,” *J. Lightw. Technol.*, vol. 27, no. 3, pp. 189–204, Feb. 2009.

[6] D. Barros, S. Wilson, and J. Kahn, “Comparison of orthogonal frequency-division multiplexing and pulse-amplitude modulation in indoor optical wireless links,” *IEEE Transactions on Communications*, vol. 60, no. 1, pp. 153–163, 2012.

[7] H. Elgala, R. Mesleh, and H. Haas, “Impact of LED nonlinearities on optical wireless OFDM systems,” in *2010 IEEE 21st International Symposium on Personal Indoor and Mobile Radio Communications (PIMRC)*, sept 2010, pp. 634 – 638.

[8] T. Fath and H. Haas, “Performance Comparison of MIMO Techniques for Optical Wireless Communications in Indoor Environments,” *Communications, IEEE Transactions on*, vol. 61, no. 2, pp. 733 – 742, 2013.

[9] R. Mesleh, H. Haas, C. W. Ahn, and S. Yun, “Spatial Modulation – A New Low Complexity Spectral Efficiency Enhancing Technique,” in *IEEE International Conference on Communication and Networking in China (CHINACOM)*, Beijing, China, Oct. 25–27, 2006, pp. 1–5.

[10] R. Mesleh, H. Haas, S. Sinanović, C. W. Ahn, and S. Yun, “Spatial Modulation,” *IEEE Trans. on Veh. Tech.*, vol. 57, no. 4, pp. 2228 – 2241, Jul. 2008.

[11] M. Di Renzo, H. Haas, and P. M. Grant, “Spatial modulation for multiple-antenna wireless systems: a survey,” *Communications Magazine, IEEE*, vol. 49, no. 12, pp. 182 – 191, 2011.

[12] R. Mesleh, R. Mehmood, H. Elgala, and H. Haas, “Indoor MIMO Optical Wireless Communication Using Spatial Modulation,” in *IEEE International Conference on Communications (ICC)*, Cape Town, South Africa, May 22–27 2010, pp. 1–5.

[13] R. Mesleh, H. Elgala, and H. Haas, “Optical Spatial Modulation,” *IEEE/OSA J. Opt. Commun. Netw.*, vol. 3, no. 3, pp. 234–244, Mar. 2011, ISSN: 1943-0620.

[14] J. Jeganathan, A. Ghrayeb, L. Szczecinski, and A. Ceron, “Space Shift Keying Modulation for MIMO Channels,” *IEEE Trans. on Wireless Commun.*, vol. 8, no. 7, pp. 3692–3703, Jul. 2009.

[15] J. Jeganathan, A. Ghrayeb, and L. Szczecinski, “Generalized Space Shift Keying Modulation for MIMO Channels,” in *Proc. IEEE 19th Intern. Symp. on Personal, Indoor and Mobile Radio Commun. PIMRC 2008*, Cannes, France, 15–18 Sep. 2008, pp. 1–5.

[16] T. Fath, M. Di Renzo, and H. Haas, “On the performance of space shift keying for optical wireless communications,” in *IEEE GLOBECOM Workshops (Globecom 2010) - Workshop on Optical Wireless Communications*, Miami, FL, USA, 6-10 Dec. 2010, pp. 990 – 994.

[17] W. Popoola, E. Poves, and H. Haas, “Generalised space shift keying for visible light communications,” in *8th International Symposium on Communication Systems, Networks & Digital Signal Processing (CSNDSP 2012)*, Poznan, Poland, 18-20 July 2012, pp. 1 – 4.

[18] W. Popoola, E. Poves, and Haas, “Error Performance of Generalised Space Shift Keying for Indoor Visible Light Communications,” *IEEE Transactions on Communications*, pp. 1–9, 2013.

[19] Y. Sun, D. Borah, and E. Curry, “Optimal symbol set selection in gssk visible light wireless communication systems,” vol. 28, no. 3, pp. 303–306.

[20] K. Ebihara, K. Kamakura, and T. Yamazato, “Spatially-modulated space-time coding in visible light communications using 22 led,” in *Circuits and Systems (APCCAS), 2014 IEEE Asia Pacific Conference on*, Nov. 2014, pp. 320–323.

[21] W. Popoola and H. Haas, “Demonstration of the merit and limitation of generalised space shift keying for indoor visible light communications,” vol. 32, pp. 1960–1965.

[22] S. Rajagopal, R. D. Roberts, and S.-K. Lim, “Ieee 802.15.7 visible light communication: Modulation schemes and dimming support,” vol. 50, no. 3, pp. 72–82.

10.2 Gb/s visible light communication with off-the-shelf LEDs

Rui Bian*, Iman Tavakkolnia, Harald Haas

Li-Fi Research and Development Centre, Institute for Digital Communications
School of Engineering, University of Edinburgh, Edinburgh, UK. *r.bian@ed.ac.uk

Abstract *A 10 Gb/s data rate is demonstrated experimentally for optical communication using three inexpensive off-the-shelf LEDs for the first time. An OFDM-based wavelength division multiplexing structure is used for efficiently utilizing the available bandwidth of the LEDs.*

Introduction

The radio frequency (RF) spectrum is saturated and cannot keep up with the ever increasing demand for high data rates originating from emerging new smart technologies. The visible light spectrum is readily available for communication purposes, and high speed data transmission has already been demonstrated using wireless optical communication. Light Fidelity (LiFi) is known as a high speed wireless access network that combines illumination and visible light communication (VLC) techniques using light emitting diodes (LEDs)[1]. The simple intensity modulation and direct detection (IM/DD) approach is mainly used to modulate data on available incoherent light sources. Moreover, spectrally efficient multicarrier modulation techniques, such as optical orthogonal frequency division multiplexing (OFDM) are also optimized for VLC. In spite of the large spectrum available for data transmission in VLC, the limited bandwidth of the light sources makes it difficult to exploit all the available spectrum efficiently. Therefore, different methods, such as multiple-input-multiple-output (MIMO)[2] and wavelength division multiplexing (WDM)[3], are used to increase the spectral efficiency. It is reported that using custom-made micro-sized Gallium Nitride (GaN) LEDs (μLEDs) a data transmission rate of about 8 Gb/s is achieved using a single pixel[4], while over 10 Gb/s is achieved by using three-color WDM[5]. These custom-fabricated μLEDs have much higher bandwidth but significantly lower output optical power compared to commercially available LEDs which are designed for illumination rather than data communication. Previously, 8 Gb/s[6] and 10.7 Gb/s[7] were demonstrated using four-color and five-color LED-based WDM with post or pre equalization respectively. Both works presented the overall data rate as the summation of all individual color links. However, the implementation method for separating the combined beam and simultaneous detection at the receiver side was not introduced. This is an essential part of a practical system where all individual links carry the data simultaneously.

In this paper, for the first time we demonstrate a 10.2 Gb/s WDM-VLC link without pre or post equalization using three high brightness off-the-shelf LEDs at a price of less than 50 US cents ($0.50). Three single color LEDs, blue, green and red, are utilized for WDM. And OFDM with adaptive sub-carrier bit loading is used to enhance the spectral efficiency. The results presented in this paper prove that high speed communication is possible using available inexpensive off-the-shelf components. Different optical components (e.g., lenses and mirrors) are incorporated for the WDM design presented, which can be integrated into compact transmitter and receiver units for real applications such as Internet-of-things (IoT).

Experimental Set-up

For IM/DD optical communication, some variants of OFDM are used because the input signal needs to be real and positive[1]. We use DC-biased optical OFDM (DCO-OFDM). A real-valued OFDM signal is first generated using a Hermitian symmetric OFDM frame which effectively makes half of the data redundant. Then, the real-valued signal is made positive by adding a DC bias. The DC-bias and the peak-to-peak amplitudes are determined to minimize the effect of signal clipping and nonlinearity of the LED. Before data transmission, the effective signal-to-noise ratio (SNR) of the whole system is estimated using a mean estimator with random pilots. Assuming a M-QAM modulation format, the modulation order M_k is adaptively chosen based on the estimated SNR at kth subcarrier in order to achieve an overall target bit error rate (BER). The data rate is calculated as

$$R = \frac{\sum_{k=1}^{\frac{N_{\mathrm{FFT}}}{2}} \log_2 M_k}{(N_{\mathrm{FFT}} + N_{\mathrm{CP}})/2B}, \qquad (1)$$

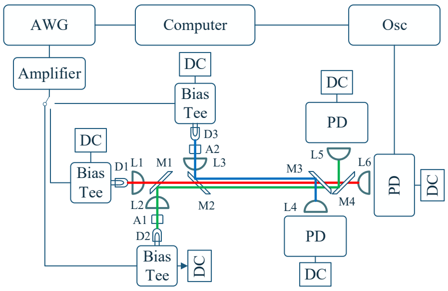

Fig. 1: The experimental set-up for WDM-VLC system

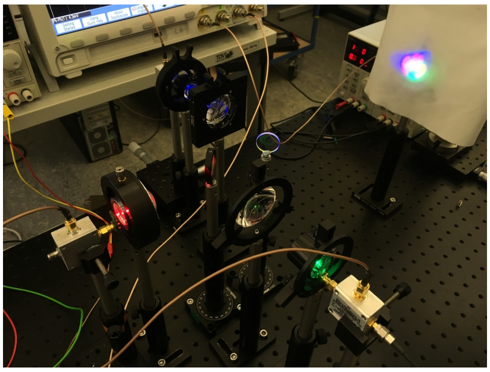

Fig. 2: The picture of transmitter side in the experimental set-up.

where B, N_{FFT} and N_{CP} are the modulation bandwidth, fast Fourier transform (FFT) size and cyclic prefix size. In this paper, the target bit error rate (BER) is chosen as the hard decision forward error correction (HDFEC) BER threshold 3.8×10^{-3}, and the number of active subcarriers is $N = N_{\mathrm{FFT}}/2 = 1024$. The details of adaptive OFDM bit loading can be found in references[3–5].

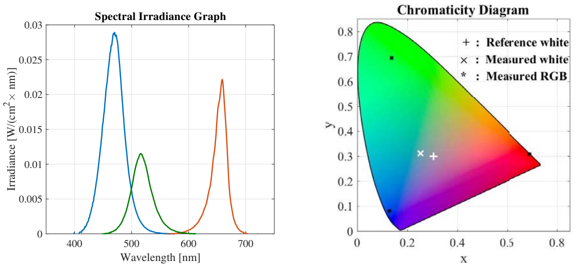

Fig. 3: The spectral irradiance measurements and chromaticity diagram for individual red, green and blue LEDs and mixed white illumination.

Figs. 1 and 2 show the experimental set-up for this paper. The digital data is generated using MATLAB code and is sent to an arbitrary waveform generator (AWG: M8195A) with sampling rate up to 16 GSa/s for four channels. The generated analogue signal is then amplified (ZHL-1A-S+) and sent to the LED through a bias-tee (ZFBT-4R2GW), which is used to mix the DC bias and the OFDM signal for each LED. The LEDs are chosen in three colors: red (D1: VLMS1500-GS08), green (D2: VLMTG1300-GS08) and blue (D3: VLMB1500-GS08). The optical signal generated by each LED is collimated using aspheric condenser lenses (L1-6: ACL4532). An additional condenser lens assembly (A1-2: 01TA25) is used for the blue and green colors to correct the spot of light incident to the dichroic mirrors. One dichroic mirror (M1: DLMP567) is used to reflect the green signal while it passes the red signal. The transmission band for this mirror is 584-800 nm. Another dichroic mirror (M2: DLMP490), with transmission band 505-800 nm, is used to reflect the blue signal while it passes the other two colors. The dichroic mirrors are chosen based on the spectral irradiance measurement results for individual red, green and blue LEDs as shown in Fig. 3. The link length for all colors is 50 cm. Fig. 3 also shows the measured chromaticity diagram values for both all individual LEDs and the combined beam with a reference value of white LED (VLMW1500-GS08) taken from its datasheet. The combination of three beams results in a white spot at the receiver side.

At the receiver side, the same configuration of mirrors (M3: DLMP490, M4: DLMP567) are used to separate different colors. Another lens is used to focus the light into the detection area of the high bandwidth photo detector (PD: New Focus 1601). The -3 dB bandwidth of this PD is 1 GHz. The received signal is captured by a high-speed oscilloscope (Osc: MSO7104B), which sends the data to a computer for processing with the MATLAB software. Note that the size of set-up presented here can be minimized, probably to the size of available lamps used for illumination only.

Results

LEDs are nonlinear light sources and cause nonlinear distortion especially in high speed data transmission. An important factor is the operation point (bias voltage and current) of each LED, which along with the signal peak-to-peak amplitude determine the amount of distortion. The optimum bias point is found by several single-color experiments. The optimum bias current I_b and voltage V_b are presented in Table. 1 for each LED. Since the characteristics of the output light varies with different bias points, the peak wavelength λ_{peak} and output power at peak wavelength P_{out} along with the chosen peak-to-peak voltage V_{pp} are also presented in Table. 1.

The estimated channel gain and measured SNR are shown in Fig. 4. While SNRs at different wavelengths are almost equal for different colors, the channel gains are different. The channel

Tab. 1: The chosen bias points and experiment results.

	I_b [mA]	V_b [V]	λ_{peak} [nm]	P_{out} [mW]	V_{pp} [V]	N_{S}	BER	R [Gb/s]
Red	125	2.6	660	4.89	0.85	852	0.0020	3.48
Green	105	4.4	516	2.14	0.80	869	0.0021	3.65
Blue	130	4.5	477	5.23	0.85	886	0.0018	3.81

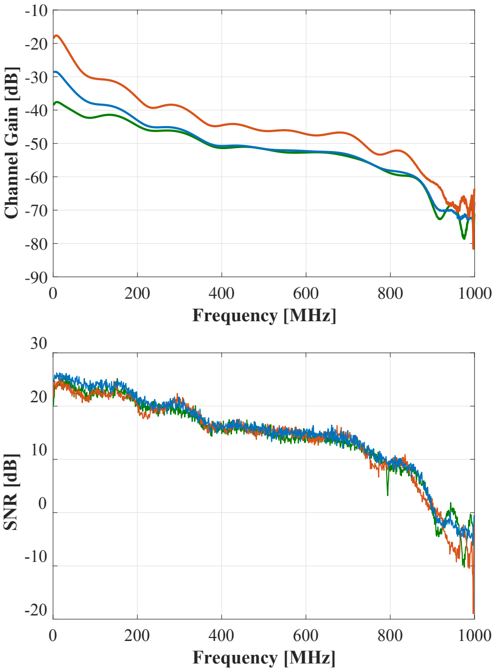

Fig. 4: The measured channel gain and SNR at different subcarriers for red, green and blue LEDs.

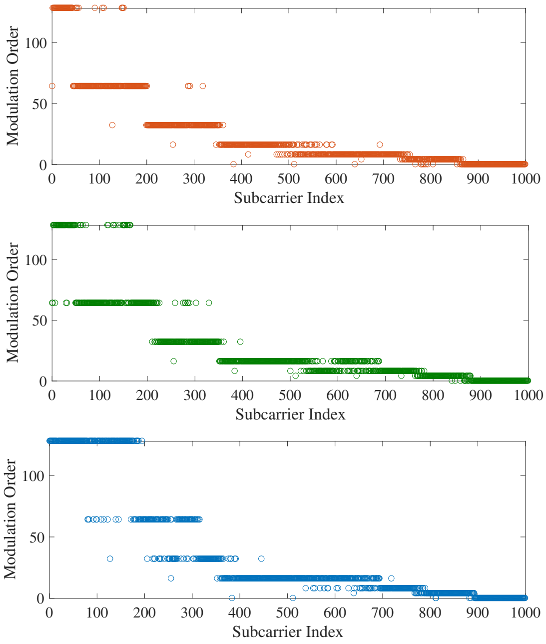

Fig. 5: The modulation order chosen for each subcarrier for colors red, green and blue LEDs.

gain for red is higher because the used receiver has a maximum responsivity at peak wavelength of 0.45 A/W for red while 0.28 A/W and 0.24 A/W for green and blue. In addition, there is a loss for all the colors at the mirrors for some parts of the spectrum being reflected (for red and green) or passed (for green and blue) through the mirrors and not reaching the receiver. The -3 dB bandwidth of LEDs are about 33 MHz for red and blue LEDs and 65 MHz for green LED. However, frequencies higher than the -3 dB bandwidth can be used for data transmission as the SNR drops gradually and stays usable for conveying information. In this work up to 1 GHz of bandwidth is used for data modulation of all LEDs. The modulation orders allocated to each subcarrier is shown in Fig. 5. The number of used subcarriers N_{S}, BER and data-rate R are shown in Table 1. The aggregate achievable data rate is 10.94 Gb/s which reduces to 10.17 Gb/s after 7% HDFEC overhead reduction.

Conclusion

We have presented experimental results of a 10.2 Gb/s VLC WDM system, using off-the-shelf RGB LEDs which are available at a cost of less than 50 US cents. The three individual color links carry the data simultaneously while the beams being combined at the transmitter side and then separated at the receiver side. The system offers high wireless data transmission rate with high bright white illumination which makes it a potential candidate for practical LiFi applications.

References

[1] H. Haas et al., “What is LiFi?” *J. Lightwave Technol.*, Vol. 34, no. 6, p. 1533 (2016).

[2] S. Rajbhandari et al., “A Multigigabit per Second Integrated Multiple-Input Multiple-Output VLC Demonstrator,” *J. Lightwave Technol.*, Vol. 35, no. 20, p. 4358 (2017).

[3] D. Tsonev et al., “Towards a 100 Gb/s visible light wireless access network,” *Opt. Express*, Vol. 23, no. 2, p. 1627 (2015).

[4] M. Islim et. al, “Towards 10 Gb/s orthogonal frequency division multiplexing-based visible light communication using a GaN violet micro-LED,” *Photon. Res.*, Vol. 5, no. 2, p. A35 (2017).

[5] H. Chun et al., “LED Based Wavelength Division Multiplexed 10 Gb/s Visible Light Communications,” *J. Lightwave Technol.*, Vol. 34, no. 13, p. 3047 (2016).

[6] Y. Wang et al., “8-Gb/s RGBY LED-based WDM VLC system employing high-order CAP modulation and hybrid post equalizer,” *IEEE Photon. J.*, Vol. 7, no. 6, p. 1 (2015).

[7] X. Zhu, et al., “10.72 Gb/s Visible Light Communication System Based On Single Packaged RGBYC LED Utilizing QAM-DMT Modulation With Hardware Pre-Equalization,” in *Optical Fibre Communication*, paper M3K-3 (2018).

15.73 Gb/s visible light communication with off-the-shelf LEDs

Rui Bian, Iman Tavakkolnia, and Harald Haas

***Abstract*—Visible light communication (VLC) can provide high speed data transmission that could alleviate the pressure on the conventional radio frequency (RF) spectrum with the looming capacity crunch for digital communication systems. In this paper, we present the experimental results of a VLC system with a data rate of 15.73 Gb/s after applying forward error correction (FEC) coding over a 1.6 m link. Wavelength division multiplexing (WDM) is utilized to efficiently modulate four wavelengths in the visible light spectrum. Four single color low-cost commercially available light emitting diodes (LEDs) are chosen as light sources. This confirms the feasibility and readiness of VLC for high data rate communication. Orthogonal frequency division multiplexing (OFDM) with adaptive bit loading is used. The system with the available components is characterized and its parameters, such as LED driving points and OFDM signal peak-to-peak scaling factor, are optimized. To the best of our knowledge, this is the highest data rate ever reported for LED-based VLC systems.**

***Index Terms*—Light Fidelity (LiFi), Orthogonal frequency division multiplexing (OFDM), Wavelength division multiplexing (WDM), Visible light communication (VLC), Experimental demonstration, off-the-shelf component.**

I. INTRODUCTION

IT is widely accepted that new high capacity communication technologies are required for the future generation of wireless communication networks. Recent forecasts show that the entire radio frequency (RF) spectrum will be saturated in the near future [1] due to the exponential growth of data traffic powered by new applications and services. Optical wireless communication (OWC) is an alternative technology that can work as a complementary system to compensate shortcomings of RF technologies. OWC is favourable because of its large available unlicensed bandwidth, immunity to electromagnetic interference, inherent security and cost-effectiveness [2]. Also, the wide availability of incoherent transmitter and receiver units makes simple intensity modulation and direct detection (IM/DD) an efficient and straightforward option. Visible light communication (VLC) is a subclass of OWC that operates in the visible light spectrum (i.e., 390-700 nm), and thus, the existing illumination infrastructure can be exploited for data transmission as well. Recently, light-fidelity (LiFi) has been proposed as a fully networked bidirectional system which can work independently or cooperate with existing RF systems creating a hybrid network [3].

Different communication system structures have been adopted for VLC, in order to increase the achievable data rate and spectral efficiency [3]–[5]. Orthogonal frequency division multiplexing (OFDM) is regarded as a natural choice of modulation scheme due to its high spectral efficiency and immunity to channel frequency selectivity. The relatively low bandwidth of common phosphor-coated white LEDs (i.e., several MHz) causes a significant limit on the achievable data rate [6]. This limitation originates from the slow response of the yellow phosphor coating. Therefore, several single color LEDs, without any coating, with much larger bandwidths can be utilized for both communication and illumination. A combination of three or four colors can used for both white illumination as well as high data rate wireless communication. This is referred to as wavelength division multiplexing (WDM), where each single color LED can be modulated independently. As a result, parallel data streams can be transmitted leading to a high communication data rate.

Over the past few years several Giga-bit-per-second experimental WDM-VLC demonstrations have been reported [7]. Laser-based experiments have shown achievable data rates up to 25 Gb/s for underwater VLC [8]–[12]. However, laser-based VLC requires consideration of eye-safety limitation which may significantly reduce the achievable data rates. To the best of our knowledge the highest achieved “eye-safe” data-rate is 8.8 Gb/s over 50 cm [13]. On the other hand, eye-safty is not an issue in LED-based VLC, but the available bandwidth and optical power are much smaller in LEDs. Data rates up to 7.36 Gb/s are reported with custom-made micro-sized Gallium Nitride (GaN) LEDs (μLEDs) as the light source [14], [15]. μLEDs have much higher bandwidth but lower output optical power compared to commercially available LEDs. The combination of several single color LEDs/μLEDs with WDM has enabled data rates up to 10.7 Gb/s [16]–[19].

In this paper a record data rate of 15.73 Gb/s is reported using available inexpensive off-the-shelf LEDs at a price of less than 50 US cents ($0.50). The link distance is 1.6 m. WDM is used with four LED colors, namely, red (R), green (G), blue (B) and yellow (Y). The single color beams are combined at the transmitter side (Tx) and separated at the receiver side (Rx) using three commercially available dichroic mirrors. Moreover, OFDM with adaptive bit loading [20] is utilized to maximize the spectral efficiency of each LED. The chosen LEDs are designed for illumination rather than data communication, and thus, system parameters, such as LED bias points and signal peak-to-peak amplitude, should be carefully optimized to reduce the effect of LED non-linearity, which can significantly affect the performance of OFDM. Also, it is shown that the high bandwidth PIN silicon optical receivers could be replaced by simple inexpensive receiver circuits to further decrease the component cost. This alteration results in 7.67 Gb/s of data rate.

R. Bian, I. Tavakkolnia and H. Haas are with the Li-Fi Research and Development Centre, Institute for Digital Communications, School of Engineering, University of Edinburgh, Edinburgh, EH9 3FD, UK. e-mail:{r.bian, i.tavakkolnia, h.haas}@ed.ac.uk

The rest of this paper is organized as follows. The data transmission and modulation scheme is explained in Section II-A. The experimental set-up and components used for the investigation are described in Section II-B. The experiment results are presented in Section III. Finally, concluding remarks are given in Section IV.

II. SYSTEM DESIGN

In this section the basics of the data transmission method and elements of the communication system are presented.

A. Data Transmission

OFDM is proved to be a spectrally efficient modulation scheme and a favourable choice in VLC [21], [22]. Among possible choices of OFDM variants for VLC, direct curent biased optical OFDM (DCO-OFDM) is chosen due to its simplicity and high spectral efficiency [3]. Since IM/DD is used in VLC, the signal should be both real and non-negative. Thus, Hermitian symmetry is imposed on the symbols of a subcarrier block $X[k]_{k=1}^{N_{\mathrm{FFT}}}$, where N_{FFT} is the number of subcarriers. This halves the number of available subcarriers for data transmission as $X^*[k] = X[N_{\mathrm{FFT}} - k]$. Also, $X[0] = X[N_{\mathrm{FFT}}/2] = 0$ because of the direct current (DC) bias. The resulting time domain signal is then clipped to avoid large values which increase the effect of nonlinearity or may harm the LED. WDM can be utilized including several visible light wavelengths that allow parallel transmission of OFDM data streams at each wavelength. Filters are used to separate signals at each wavelength. The corresponding channel model for ith wavelength can be expressed as

$$y_i(t) = g_i\left(x_i(t)\right) + n_i(t), \tag{1}$$

where $g_i(.)$ is the overall channel including the effects optical channel and front-end devices. $n_i(t)$ is and additive white Gaussian noise (AWGN) consisting any noise origin, such as thermal and shot noise. It can be assumed that $g_i\left(x_i(t)\right) = h_i(t) * w_i\left(x_i(t)\right)$, where $h_i(t)$ is the optical channel response and $w_i(.)$ is the nonlinear distortion of the LED [23]. It is shown that this nonlinearity distortion can be modeled as a Gaussian process [24]. Usually, the LED can be assumed to be the dominant source of nonlinearity. As it will be detailed in Section II-B, the nonlineairty of photoreceivers, amplifiers and other components are negligible compared to the LED.

Different phenomena in an experimental set-up affect the overall frequency response of the communication system and make it frequency-dependent. For instance, the interference from ambient light sources or other optical wavelengths, the frequency-dependent response of front-end devices and the optical channel itself can affect the overall frequency response. Therefore, the modulation order can be selected adaptively at each subcarrier to maximize the achievable data rate at a target bit error rate (BER) [20]. Thus, SNR estimation is required at each subcarrier prior to data transmission. The channel and available SNR at each subcarrier SNR_k is estimated using pilots composed of several OFDM blocks. Details of the estimation method can be found in [8]. It should be noted that the overall communication channel is considered in this SNR estimation including all the affecting phenomena, such as attenuation, noise and nonlinear distortion. M_k-QAM modulation format is considered where the modulation order at each subcarrier M_k is determined by the available SNR and target BER. The BER of a M_k-QAM modulation format with SNR_k can be approximated as [25]

$$\begin{aligned} \mathrm{BER}\left(M_k, \mathrm{SNR}_k\right) \simeq \frac{4\left(1-\frac{1}{\sqrt{M_k}}\right)}{\log_2 M_k} \\ \times \sum_{l=1}^{\min(2,\sqrt{M_k})} \mathrm{Q}\left((2l-1)\sqrt{\frac{3\mathrm{SNR}_k}{2\left(M_k-1\right)}}\right) \end{aligned} \tag{2}$$

where $\mathrm{Q}(.)$ is the Gaussian Q-function. Therefore, using the iterative algorithm for bit loading the modulation orders M_k are determined, and the overall data rate is given by [8]

$$R = \frac{\sum_{k=1}^{\frac{N_{\mathrm{FFT}}}{2}} \log_2 M_k}{(N_{\mathrm{FFT}} + N_{\mathrm{CP}})/2B}, \tag{3}$$

where B is the single-sided modulation bandwidth of the system, and N_{CP} is the cyclic prefix size. It should be emphasized that after SNR estimation and adaptive bit loading, multiple OFDM blocks are transmitted through the communication channel according to the determined bit loading and the actual BER is then measured. This ensures that the overall BER of the system is below the target BER. In this paper, we consider a hard decision forward error correction coding (HDFEC) threshold of 3.8×10^{-3} which imposes 7% coding overhead [26].

B. Experimental Set-up

In this section the details of the experimental set-up are presented. As mentioned earlier, WDM using four single color LEDs is used. WDM can be realized in different structures. For instance, only bandpass filters at the receiver side may be used for detecting each wavelength individually [17], or a combination of bandpass filters at the Rx and dichroic mirrors at the Tx may be selected [8]. In this paper, dichroic mirrors are used in both Tx and Rx because the spectrum of each single color LED is large and available narrowband bandpass filters will result in significant power loss. Dichroic mirrors are basically high-pass filters which pass wavelengths larger than a certain value and reflect shorter wavelengths. Moreover, it is possible to efficiently (i.e., minimal loss of optical power) combine and separate all four colors using the same combination of condenser lenses and dichroic mirrors respectively at Tx and Rx.

Fig. 1 shows optical power spectrum of LEDs used in this experiment at their nominal driving current. These LEDs are chosen from VLM series LEDs by Vishay Semiconductors designed for small-scale high brightness applications [27]. The model number of RGBY LEDs are L1: VLMS1500-GS08, L2: VLMTG1300-GS08, L3: VLMB1500-GS08 and L4 VLMY1500-GS08, respectively. The dimension of LEDs are $1 \times 0.5 \times 0.35$ mm for red, blue and yellow LEDs, and $1.6 \times 0.8 \times 0.8$ mm for the green LED. The scaled picture of a blue LED is shown in the inset of Fig. 1.

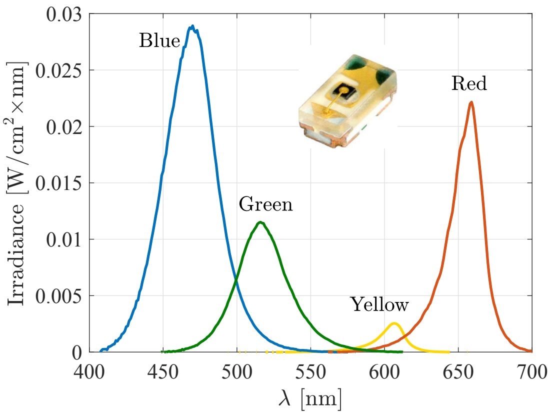

Fig. 1: Measured optical spectrum of RGBY sources. Inset: The picture of an individual LED [27].

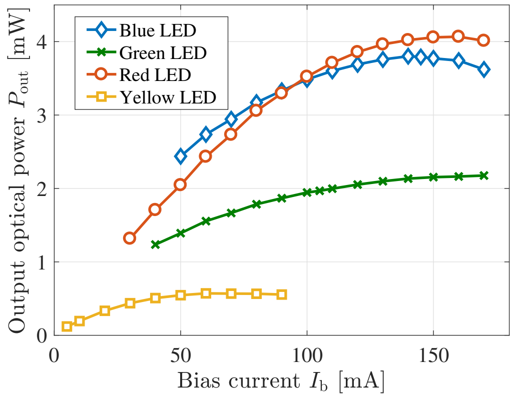

Fig. 2: Optical power output at different driving current different LED colors.

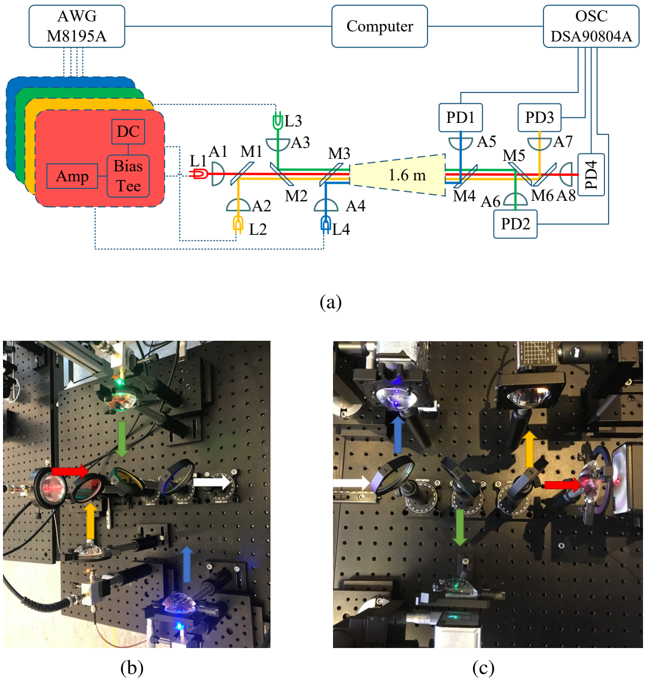

(a)

(b)

(c)

Fig. 3: (a) Block diagram of the experimental system, (b) Picture of the set-up at the transmitter side Tx. (c) Picture of the set-up at the receiver side Rx.

A crucial parameter of the experiment is the deriving current point of each LED which determines the available signal amplitude range and the distortion caused by nonlinearity. Since these LEDs are manufactured for purposes other than data communication, their communication characteristics differ for each model. It can be seen in Fig. 2 that the output powers of LEDs are significantly different, and for instance, the output power of the yellow LED is always small. Therefore, it is essential to carefully measure the effect of different driving points and choose the optimum point. This will be studied in the next section.

The system block diagram and pictures are shown in Fig. 3. The DCO-OFDM signal generation and analysis is performed on a PC using MATLAB. Generated signals are sent to the arbitrary waveform generator (AWG: Keysight M8195A). The sampling rate of the AWG is 16 GSa/s and the resolution of the digital-to-analog (DAC) unit of the AWG is 8 bits. Each output signal from AWG is amplified by an amplifier module (Amp: Mini-Circuits ZHL-1A-S+) and fed into Bias-Tees (Mini-Circuits ZFBT-4R2GW). The Bias-Tee is used to combine the OFDM information signal with the DC bias which comes from a DC power supply. The Bias-Tee's output is connected to the LED source. Since the half-power semiangle of LEDs are wide (i.e., about 65° [27], aspheric condenser lenses (A1-4: Thorlabs ACL4532) are used at Tx to collimate the output light of each LED. One dichroic mirror (M1: Thorlabs DLMP605L) is used to reflect the yellow signal while it passes the red signal. The transmission band for this mirror is 620-800 nm with a cut-off wavelength of 605 nm. Another dichroic mirror (M2: Thorlabs DLMP567L), with transmission band 584-800 nm with cut-off wavelength 567 nm, is used to reflect the green signal while it passes the other two colors. The third one, (M3: Thorlabs DMLP490L), with transmission band 505-800 nm and cut-off wavelength 490 nm, reflects the blue signal and passes the others. It should be noted that mirrors are chosen based on the measured spectrum of LEDs among commercially available dichroic mirrors.

At the receiver side at a link distance of 1.6 m, the same configuration of mirrors (M4-6) and aspheric condenser lenses (A5-8) is applied to separate each color and focus the light into the detection area of the high bandwidth positive-intrinsic-negative (PIN) diode photo detector (PD: New Focus 1601 AC). This receiver has a -3 dB bandwidth of 1 GHz. The gain of the receiver built-in transimpedance amplifier (TIA) is 10 V/mA. The received signal is captured by a high-speed oscilloscope (OSC: Agilent DSA90804A) and then sent back to PC to be processed.

III. Data Transmission Results

In this section, details of the data transmission results are presented. First, the driving point for each LED is optimised. Next, the peak-to-peak scaling factor of the OFDM signal

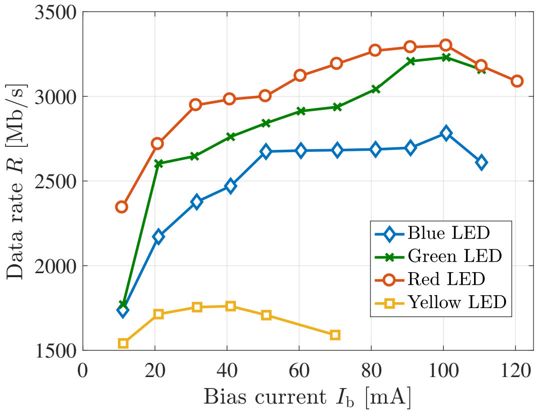

Fig. 4: The measured data rate for different I_b.

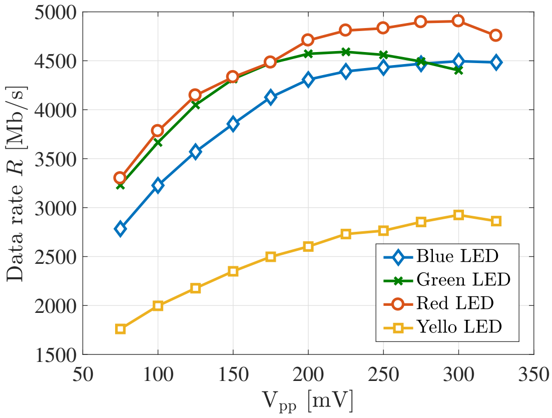

Fig. 5: The measured data rate for different V_pp.

TABLE I:
THE SUMMARY OF EXPERIMENT RESULTS.

	P_out [mW]	N_act	BER	R [Gb/s]
Red	3.52	890	0.0025	4.904
Green	1.94	887	0.0027	4.591
Blue	3.49	865	0.0036	4.796
Yellow	0.5	811	0.0028	2.925

is determined. Experimental measurement results are also presented in details.

As mentioned earlier, driving points of LEDs determine achievable data rates and output optical powers. The driving point of each LED is found so that the amount of nonlinear distortion is minimized, and consequently, the available SNR for data transmission is maximized. When the driving point is selected, the OFDM signal can be scaled to fit in the linear operation region of each LED. This is performed by adjusting the maximum peak-to-peak voltage (V_pp) at the output of the AWG. Note that the signal is amplified after the AWG before being applied to LEDs. The overall gain from AWG to LEDs is about 13 dB including losses in components such as the bias-Tee.

The same experimental set-up, as in Fig. 3, is used for driving point optimization. The modulation bandwidth is 1GHz, and the number of subcarries is 1024. First, the minimum possible V_pp of the AWG, equal to 75 mV, is chosen to minimize the nonlinearity distortion of LEDs. Next, the bias current is gradually increased, and the data rate is measured using the algorithm explained in Section. II-A. The results are shown in Fig. 4 and it can be seen that each LED demonstrates different behaviour. Maximum data rates are found at $I_\text{b} = 100$ mA for RGB LEDs and $I_\text{b} = 40$ mA for the yellow LED. The bias voltages of RGBY LEDs are, respectively, 2.38 V, 3.85 V, 4.01 V, and 2.15 V. At the selected operating points of LEDs, the optimum V_pp for each LED is also found by gradually increasing its value and measuring the data rate. The corresponding results are demonstrated in Fig. 5. The optimum values of V_pp are 300 mV for red, blue and yellow LEDs, and 225 mV for the green LED. Therefore, the operation point of each LED is determined which results in the highest achievable data rate.

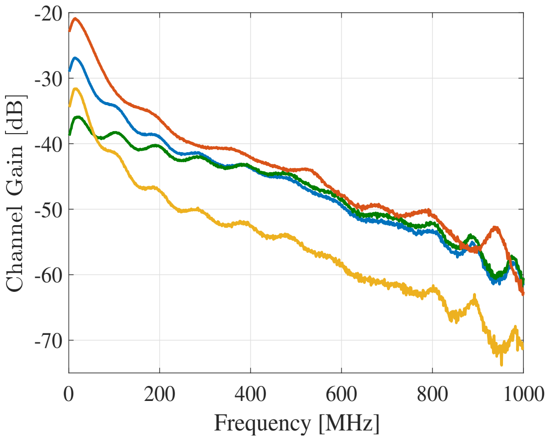

Fig. 6: The measured channel gains for four colors.

The summary of the data rate measurement results are provided in Table I. An aggregate bit rate 16.92 G/s is achieved which reduces to 15.73 Gb/s after removing the 7% HDFEC coding overhead. It can be seen that the BER is below the threshold of 3.8×10^{-3} for all LEDs. The number of active subcarriers N_act (i.e., non-zero modulation order) and the output optical power P_out of each LED is also included in Table I. The data rate for the white LED of the same series (VLMW1300-GS08) was also measured using the same procedure (a direct link and no dichroic mirror) for comparison with the aggregate data rate achieved with the WDM system. It was observed that only 3.53 Gb/s can be achieved with BER 1.2×10^{-3}. The measured output optical power of the white LED was 7.13 mW. This implies that while the output optical power of the white LED is 42% lower that the aggregate output optical powers of RGBY LEDs, its measured data rate is 79% lower. This confirms that utilizing WDM significantly increases the power efficiency of VLC systems.

The overall frequency responses of the system for each color are depicted in Fig. 6. The measured SNR and bit loading results are also shown in Fig. 7. Frequency responses are affected by all individual components of the communication. For instance, the frequency response and the responsivity

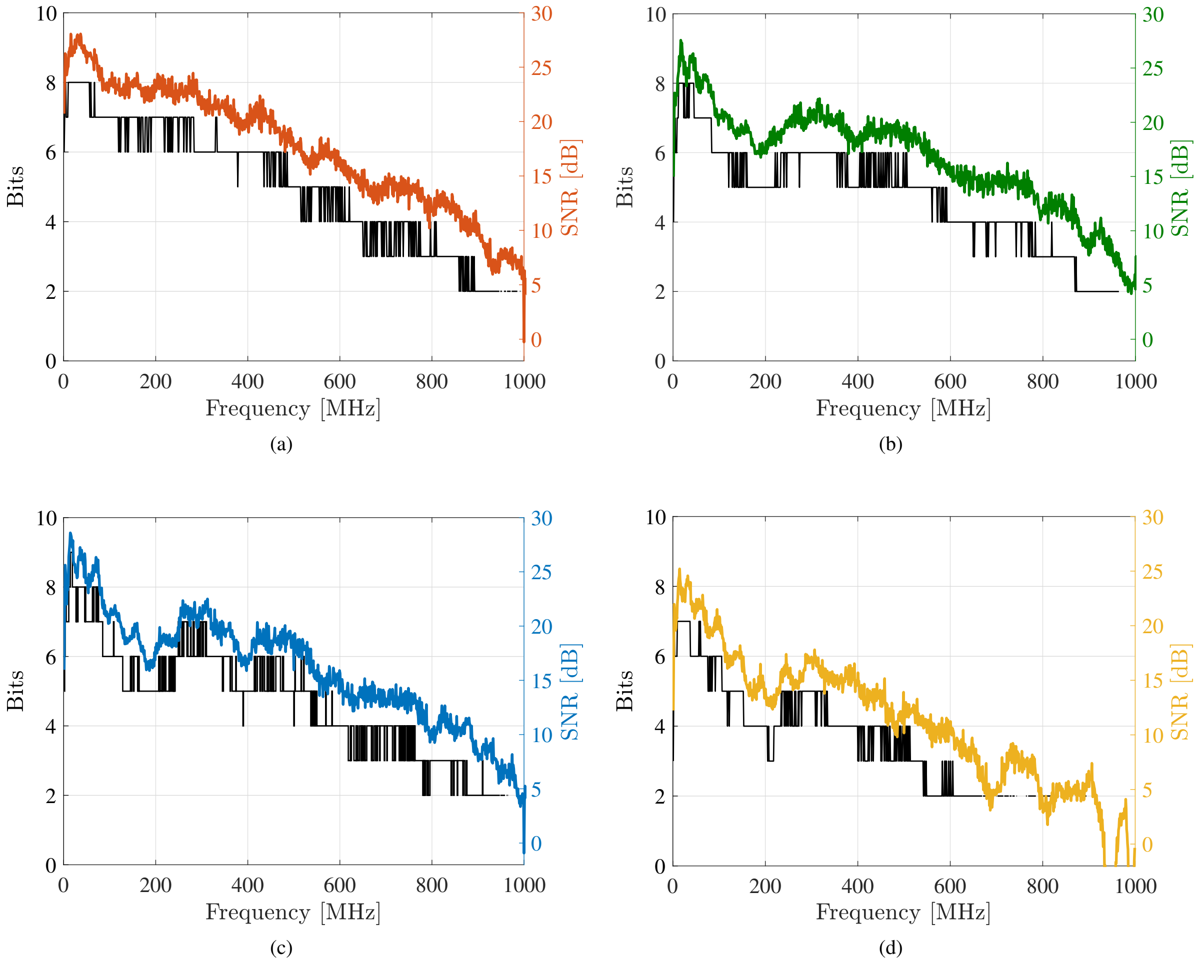

(a)

(b)

(c)

(d)

Fig. 7: (a)-(d) The measured SNR and adaptively allocated bit to each subcarrier for RGBY LEDs respectively.

of the PD at each wavelength affects the overall frequency response. Moreover, the amount of the optical power reaching the receiver is a determining factor. Since LEDs and dichroic mirrors are chosen from commercially available products, their spectrum is not as optimum as possible, and some part of the energy is lost at the mirrors. For instance, the mirror M1 in Fig. 3 passes some part of the incident light from the yellow LED which does not reach the receiver. In a separate experiment with the same link distance, the achievable data rate for single color transmission was measured. Each single LED was placed at the position of the red LED in Fig. 3 without any mirror. The obtained data rates where 5.13 Gb/s, 5.26 Gb/s, 5.22 Gb/s and 4.15 Gb/s corresponding to respective data rate decrease of 4%, 11%, 14%, and 30% when the full WDM system is used. We infer that if optimum mirrors where available, a potential data rate of 19.66 Gb/s could be achieved (i.e., 18.28 Gb/s after 7% HDFEC coding overhead reduction).

Results of an extra experiment are also presented here, in which a simple inexpensive receiver board is used. The receiver board is fully designed and produced in the lab and replaces the high bandwidth PD (New Focus 1601 AC) mentioned previously. The board contains a silicon PIN diode PD (OSRAM SFH2400) followed by a TIA circuit based on an operational amplifier chip (TEXAS INSTRUMENTS: LMH6629). The reiver circuit is shown in Fig. 8. This receiver circuit could be developed with the cost of under 5 US Dollars ($5). The smaller bandwidth of this circuit reduces the overall useful modulation bandwidth of the system to about 300 MHz. The measured data rates and corresponding BER are presented in Table II. In total 8.24 Gb/s (7.67 Gb/s after 7% HDFEC coding overhead reduction) is achieved. This also confirms the high capacity of VLC systems for future wireless communications.

TABLE II:
THE SUMMARY OF EXPERIMENT RESULTS WITH SELF-MADE RX BOARD.

	BER	R [Gb/s]
Red	0.0021	2.183
Green	0.0032	2.262
Blue	0.0021	2.180
Yellow	0.0033	1.618

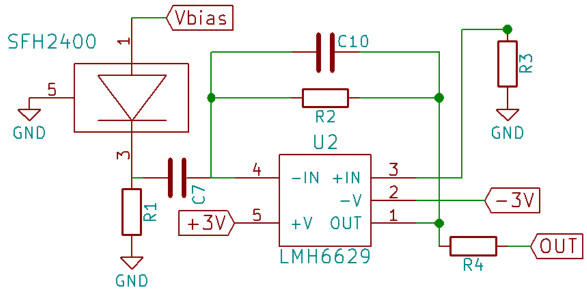

Fig. 8: The circuit design of the receiver board.

IV. Conclusion

In this paper, the highest achieved data rate in the LED-based VLC systems is reported. Low-cost commercially available LEDs are chosen to signify the great potential of VLC systems for high data rate communication. A WDM system with four visible light wavelengths is designed based on dichroic mirrors. Each wavelength is modulated using DCO-OFDM with adaptive bit-loading and system parameters are optimized experimentally. A data transmission rate of 15.73 Gb/s is achieved with the BER below the 7% HDFEC limit of 3.8×10^{-3} over a 1.6 m wireless link.

Acknowledgment

Professor Haas gratefully acknowledge the support of this research by the Engineering and Physical Sciences Research Council (EPSRC) under an Established Career Fellowship grant, EP/R007101/1. He also acknowledges the financial support of his research by the Wolfson Foundation and the Royal Society.

References

[1] T. Cogalan and H. Haas, “Why would 5G need optical wireless communications?” in *IEEE Int. Symp. Pers., Indoor Mobile Radio Commun. (PIMRC)*, Oct. 2017, pp. 1–6.

[2] H. Elgala, R. Mesleh, and H. Haas, “Indoor optical wireless communication: potential and state-of-the-art,” *IEEE Communications Magazine*, vol. 49, no. 9, pp. 56–62, Sept. 2011.

[3] H. Haas, L. Yin, Y. Wang, and C. Chen, “What is LiFi?” *Journal of Lightwave Technology*, vol. 34, no. 6, pp. 1533–1544, Mar. 2016.

[4] I. Tavakkolnia, C. Chen, R. Bian, and H. Haas, “Energy-efficient adaptive MIMO-VLC technique for indoor LiFi applications,” in *Int. Conf. Telecommun. (ICT)*, Jun. 2018, pp. 1–6.

[5] M. D. Soltani, X. Wu, M. Safari, and H. Haas, “Bidirectional user throughput maximization based on feedback reduction in LiFi networks,” *IEEE Trans. Commun.*, vol. 66, no. 7, pp. 3172–3186, Jul. 2018.

[6] A. Khalid, G. Cossu, R. Corsini, P. Choudhury, and E. Ciaramella, “1-gb/s transmission over a phosphorescent white led by using rate-adaptive discrete multitone modulation,” *IEEE Photonics Journal*, vol. 4, no. 5, pp. 1465–1473, Oct. 2012.

[7] S. Rajbhandari, J. J. McKendry, J. Herrnsdorf, H. Chun, G. Faulkner, H. Haas, I. M. Watson, D. OBrien, and M. D. Dawson, “A review of gallium nitride LEDs for multi-gigabit-per-second visible light data communications,” *Semiconductor Science and Technology*, vol. 32, no. 2, p. 023001, 2017.

[8] D. Tsonev, S. Videv, and H. Haas, “Towards a 100 Gb/s visible light wireless access network,” *Optics express*, vol. 23, no. 2, pp. 1627–1637, Jan. 2015.

[9] S. Viola, M. S. Islim, S. Watson, S. Videv, H. Haas, and A. E. Kelly, “15 Gb/s OFDM-based VLC using direct modulation of 450 GaN laser diode,” in *Advanced Free-Space Optical Communication Techniques and Applications III*, vol. 10437. International Society for Optics and Photonics, Oct. 2017, p. 104370E.

[10] Y.-C. Chi, Y.-F. Huang, T.-C. Wu, C.-T. Tsai, L.-Y. Chen, H.-C. Kuo, and G.-R. Lin, “Violet laser diode enables lighting communication,” *Scientific Reports*, vol. 7, no. 1, p. 10469, Sep. 2017.

[11] T.-C. Wu, Y.-C. Chi, H.-Y. Wang, C.-T. Tsai, and G.-R. Lin, “Blue laser diode enables underwater communication at 12.4 Gbps,” *Scientific reports*, vol. 7, p. 40480, Jan. 2017.

[12] C.-Y. Li, H.-H. Lu, W.-S. Tsai, Z.-H. Wang, C.-W. Hung, C.-W. Su, and Y.-F. Lu, “A 5 m/25 Gbps underwater wireless optical communication system,” *IEEE Photonics Journal*, Jun. 2018.

[13] T.-C. Wu, Y.-C. Chi, H.-Y. Wang, C.-T. Tsai, Y.-F. Huang, and G.-R. Lin, “Tricolor R/G/B laser diode based eye-safe white lighting communication beyond 8 Gbit/s,” *Scientific reports*, vol. 7, no. 1, p. 11, Jan. 2017.

[14] D. Tsonev, H. Chun, S. Rajbhandari, J. J. McKendry, S. Videv, E. Gu, M. Haji, S. Watson, A. E. Kelly, G. Faulkner *et al.*, “A 3-Gb/s single-LED OFDM-based wireless VLC link using a gallium nitride μLED,” *IEEE Photon. Technol. Lett.*, vol. 26, no. 7, pp. 637–640, Apr. 2014.

[15] M. S. Islim, R. X. Ferreira, X. He, E. Xie, S. Videv, S. Viola, S. Watson, N. Bamiedakis, R. V. Penty, I. H. White *et al.*, “Towards 10 Gb/s orthogonal frequency division multiplexing-based visible light communication using a GaN violet micro-LED,” *Photonics Research*, vol. 5, no. 2, pp. A35–A43, Apr 2017.

[16] H. Chun, S. Rajbhandari, G. Faulkner, D. Tsonev, E. Xie, J. J. D. McKendry, E. Gu, M. D. Dawson, D. C. O’Brien, and H. Haas, “LED based wavelength division multiplexed 10 Gb/s visible light communications,” *Journal of lightwave technology*, vol. 34, no. 13, pp. 3047–3052, Jul. 2016.

[17] Y. Wang, L. Tao, X. Huang, J. Shi, and N. Chi, “8-Gb/s RGBY LED-based WDM VLC system employing high-order CAP modulation and hybrid post equalizer,” *IEEE Photonics Journal*, vol. 7, no. 6, pp. 1–7, Dec. 2015.

[18] X. Zhu, F. Wang, M. Shi, N. Chi, J. Liu, and F. Jiang, “10.72 Gb/s Visible Light Communication System Based On Single Packaged RGBYC LED Utilizing QAM-DMT Modulation With Hardware Pre-Equalization,” in *Optical Fiber Communication Conference*. Optical Society of America, Mar. 2018, pp. M3K–3.

[19] R. Bian, I. Tavakkolnia, and H. Haas, “10.2 Gb/s visible light communication with off-the-shelf LEDs,” in *Eur. Conf. Opt. Commun. (ECOC)*, Sep. 2018, pp. 1–3.

[20] H. E. Levin, “A complete and optimal data allocation method for practical discrete multitone systems,” in *Global Telecommunications Conference, 2001. GLOBECOM’01. IEEE*, vol. 1. IEEE, Dec. 2001, pp. 369–374.

[21] M. Z. Afgani, H. Haas, H. Elgala, and D. Knipp, “Visible light communication using OFDM,” in *Testbeds and Research Infrastructures for the Development of Networks and Communities, 2006. TRIDENTCOM 2006. 2nd International Conference on*, mar. 2006, pp. 6–pp.

[22] J. Armstrong and A. Lowery, “Power efficient optical OFDM,” *Electronics letters*, vol. 42, no. 6, pp. 370–372, Mar. 2006.

[23] L. Chen, B. Krongold, and J. Evans, “Theoretical characterization of nonlinear clipping effects in im/dd optical ofdm systems,” *IEEE Transactions on Communications*, vol. 60, no. 8, pp. 2304–2312, Aug. 2012.

[24] S. Dimitrov and H. Haas, “Information rate of ofdm-based optical wireless communication systems with nonlinear distortion,” *Journal of Lightwave Technology*, vol. 31, no. 6, pp. 918–929, Mar. 2013.

[25] D. Tsonev, S. Videv, and H. Haas, “Unlocking spectral efficiency in intensity modulation and direct detection systems,” *IEEE Journal on Selected Areas in Communications*, vol. 33, no. 9, pp. 1758–1770, Sep. 2015.

[26] A. Alvarado, E. Agrell, D. Lavery, R. Maher, and P. Bayvel, “Replacing the soft-decision fec limit paradigm in the design of optical communication systems,” *Journal of Lightwave Technology*, vol. 33, no. 20, pp. 4338–4352, Oct. 2015.

[27] Vishay, “Ultrabright 0402 ChipLED,” 91000 datasheet, Feb. 2017.

References

[1] CISCO. (Nov 2018) Cisco visual networking index: Forecast and trends, 2017-2022. [Online]. Available: https://www.cisco.com/c/en/us/solutions/collateral/service-provider/visual-networking-index-vni/white-paper-c11-741490.html#_Toc529314175

[2] H. Haas. (April 2013) High speed wireless networking using visible light. [Online]. Available: http://spie.org/newsroom/4773-high--speed-wireless-networking-using-visible-light

[3] S. Dimitrov and H. Haas, *Principles of LED Light Communications: Towards Networked Li-Fi*. Cambridge University Press, 2015.

[4] U. D. of Energy. (2016) Energy savings forecast of solid-state lighting in general illumination applications. [Online]. Available: https://www.energy.gov/sites/prod/files/2016/09/f33/energysavingsforecast16_2.pdf

[5] R. Mesleh, H. Haas, C. W. Ahn, and S. Yun, "Spatial Modulation – A New Low Complexity Spectral Efficiency Enhancing Technique," in *IEEE International Conference on Communication and Networking in China (CHINACOM)*, Beijing, China, Oct. 25–27, 2006, pp. 1–5.

[6] R. Mesleh, H. Elgala, and H. Haas, "Optical Spatial Modulation," *IEEE/OSA J. Opt. Commun. Netw.*, vol. 3, no. 3, pp. 234–244, Mar. 2011, ISSN: 1943-0620.

[7] T. Komine and M. Nakagawa, "Fundamental Analysis for Visible–Light Communication System using LED Lights," *IEEE Trans. Consum. Electron.*, vol. 50, no. 1, pp. 100–107, Feb. 2004.

[8] A. M. Khalid, G. Cossu, R. Corsini, P. Choudhury, and E. Ciaramella, "1-Gb/s transmission over a phosphorescent white LED by using rate-adaptive discrete multitone modulation," *IEEE Photon. J.*, vol. 4, no. 5, pp. 1465–1473, Oct. 2012.

[9] E. Schubert, *Light-Emitting Diodes*, 1st ed. Cambridge University Press, 2003, ISBN 0 521 82330 7.

[10] D. Tsonev, H. Chun, S. Rajbhandari, J. McKendry, S. Videv, E. Gu, M. Haji, S. Watson, A. Kelly, G. Faulkner, M. Dawson, H. Haas, and D. O'Brien, "A 3-Gb/s Single-LED OFDM-Based Wireless VLC Link Using a Gallium Nitride μLED," *IEEE Photon. Technol. Lett.*, vol. 26, no. 7, pp. 637–640, Apr. 2014.

[11] M. S. Islim, R. X. Ferreira, X. He, E. Xie, S. Videv, S. Viola, S. Watson, N. Bamiedakis, R. V. Penty, I. H. White, A. E. Kelly, E. Gu, H. Haas, and M. D. Dawson, "Towards 10 gb/s orthogonal frequency division multiplexing-based visible light communication using a gan violet micro-led," *Photonics Research*, vol. 5, pp. 35–43, 2017.

[12] CISCO. (2014) The internet of things. [Online]. Available: https://www.cisco.com/c/dam/en_us/solutions/trends/iot/docs/iot-aag.pdf

[13] H. Haas. (Nov 2015) Forget wi-fi. meet the new li-fi internet. [Online]. Available: https://www.ted.com/talks/harald_haas_a_breakthrough_new_kind_of_wireless_internet

[14] S. Zhang, D. Tsonev, S. Videv, S. Ghosh, G. A. Turnbull, I. D. W. Samuel, and H. Haas, "Organic solar cells as high-speed data detectors for visible light communication," *Optica*, July 2015.

[15] R. Bian, S. Videv, A. D. Griffiths, J. J. D. McKendry, E. Xie, E. Gu, M. D. Dawson, and H. Haas, "Experimental demonstration of generalised space shift keying for visible light communication," in *2017 IEEE BlackSeaCom*, Jun 2017.

[16] S. Rajbhandari, A. V. N. Jalajakumari, H. Chun, G. Faulkner, K. Cameron, R. Henderson, D. Tsonev, H. Haas, E. Xie, J. J. D. McKendry, J. Herrnsdorf, R. Ferreira, E. Gu, M. D. Dawson, and D. O'Brien, "A multigigabit per second integrated multiple-input multiple-output vlc demonstrator," *Journal of Lightwave Technology*, vol. 35, 2017.

[17] R. Bian, S. Videv, A. D. Griffiths, J. J. D. Mckendry, E. Xie, K. Cameron, E. Gu, S. Rajbhandari, G. Faulkner, D. O'Brien, M. D. Dawson, R. Henderson, and H. Haas, "A high speed generalised space shift keying link with micro-leds and cmos apd receiver," in *2016 IEEE SUM*, July 2016.

[18] R. Bian, I. Tavakkolnia, and H. Haas, "10.2 gb/s visible light communication with off-the-shelf leds," in *2018 ECOC*, 2018.

[19] ——, "15.73 gb/s visible light communication with off-the-shelf leds," *Journal of Lightwave Technology*, vol. 37, p. 2, 2019.

[20] A. G. Bell, "Selenium and the Photophone," *Nature*, vol. 22, no. 569, pp. 500–503, 1880.

[21] M. I. Nathan, W. P. Dumke, G. Burns, and F. H. Dill, "Stimulated Emission of Radiation from GaAs p-n Junctions," *Appl. Phys. Lett.*, vol. 1, no. 3, p. 62, 1962.

[22] Z. Ghassemlooy, W. Popoola, and S. Rajbhandari, *Optical Wireless Communications: System and Channel Modeling with MATLAB(R)*, 1st ed. CRC Press, 2012.

[23] T. H. Maiman, "Stimulated optical radiation in ruby," *Nature*, pp. 493–494, 1960.

[24] F. E. Goodwin, "A review of operational laser communication systems," *Proceedings of the IEEE*, vol. 58, no. 10, pp. 1746–1752, Oct. 1970.

[25] F. R. Gfeller and U. Bapst, "Wireless In-House Data Communication Via Diffuse Infrared Radiation," *Proc. IEEE*, vol. 67, no. 11, pp. 1474–1486, Nov. 1979.

[26] P. Barker and A. C. Boucouvalas, "Performance modeling of the IrDA protocol for infrared wireless communications," vol. 36, no. 12, pp. 113–117, 1998.

[27] W. Creek. Infrared data association (irda). [Online]. Available: http://www.irda.org/

[28] IEEE. (2014) The IEEE P802.15.7r1 Short-Range Optical Wireless Communication Task Group Project Authorization Request (PAR). . [Online]. Available: http://www.ieee802.org/15/pub/IEEE%20802_15%20WPAN%2015_7%20Revision1%20Task%20GroupOLD.htm

[29] ——. (2018) Status of IEEE 802.11 Light Communication TG. [Online]. Available: http://www.ieee802.org/11/Reports/tgbb_update.htm

[30] A. A. Bergh and P. J. Dean, "Light-emitting diodes," *Proceedings of the IEEE*, vol. 60, no. 2, pp. 156–223, 1972.

[31] H. Elgala, R. Mesleh, and H. Haas, "Non-linearity Effects and Predistortion in Optical OFDM Wireless Transmission Using LEDs," *Inderscience International Journal of Ultra Wideband Communications and Systems (IJUWBCS)*, vol. 1, no. 2, pp. 143–150, 2009.

[32] S. Forrest, P. Burrows, and M. Thompson, "The dawn of organic electronics," *IEEE Spectrum*, Aug 2000.

[33] S. Zvanovec, P. Chvojka, P. Haigh, and Z. Ghassemlooy, "Visible light communication towards 5g," *Radioengineering*, vol. 24, no. 1, pp. 1–9, 2015.

[34] H. Chen, Z. Xu, Q. Gao, and S. Li, "A 51.6 mb/s experimental vlc system using a monochromic organic led," *IEEE Photonics Journal*, vol. 10, April 2018.

[35] J. M. Senior, *Optical Fiber Communications Principles and Practice*, 3rd ed. Essex: Pearson Education Limited, 2009.

[36] Z. Wang, D. Tsonev, S. Videv, and H. Haas, "Towards Self-Powered Solar Panel Receiver for Optical Wireless Communication," in *Proc. IEEE Int. Conf. Commun. (ICC)*, Sydney, NSW, Jun. 10–14 2014, pp. 3348–3353.

[37] ——, "On the Design of a Solar-Panel Receiver for Optical Wireless Communications with Simultaneous Energy Harvesting," *IEEE J. Sel. Areas Commun.*, vol. 33, no. 8, pp. 1612–1623, 2015.

[38] G. Keiser, *Optical Fiber Communications*, 3rd ed. New York: McGraw-Hill, 2000.

[39] J. M. Kahn and J. R. Barry, "Wireless Infrared Communications," *Proc. IEEE*, vol. 85, no. 2, pp. 265–298, Feb. 1997.

[40] B. Wilson and Z. Ghassemlooy, "Pulse Time Modulation Techniques for Optical Communications: A Review," in *Proceeding of the IEE on Optoelectronics*, vol. 140, no. 6, Dec. 1993, pp. 347–357.

[41] S. Dimitrov and H. Haas, "Optimum signal shaping in ofdm-based optical waireless communication systems," in *2012 IEEE VTC Fall*, Sep 2012.

[42] S. Rajbhandari, Z. Ghassemlooy, and M. Angelova, "Optimising the Performance of Digital Pulse Interval Modulation With Guard Slots for Diffuse Indoor Optical Wireless Links ," *IET Microwaves, Antennas and Propagation*, vol. 5, no. 9, pp. 1025–1030, Jun. 2011.

[43] J. B. Carruthers and J. M. Kahn, “Multiple-subcarrier Modulation for Nondirected Wireless Infrared Communication,” *IEEE Journal on Selected Areas in Communications*, vol. 14, no. 3, pp. 538–546, Apr. 1996.

[44] J. Armstrong, “OFDM for Optical Communications,” *J. Lightw. Technol.*, vol. 27, no. 3, pp. 189–204, Feb. 2009.

[45] J. Armstrong and A. Lowery, “Power Efficient Optical OFDM,” *Electronics Letters*, vol. 42, no. 6, pp. 370–372, Mar. 16, 2006.

[46] H. Elgala, R. Melsleh, H. Haas, and B. Pricope, “OFDM Visible Light Wireless Communication based on White LEDs,” in *2007 IEEE 65th VTC Spring*, April 2007.

[47] S. Dimitrov, S. Sinanovic, and H. Haas, “Signal Shaping and Modulation for Optical Wireless Communication,” *Lightwave Technology, Journal of*, vol. 30, no. 9, pp. 1319–1328, May 2012.

[48] H. E. Levin, “A Complete and Optimal Data Allocation Method for Practical Discrete Multitone Systems,” in *Proc. IEEE Global Telecommun. Conf.*, vol. 1, San Antonio, TX , USA, 25–29 Nov. 2001, pp. 369–374.

[49] D. Tsonev, S. Videv, and H. Haas, “Unlocking Spectral Efficiency in Intensity Modulation and Direct Detection Systems,” *IEEE J. Sel. Areas Commun.*, vol. PP, no. 99, pp. 1–1, 2015.

[50] ——, “Towards a 100 Gb/s Visible Light Wireless Access Network,” *Opt. Express*, vol. 23, no. 2, pp. 1627–1637, Jan 2015. [Online]. Available: http://www.opticsexpress.org/abstract.cfm?URI=oe-23-2-1627

[51] G. V. Tsoulos, “Experimental and theoretical capacity analysis of space-division multiple access (SDMA) with adaptive antennas,” *IEE Proceedings- Communications*, vol. 146, no. 5, pp. 307–311, Oct. 1999.

[52] G. J. Foschini and M. J. Gans, “On Limits of Wireless Communications in a Fading Environment when Using Multiple Antennas,” *Wireless Personal Communications*, vol. 6, no. 6, pp. 311–335, 1998.

[53] Y. Wang, L. Tao, X. Huang, J. Shi, and N. Chi, “8-gb/s rgby led-based wdm vlc system employing high-order cap modulation and hybrid post equalizer,” *IEEE Photonics Journal*, vol. 7, Dec. 2015.

[54] D. Tsonev, S. Videv, and H. Haas, “Towards a 100 Gb/s visible light wireless access network,” *Optics express*, vol. 23, no. 2, pp. 1627–1637, Jan. 2015.

[55] R. Mesleh, H. Haas, S. Sinanović, C. W. Ahn, and S. Yun, “Spatial Modulation,” *IEEE Trans. on Veh. Tech.*, vol. 57, no. 4, pp. 2228 – 2241, Jul. 2008.

[56] M. Di Renzo, H. Haas, and P. M. Grant, “Spatial modulation for multiple-antenna wireless systems: a survey,” *Communications Magazine, IEEE*, vol. 49, no. 12, pp. 182 – 191, 2011.

[57] T. Fath and H. Haas, "Performance Comparison of MIMO Techniques for Optical Wireless Communications in Indoor Environments," *Communications, IEEE Transactions on*, vol. 61, no. 2, pp. 733 – 742, 2013.

[58] A. Burton, H. L. Minh, Z. Ghassemlooy, E. Bentley, and C. Botella, "Experimental Demonstration of 50-Mb/s Visible Light Communications Using 4 x 4 MIMO," *IEEE Photonics Technology Letter*, vol. 26, no. 9, May 2014.

[59] L. Zeng, D. O'Brien, H. Minh, G. Faulkner, K. Lee, D. Jung, Y. Oh, and E. T. Won, "High Data Rate Multiple Input Multiple Output (MIMO) Optical Wireless Communications Using White LED Lighting," *IEEE J. Sel. Areas Commun.*, vol. 27, no. 9, pp. 1654–1662, Dec. 2009.

[60] A. Azhar, T. Tran, and D. O'Brien, "A Gigabit/s Idoor Wireless Transmission using MIMO-OFDM Visible-Light Communications," *IEEE Photon. Technol. Lett.*, vol. 25, no. 2, pp. 171–174, Jan.15 2013.

[61] J. J. D. McKendry, D. Massoubre, S. Zhang, B. R. Rae, R. P. Green, E. Gu, R. K. Henderson, A. E. Kelly and M. D. Dawson, "Visible-light communications using a CMOS-controlled micro-light-emitting-diode array," *J. Lightw. Technol.*, vol. 30, no. 1, pp. 61–67, 2012.

[62] J. Jeganathan, A. Ghrayeb, L. Szczecinski, and A. Ceron, "Space Shift Keying Modulation for MIMO Channels," *IEEE Trans. on Wireless Commun.*, vol. 8, no. 7, pp. 3692–3703, Jul. 2009.

[63] J. Jeganathan, A. Ghrayeb, and L. Szczecinski, "Generalized Space Shift Keying Modulation for MIMO Channels," in *Proc. IEEE 19th Intern. Symp. on Personal, Indoor and Mobile Radio Commun. PIMRC 2008*, Cannes, France, 15–18 Sep. 2008, pp. 1–5.

[64] D. Tsonev, S. Sinanovic, and H. Haas, "Complete Modeling of Nonlinear Distortion in OFDM-based Optical Wireless Communication," *J. Lightw. Technol.*, vol. 31, no. 18, pp. 3064–3076, Sep. 15 2013.

[65] S. Rajagopal, R. D. Roberts, and S.-K. Lim, "Ieee 802.15.7 visible light communication: Modulation schemes and dimming support," *IEEE Communications Magazine*, vol. 50, no. 3, pp. 72–82, Mar. 2012.

[66] T. Fath, M. Di Renzo, and H. Haas, "On the performance of space shift keying for optical wireless communications," in *IEEE GLOBECOM Workshops (Globecom 2010) - Workshop on Optical Wireless Communications*, Miami, FL, USA, 6-10 Dec. 2010, pp. 990 – 994.

[67] W. Popoola, E. Poves, and Haas, "Error Performance of Generalised Space Shift Keying for Indoor Visible Light Communications," *IEEE Transactions on Communications*, pp. 1–9, 2013.

[68] Y. Sun, D. Borah, and E. Curry, "Optimal symbol set selection in gssk visible light wireless communication systems," *IEEE Photonics Technology Letters*, vol. 28, no. 3, pp. 303–306, 2016.

[69] K. Ebihara, K. Kamakura, and T. Yamazato, “Spatially-modulated space-time coding in visible light communications using 2Œ2 led,” in *Circuits and Systems (APCCAS), 2014 IEEE Asia Pacific Conference on*, Nov. 2014, pp. 320–323.

[70] W. Popoola and H. Haas, “Demonstration of the merit and limitation of generalised space shift keying for indoor visible light communications,” vol. 32, pp. 1960–1965.

[71] W. Popoola, E. Poves, and H. Haas, “Generalised space shift keying for visible light communications,” in *8th International Symposium on Communication Systems, Networks & Digital Signal Processing (CSNDSP 2012)*, Poznan, Poland, 18-20 July 2012, pp. 1 – 4.

[72] S. Rajagopal, R. D. Roberts, and S.-K. Lim, “Ieee 802.15.7 visible light communication: Modulation schemes and dimming support,” vol. 50, no. 3, pp. 72–82.

[73] H. Haas, L. Yin, Y. Wang, and C. Chen, “What is lifi?” *Journal of Lightwave Technology*, vol. 34, no. 6, pp. 1533–1544, Mar 2016.

[74] I. Tavakkolnia, C. Chen, R. Bian, and H. Haas, “Energy-efficient adaptive mimo-vlc technique for indoor lifi applications,” in *Int. Conf. Telecommun. (ICT)*, Jun. 2018.

[75] M. D. Soltani, X. Wu, M. Safari, and H. Haas, “Bidirectional user throughput maximization based on feedback reduction in lifi networks,” *IEEE Trans. Commun.*, vol. 66, no. 7, pp. 3172–3186, Jul. 2018.

[76] S. Rajbhandari, J. J. McKendry, J. Herrnsdorf, H. Chun, G. Faulkner, H. Haas, I. M. Watson, D. O’Brien, and M. D. Dawson, “A review of gallium nitride LEDs for multi-gigabit-per-second visible light data communications,” *Semiconductor Science and Technology*, vol. 32, no. 2, p. 023001, 2017.

[77] S. Viola, M. S. Islim, S. Watson, S. Videv, H. Haas, and A. E. Kelly, “15 Gb/s OFDM-based VLC using direct modulation of 450 GaN laser diode,” in *Advanced Free-Space Optical Communication Techniques and Applications III*, vol. 10437. International Society for Optics and Photonics, Oct. 2017, p. 104370E.

[78] Y. C. Chi, Y. F. Huang, T. C. Wu, C. T. Tsai, L. Y. Chen, H. C. Kuo, and G. R. Lin, “Violet laser diode enables lighting communication,” *Scientific Reports*, vol. 7, no. 1, p. 10469, Sep. 2017.

[79] T. C. Wu, Y. C. Chi, H. Y. Wang, C. T. Tsai, and G. R. Lin, “Blue laser diode enables underwater communication at 12.4 Gbps,” *Scientific reports*, vol. 7, p. 40480, Jan. 2017.

[80] C. Y. Li, H. H. Lu, W. S. Tsai, Z. H. Wang, C. W. Hung, C. W. Su, and Y. F. Lu, “A 5 m/25 Gbps underwater wireless optical communication system,” *IEEE Photonics Journal*, Jun. 2018.

[81] T. C. Wu, Y. C. Chi, H. Y. Wang, C. T. Tsai, Y. F. Huang, and G. R. Lin, “Tricolor R/G/B laser diode based eye-safe white lighting communication beyond 8 Gbit/s,” *Scientific reports*, vol. 7, no. 1, p. 11, Jan. 2017.

[82] D. Tsonev, H. Chun, S. Rajbhandari, J. J. McKendry, S. Videv, E. Gu, M. Haji, S. Watson, A. E. Kelly, G. Faulkner *et al.*, “A 3-Gb/s single-LED OFDM-based wireless VLC link using a gallium nitride μLED,” *IEEE Photon. Technol. Lett.*, vol. 26, no. 7, pp. 637–640, Apr. 2014.

[83] M. S. Islim, R. X. Ferreira, X. He, E. Xie, S. Videv, S. Viola, S. Watson, N. Bamiedakis, R. V. Penty, I. H. White *et al.*, "Towards 10 Gb/s orthogonal frequency division multiplexing-based visible light communication using a GaN violet micro-LED," *Photonics Research*, vol. 5, no. 2, pp. A35–A43, Apr 2017.

[84] H. Chun, S. Rajbhandari, G. Faulkner, D. Tsonev, E. Xie, J. J. D. McKendry, E. Gu, M. D. Dawson, D. C. O'Brien, and H. Haas, "LED based wavelength division multiplexed 10 Gb/s visible light communications," *Journal of lightwave technology*, vol. 34, no. 13, pp. 3047–3052, Jul. 2016.

[85] X. Zhu, F. Wang, M. Shi, N. Chi, J. Liu, and F. Jiang, "10.72 Gb/s Visible Light Communication System Based On Single Packaged RGBYC LED Utilizing QAM-DMT Modulation With Hardware Pre-Equalization," in *Optical Fiber Communication Conference*. Optical Society of America, Mar. 2018, pp. M3K–3.

[86] H. E. Levin, "A complete and optimal data allocation method for practical discrete multitone systems," in *Global Telecommunications Conference, 2001. GLOBECOM'01. IEEE*, vol. 1. IEEE, Dec. 2001, pp. 369–374.

[87] M. Afgani, H. Haas, H. Elgala, and D. Knipp, "Visible light communication using ofdm," in *2nd International Conference on Testbeds and Research Infrastructures for the Development of Networks and Communities. TRIDENTCOM*, 2006, pp. 6 pp.–134.

[88] J. Armstrong and A. Lowery, "Power efficient optical OFDM," *Electronics letters*, vol. 42, no. 6, pp. 370–372, Mar. 2006.

[89] L. Chen, B. Krongold, and J. Evans, "Theoretical characterization of nonlinear clipping effects in im/dd optical ofdm systems," *IEEE Transactions on Communications*, vol. 60, no. 8, pp. 2304–2312, Aug. 2012.

[90] S. Dimitrov and H. Haas, "Information rate of ofdm-based optical wireless communication systems with nonlinear distortion," *Journal of Lightwave Technology*, vol. 31, no. 6, pp. 918–929, Mar. 2013.

[91] D. Tsonev, S. Videv, and H. Haas, "Unlocking spectral efficiency in intensity modulation and direct detection systems," *IEEE Journal on Selected Areas in Communications*, vol. 33, no. 9, pp. 1758–1770, Sep. 2015.

[92] A. Alvarado, E. Agrell, D. Lavery, R. Maher, and P. Bayvel, "Replacing the soft-decision fec limit paradigm in the design of optical communication systems," *Journal of Lightwave Technology*, vol. 33, no. 20, pp. 4338–4352, Oct. 2015.

[93] Vishay, "Ultrabright 0402 ChipLED," 91000 datasheet, Feb. 2017.

[94] Thorlabs. Longpass dichroic mirrors/beamsplitters. [Online]. Available: https://www.thorlabs.com/newgrouppage9.cfm?objectgroup_id=3313

[95] P. J. Reddy, *Science and Technology of Photovoltaics*, 2nd ed. The Netherlands: CRC Press, 2009.

[96] M. M. Rhaman and M. A. Matin, "Organic solar cells: Historical developments and challenges," in *2015 ICAEE*, Dec 2015.

[97] R. H. Bube, *Photoconductivity of Solids*. Wiley, New York, 1960.

[98] G. A. Chamberlain, "Organic solar cells: a review," *Solar Cells*, pp. 47–83, February 1983.

[99] H. Spanggaard and F. C. Krebs, "A brief history of the development of organic and polymeric photovoltaics," *Solar Energy Materials and Solar Cells*, vol. 83, pp. 125–146, 15 June 2004.

[100] I. Mathews, P. J. King, F. Stafford, and R. Frizzell, "Performance of iii-v solar cells as indoor light energy harvesters," *IEEE Journal of Photovoltaics*, 2015.

[101] W. Shin, S. Yang, D. Kwon, and S. Han, "Self-reverse-biased solar panel optical receiver for simultaneous visible light communication and energy harvesting," *Optics Express*, vol. 24, no. 22, Oct 2016.

[102] E. Bialic, L. Maret, and D. Ktenas, "Specific innovative semi-transparent solar cell for indoor and outdoor lifi applications," *Applied Optics*, vol. 54, no. 27, Sep 2015.

[103] R. Bian, L. K. Jagadamma, P. P. Manousiadis, I. Tavakkolnia, S. Videv, G. A. Turnbull, I. D. W. Samuel, and H. Haas, "Multiple-input multiple-output visible light communication with simultaneously energy harvesting using organic photovoltaics," 2019, to be submitted.

[104] Kennerud, "Analysis of performance degradation in cds solar cells," *IEEE Transactions on Aerospace and Electronic Systems*, vol. 5, pp. 912–917, Nov. 1969.

[105] M. Villalva, J. Gazoli, and E. Filho, "Comprehensive Approach to Modeling and Simulation of Photovoltaic Arrays," *IEEE Trans. Power Electron.* , vol. 24, no. 5, pp. 1198–1208, May 2009.

[106] D. Sera, R. Teodorescu, and P. Rodriguez, "PV Panel Model Based on Datasheet Values," in *Proc. IEEE Int. Symp. Ind. Electron. (ISIE)*, Vigo, Spain, Jun. 4–7 2007, pp. 2392–2396.

[107] M. A. Stosovic, D. Lukac, I. Litovski, and V. Litovski, "Frequency domain characterization of a solar cell," in *11th Symposium on Neural Network Applications in Electrical Engineering*, Sep 2012.

[108] P. Rueda, E. F. Lisbona, and M. D. Herrero, "Capacitance measurements on multi-junction solar cells," in *3rd WCPEC Proceedings of*, May 2003.